TECHNISCHE
UNIVERSITÄT
WIEN
Vienna University of Technology

# Modelling and thermo-kinetic computer analysis of the precipitation sequence of metastable and stable phases in heat treatable aluminium alloys

## Peter Lang

Doctoral thesis

Vienna University of Technology,

Faculty for Mechanical and Industrial Engineering

Institute of Materials Science and Technology

August 2014

Dissertation

# Modelling and thermo-kinetic computer analysis of the precipitation sequence of metastable and stable phases in heat treatable aluminium alloys

ausgeführt zum Zwecke der Erlangung des akademischen Grades eines

Doktor der technischen Wissenschaften unter der Leitung von

Prof. Ernst Kozeschnik
E308
Institut für Werkstoffwissenschaft und Werkstofftechnologie

eingereicht an der Technischen Universität Wien

Fakultät für Maschinenwesen und Betriebswissenschaften

von

Peter Lang
9835133
Obere Gartengasse 27a, 7041 Wulkaprodersdorf

Cambridge, am 03.09.2014

## Abstract

Computational Materials Science has grown rapidly over the last decades with remarkable close collaborations and long term partnerships between industry and academic researchers. In this work some examples of modelling subjects are presented to show the profitable commercial benefit resulting from the application of this type of research. The aspect of modelling is to connect theoretical and experimental work, having a sound theoretical base, which allows making predictions about distinguished material's behaviour, for example prediction about precipitating evolution or mechanical properties. The major goal of the present work is the numerical description of the precipitation kinetics of Al-Mg-Si(-Cu) and Al-Zn-Mg(-Cu) alloys. Multiscale thermo-kinetic modelling is used for different aspects of processes, predicting the amounts of different phases as well as mechanical properties. Quantum mechanics modelling techniques are applied, describing materials properties such as enthalpy of formation of metastable and stable phases. Calculated ab intio binding energies enables to describe the interactions of elements and clusters to vacancies and the related influences to the mobility of the system are taken into account in the models.

## Zusammenfassung

In den letzten Jahrzehnten haben sich computerunterstützte Materialwissenschaften durch Zusammenarbeit von Industrie und akademischen Forschern erfolgreich entwickelt und bewährt. In dieser Arbeit werden einige Beispiele der Modellierung und ihrer möglichen Anwendung vorgestellt, um den kommerziellen Nutzen durch die Verwendung von computergestützter Simulation und Modellierung zu zeigen. Die Grundlage der Modellierung liegt darin begründet theoretische und experimentelle Erkenntnisse zu einer soliden theoretischen Basis zu vereinen, um reale Vorhersagen über das Verhalten unterschiedlichster Materialien machen zu können. Beispielsweise seien die Ausscheidungsreaktionen in metallischen Legierungen und Vorhersagen über mechanischen Eigenschaften genannt. Das Hauptziel der vorliegenden Arbeit ist die numerische Beschreibung der Phasentrennung und Ausscheidungskinetik der Al-Mg-Si(-Cu) und Al-Zn-Mg(-Cu)-Legierungen. Thermo-kinetische Modellierung kann für verschiedenste Prozessschritte und Verfahren verwendet werden, um detaillierte Vorhersagen über Teilchenmenge und Größenverteilungen der verschiedenen Phasen, sowie deren Einfluss auf die resultierenden mechanischen Eigenschaften, zu machen. In der vorliegenden Arbeit werden des weiteren quantenmechanische Modellierungstechniken zur Bestimmung spezifischer Materialeigenschaften, wie etwa der Bildungsenthalpie von metastabilen und stabilen Phasen, angewendet und beschrieben. Berechnete Bindungsenergien zwischen Leerstellen mit gelösten Elementen und Clustern sind in den Modellen implementiert und werden bei der Beschreibung der Mobilität des Systems berücksichtigt.

The research in this thesis was performed at the

Institute of Materials Science and -Technology,

University of Technology, Vienna, Austria,

within the research activities of the K2 Competence Centre on “Integrated Research in Materials, Processing and Product Engineering”, operated by the Materials Center Leoben Forschung GmbH in the framework of the Austrian Comet Competence Centre Programme.

to Marion and Sophia, my beloved daughters

and Margit, my beloved and esteemed wife

with love

# Acknowledgement

I would like to thank my advisor Professor Ernst Kozeschnik for allowing me the opportunity to work on this project and for his help, encouragement and advice throughout his project.

I especially thank Margit for her infinite love and time, understanding and support.

I thank my family, especially "Papa, Tante Gerti" and "Oma" and my friends and colleagues, I met during my thesis, to allow me to be where I am today  and for all their help to get me work-on and finish this thesis.

I also would like to express my appreciation for the efforts of AMAG Austria Metall AG, Austria, for supplying the aluminium alloys used in this project.

Financial support by the Austrian Federal Government (in particular from the Bundesministerium für Verkehr, Innovation und Technologie and the Bundesministerium für Wirtschaft, Familie und Jugend) and the Styrian Provincial Government, represented by Österreichische Forschungsförderungs-gesellschaft mbH and by Steirische Wirtschaftsförderungsgesellschaft mbH, within the research activities of the K2 Competence Centre on ‘‘Integrated Research in Materials, Processing and Product Engineering’’, operated by the Materials Center Leoben Forschung GmbH in the framework of the Austrian COMET Competence Centre Programme, is gratefully acknowledged.

Cambridge, 2014

Peter Lang

# Preface

This thesis is submitted in partial fulfilment of the requirements for the degree of technical doctor at the Vienna University of Technology. The doctoral work has been carried out at the Faculty of Mechanical and Industrial Engineering, Institute of Materials Science and -Technology, Vienna, Austria.

The thesis is divided into two parts. The first part contains an introduction to the main modelling approaches and techniques used. Part two contains five selected scientific papers that constitute the most important portion of this thesis. The experimental details and simulation results of this work are omitted from Part one and instead described in the papers in Part two.

- P. Lang, P. Mohn, A. Falahati, E. Kozeschnik, "*Ab initio simulations of vacancy-solute clusters in Al-Mg-Si and Al-Zn-Mg alloys*", Proc. 13th International Conference on Aluminum Alloys ICAA13 (2012) 273-277.
- P. Lang, Y.V. Shan, E. Kozeschnik, "*The life-time of structural vacancies in the presence of solute trapping*", Materials Science Forum 794-796 (2014) 963-970.
- P. Lang, E. Povoden-Karadeniz, A. Falahati, E. Kozeschnik, "*Simulation of the effect of composition on the precipitation in 6xxx Al alloys during continuous-heating DSC*", Journal of Alloys and Compounds (2014) 443-449.
- P. Lang, T. Wojcik, E. Povoden-Karadeniz, A. Falahati, E. Kozeschnik, "*Thermo-kinetic prediction of metastable and stable phase precipitation in Al-Zn-Mg series aluminium alloys during non-isothermal DSC analysis*", Journal of Alloys and Compounds 609 (2014) 129-136.
- P. Lang, T. Weisz, M.R. Ahmadi, E. Povoden-Karadeniz, A. Falahati, E. Kozeschnik, "*Thermo-kinetic simulation of the yield strength evolution of AA7075 during natural aging*", Advanced Materials Research 922 (2014) 406-411.
- P. Lang, M. Rath, P. Sherstnev, E. Kozeschnik, "*Simulation of the plastic deformation response of AA 6082 in W condition*", Materials Science and Engineering (2014) under review.

# Full publication record

1. P. Lang, A.Falahati, E.Povoden-Karadeniz, O.Nodin, P.Warczok, M.R.Ahmadi,E.Kozeschnik, “*Simulation of precipitation sequences of metastable and stable phases in Al-Mg-Si alloys*“, Proceedings of JSC (2010) 111-112.
2. A. Falahati, E. Povoden-Karadeniz, P. Lang, P. Warczok, E. Kozeschnik, “*Thermo-kinetic computer simulation of different scanning calorimetry curves of AlMgSi alloys*“, International Journal of Materials Research 101 9 (2010) 1089-1096.
3. A. Falahati, P. Lang, M.R.Ahmadi, P. Warczok, E. Povoden-Karadeniz, E. Kozeschnik, “*Computer Simulation der Ausscheidungs-Mikrostruktur- und Festigkeitsentwicklung von Al-Mg-Si Legierungen in mehrstufigen Wärmebehandlungen*“, in: "MOBILITÄT IM WANDEL*:* Anforderungen an modernen Leichtbau und Leichtmetalle" (2010) ISBN: 978-3-902092-06-9, 61-75.
4. P.Lang, A.Falahati, E.Povoden-Karadeniz, M.R.Ahmadi, P.Warczok, E.Kozeschnik, “*Modeling of the Yield Strength Evolution in Al-Mg-Si Alloys”,* Proceedings of the 12th International Conference on Aluminium Alloys, The Japan Institute of Light Metals, 1 (2010), ISBN: 978-4-905829-11-9, 1443-1448.
5. P.Lang, A.Falahati, M.R.Ahmadi, P.Warczok, E.Povoden-Karadeniz, R.Radis, E.Kozeschnik, ”*Modeling the influence of cooling rate on the precipitate evolution in Al-Mg-Si (Cu) alloys*”, Proceedings of Materials Science and Technology MS&T (2011) 284-291.
6. A. Falahati, M.R. Ahmadi, P. Warczok, P. Lang, E. Povoden-Karadeniz, E. Kozeschnik, “*Thermo-kinetic computer simulation of precipitation and age-hardening effect in Al-Mg-Si alloys with arbitrary heat treatment*”, Proceedings of Materials Science and Technology MS&T (2011) 292-299.
7. P. Lang, P. Mohn, A. Falahati, E. Kozeschnik, “*Ab initio simulations of vacancy-solute clusters in Al-Mg-Si and Al-Zn-Mg alloys”,* Proceedings of the 13th International Conference on Aluminium Alloys (2012) ISBN: 978-1-118-45804-4, 273-277.
8. A. Falahati, P. Lang, E. Kozeschnik, “*Precipitation in Al-alloy 6016 – The role of excess vacancies*”, Materials Science Forum 706-709 (2012) 317-322.
9. P. Sherstnev, P. Lang. E. Kozeschnik, “*Treatment of simultaneous deformation and solid-state precipitation in thermo-kinetic calculations*“, Proceedings of European Congress on Computational Methods in Applied Sciences and Engineering, e-Book Full Papers ECCOMAS (2012) 5331-5338.

10. P. Lang, E. Povoden-Karadeniz, W. Mayer, A. Falahati, E. Kozeschnik, “*The bustling nature of vacancies in Al alloys*“, Proceedings of Pacific Rim International Congress on Advanced Materials and Processing PRICM8 (2013), ISBN: 978-0-470-94309-0, 3181-3188.
11. P. Lang, E. Kozeschnik, “*Modelling and simulation to improve quality and efficiency*”, AluReport 2 (2013) 8-9.
12. E. Povoden-Karadeniz, D.C. Cirstea, P. Lang, T. Wojcik, E. Kozeschnik, “*Thermodynamics of Ti-Ni shape memory alloys*“, Computer Coupling of Phase Diagrams and Thermochemistry Calphad 41 (2013) 128-139.
13. E. Povoden-Karadeniz, P. Lang, P. Warczok, A. Falahati, W. Jun, E. Kozeschnik, “*CALPHAD modeling of metastable phases in the Al-Mg-Si system*“, Calphad 43 (2013) 94-104.
14. E. Povoden-Karadeniz, P. Lang, K.I. Öksüz, W. Jun, S. Rafiezadeh, A. Falahati, E. Kozeschnik, “*Thermodynamics-integrated simulation of precipitate evolution in Al-Mg-Si-alloys*“, Materials Science Forum 765 (2013) 476-480.
15. P. Lang, T. Weisz, M.R. Ahmadi, E. Povoden-Karadeniz, A. Falahati, E. Kozeschnik, “*Thermo-kinetic simulation of the yield strength evolution of AA7075 during natural aging*”, Advanced Materials Research 922 (2014) 406-411.
16. P. Lang, M.C. Lang, A. Falahati, E. Kozeschnik, “*The effect of Si on the precipitation behaviour in Al-Mg-Si alloys studied by thermo-kinetic simulation and DSC experiments*“, Berg- und Hüttenmänische Monatshefte BHM 159 (2014) 116-212.
17. E. Povoden-Karadeniz, E. Eidenberger, P. Lang, G. Stechauner, H. Leitner, E. Kozeschnik, “*Simulation of precipitate evolution in Fe-25 Co-15 Mo with Si addition based on computational thermodynamics*”, Journal of Alloys and Compounds 587 (2014) 158-170.
18. P. Lang, Y.V. Shan, E. Kozeschnik, “*The life-time of structural vacancies in the presence of solute trapping*“, Materials Science Forum 794-796 (2014) 963-970.
19. P. Lang, T. Wojcik, E. Povoden-Karadeniz, A. Falahati, E. Kozeschnik, “*Thermo-kinetic prediction of metastable and stable phase precipitation in Al-Zn-Mg series aluminium alloys during non-isothermal DSC analysis*“, Journal of Alloys and Compounds 609 (2014) 129-136.
20. P. Lang, E. Povoden-Karadeniz, A. Falahati, E. Kozeschnik, “*Simulation of the effect of composition on the precipitation in 6xxx Al alloys during continuous-heating DSC*“, Journal of Alloys and Compounds 612 (2014) 443-449.
21. P. Lang, T. Wojcik, E. Povoden-Karadeniz, E. Kozeschnik, “*Crystal structure and free energy of Ti2Ni3 precipitates in Ti-Ni alloys from first principles*”, Computational Materials Science 93 (2014) 46-49.

# Part I

## Computational methodology & model approaches

Peter Lang

# Contents

# 1. Introduction

Aluminium alloys are widely used for structural components in the automotive and aerospace industry because they offer an advantageous combination of low density, strength and formability. Pure aluminium is too soft to be used in structural components. Alloying it with other elements increases the strength either due to precipitation hardening or by solid solution strengthening. Precipitation hardening occurs during natural or artificial ageing treatment after solutionising the material at temperatures close to the melting point. In the initially supersaturated solid solution, the alloying elements form precipitates. Additions of Mg, Si and Cu constitute the heat-treatable 6xxx series, adding Zn, Mg and Cu constitute the heat-treatable 7xxx aluminium alloys. This series of aluminium alloys are normally aged at 120-200 °C during which the system undergoes complex precipitation reactions, consisting of a series of metastable and stable precipitates with different stoichiometry and various morphologies. The precipitation reactions can be described by three main microstructural processes: nucleation, growth and coarsening. In most cases, these reactions take place simultaneously. Physical modelling helps for better understanding of processing-structure-property relationships. The objective of developing models for the precipitation reactions is making a link between processing parameters, such as aging time and temperatures, chemical composition and precipitate characteristics, such as sizes and number densities.

## 1.1 Al-Mg-Si(-Cu) alloys - 6xxx series

Al-Mg-Si(-Cu) alloys are used in a wide range of applications, including automobile body sheet, extrusions profiles and aircraft sheets. This type of alloy is used as a medium-strength structural alloy with good corrosion resistance. Industrial 6xxx Al series alloys are either balanced in Mg and Si content to form the quasi-binary Al-$Mg_2Si$ or have excess Si (or Mg). The 6xxx Al series are typically aged at temperatures around 160 - 190 °C. The ternary 6xxx Al series (Al-Mg-Si) is mainly strengthened by precipitation of the metastable precursor precipitates β” of the equilibrium β ($Mg_2Si$) phase. In Al-Mg-Si-Cu alloys, dependent on the Cu content, other phases such as Q’, L, S, C or QC may also precipitate and replace β” partially as the most efficient strengthening phase [1].

The precipitation sequence in hardenable 6xxx Al-alloys is generally accepted as [2-10]:

SSS → clusters/co-clusters of Mg and Si → GP zones → ß” (L, C) →ß’(Q’, B’, U1, U2) →ß (Q, Si)

In the presented modelling framework, a multi-component, multi-precipitate distribution in the Al matrix, taking the solute elements and, partly, simultaneous formation of cluster and co-cluster, GP-zones, Cu containing ß", ß', B', U1, U2, ß, Q and free Si into account, is considered. Details about precipitates are given in the related publications, applied modelling techniques are discussed in chapter 2 and 3.

DSC (Differential Scanning Calorimetry) analysis is used to investigate the precipitation reactions during continuous heating to study the precipitation sequence. Based on experimental DSC thermograms, we optimize the input parameters for modelling along the whole precipitation path. TEM (Transmission Electron Microscopy) investigations, yield strength measurements and data from literature are used to validate our outputs of the precipitation model.

## 1.2 Al-Zn-Mg(-Cu) alloys - 7xxx series

The 7xxx series of aluminium alloys are primarily used in the aerospace industry and as high-strength structural components. The 7xxx series alloys are precipitation-hardening metallic materials with the main alloying elements Zn and Mg, as well as additions of Cu.

The precipitation sequence in hardenable 7xxx Al-alloys is generally accepted as [11-13]:

SSS → metastable GP zones →metastable η' (S') → stable η (S, τ)

GP-zones are generally considered as precipitates formed during room temperature ageing and the early stages of artificial ageing [14]. In combination with the evolution of quenched-in excess vacancies, these precipitates strongly influence the subsequent precipitation of the metastable phase η´, which is considered as the main hardening phase in 7xxx Al-alloys. The over-aged situation is represented by the nucleation and growth of the stable phase η ($MgZn_2$).

Prior to the evaluation of the sequence of precipitates in the Al 6xxx and Al 7xxx series, and the assignment of the experimental findings to the individual phases, the thermodynamic description of the system is needed. First principle calculations are used to evaluate eventually missing enthalpies of formation of the stable and metastable phases. These formation enthalpies are used as starting values, using the CALPHAD (Computer Coupling of Phase Diagrams and Thermochemistry) approach, to give a complex description of the Gibbs energies of the phases [15]. The CALPHAD thermodynamic modelling is widely recognized as a powerful tool in predicting multi-component phase diagrams and guiding new materials development. A detailed description of the CALPHAD approach and methodology is given in ref. [16].

The mobility of the elements (tracer diffusion coefficient), based on experimental as well as on ab initio data, are compiled in mobility databases [17].

## 2. Model approaches in thermo-kinetic simulations

In the last few decades, modelling of nucleation and growth of secondary phases has evolved into several distinct approaches, originating from physical laws. One of these approaches is modelling the nucleation and growth, using a size distribution function of precipitates, which progresses using growth and nucleation laws, as implemented in the software tool MatCalc [18,19]. These models, which are able to describe the simultaneous nucleation, growth and coarsening, are outlined shortly in the following sections. A model associated calculation example, based on Al alloys, is given to illustrate the concepts for each approach.

## 2.1 Classical nucleation theory for multi-component systems

The classical nucleation theory (CNT) [20] is an important and elegant model approach to describe the initial step of phase transition based on thermodynamics and kinetics. Hardly worth mentioning, without basic thermodynamics and statistical physics modelling a nucleation event or predicting the size and composition of a nucleating critical cluster would not be possible. Using the CNT [20] theory, based on issues concerning multi-component nucleation, the following section provides a detailed picture of the nucleation theorem.

The nucleation kinetics of precipitates are calculated from the Classical Nucleation Theory (CNT) [20] extended for multi-component systems [18]. Accordingly, the transient nucleation rate *J* is given as:

$$J = N_0 Z \beta^* \cdot \exp\left(\frac{-G^*}{kT}\right) \cdot \exp\left(\frac{-\tau}{t}\right) . \tag{1}$$

*J* describes the rate at which nuclei are created per unit volume and time. $N_0$ represents the total number of potential nucleation sites. The Zeldovich factor *Z* takes into account that the nucleus is destabilised by thermal excitation. The atomic attachment rate is given by *ß**, taking into account the long-range diffusive transport of atoms. *G** is the critical energy for nucleus formation, *τ* is the incubation time, *k* is the Boltzmann constant, *T* is temperature and *t* is time.

***Example***: Minimum nucleation barrier concept for the metastable fcc Al-Cu system

The metastable fcc Al – 4 wt.% Cu system is taken as an example to illustrate the minimum nucleation barrier concept for the nucleus composition of the metastable Al-Cu cluster and the metastable Al-Cu GPB zones (θ”). The precipitation sequence in supersaturated Al-Cu solid solutions is [21]:

SSS → Al-Cu cluster → GPB zones (θ”, $Al_3Cu$) → metastable θ’ ($Al_{2+x}Cu_{1-x}$)→ stable θ ($Al_2Cu$).

This sequence commences with the formation of Al-rich Cu clusters, consisting of coherent layers on $\{0\ 0\ 1\}_{\alpha\text{-Al}}$ planes. GPB zones consist of two Cu layers separated by three Al planes, with the stoichiometry $Al_3Cu$ [21].

Figure 1 shows the driving force for coherent Al-Cu clusters, dependent on the chemical composition of the precipitate at 25 °C. The interfacial energy, shown in Fig. 1 (bottom plot) is composition-dependent and a quadratic function of the composition difference between precipitate and matrix. This statement is investigated in Figure 1, showing the driving force and the interfacial energy as function of the Cu content, $X_{Cu}$, of the Al-Cu cluster nucleus.

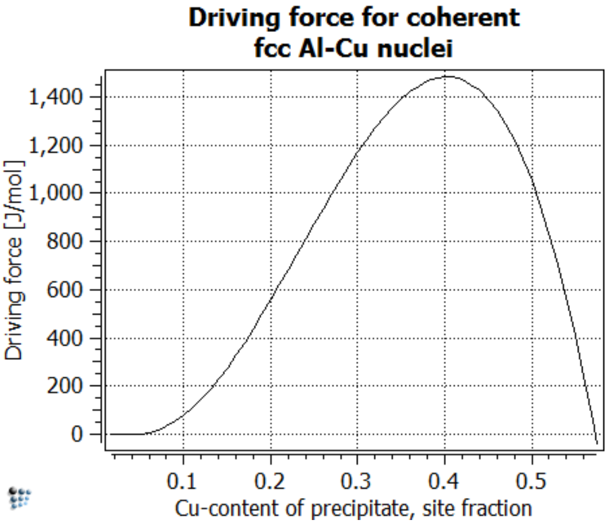

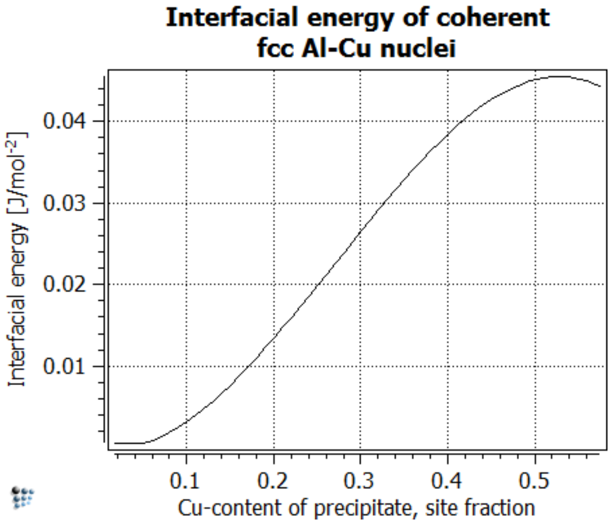

Figure 1: Chemical driving force and interfacial energy for fcc Al-Cu cluster at 25 °C.

Accordingly, it is found, that the chemical driving force adopts positive values for all compositions with $0.08 \leq X_{\mathrm{Cu}} \leq 0.57$. All of these compositions are thermodynamically metastable with respect to the equilibrium phase θ, $Al_2Cu$, which has been suspended from the system for the calculation. Above the composition of 0.57 Cu content, the driving force remains negative and no precipitates will form. The interfacial energy, calculated by the Generalized Broken-Bond (GBB) model [22], increases steadily for all values $X_{\mathrm{Cu}} \geq 0.01$ up to $X_{\mathrm{Cu}} \leq 0.54$.

It is interesting, now, that the two plots in Figure 1 suggest different composition regions for the ideal nucleus composition for which minimum $G^*$ can be expected. According to the driving force plot, the ideal composition should be given at a Cu content of the nucleus of $X_{\mathrm{Cu}} = 0.4$, where the driving force reaches a maximum. In contrast, the interfacial energy plot suggests, that the minimum interfacial energy is achieved at very low Cu ($X_{\mathrm{Cu}} \leq 0.05$) or $X_{\mathrm{Cu}} \geq 0.54$, where the interfacial energy starts to decrease again.

The analysis of the most likely nucleus composition, based on Classical Nucleation Theory (CNT) [20] prediction of the critical nucleation Gibbs energy, is given as function of the interfacial energy, $\gamma_0$, and the driving force $\Delta G_0$

$$G^* = \frac{16\pi}{3} \cdot \frac{(\gamma_0)^3}{(\Delta G_0)^2}\,. \tag{2}$$

Figure 2 presents the critical nucleation energy, $G^*$, as a function of the Cu-content of the nucleus in the Al-4 wt.% Cu system at 25 °C. Apparently, this quantity exhibit a pronounced minimum at a nucleus composition of approximately $X_{\mathrm{Cu}}$ = 0.11, which is in good agreement with experiments indicating Cu concentrations ranging from ~ 10 to 40 at.%, with the majority of precipitates exhibiting concentrations less than 25 at.% Cu [21].

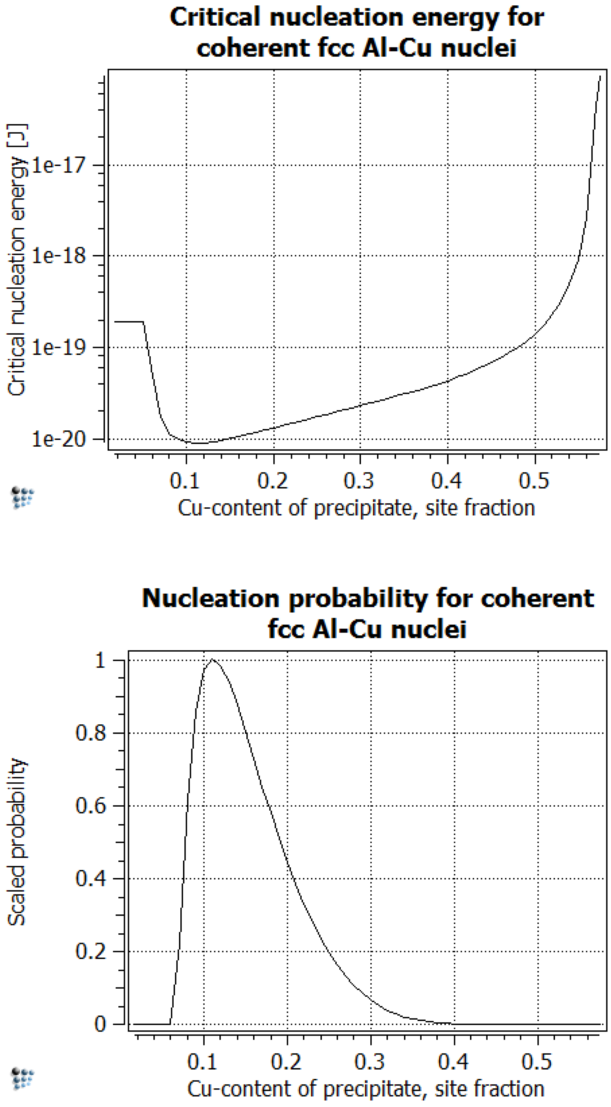

Figure 2: Critical nucleation energy and normalized nucleation probability for fcc Al-Cu cluster at 25 °C.

Nucleation reactions from the solute atoms form the first nuclei (cluster), e.g., several Al and Cu atoms combine to form clusters. As the composition of the cluster increases from $X_{Cu}$ = 0.06 to $X_{Cu}$ = 0.11, the critical nucleation energy, $G^*$, as a function of the Cu-content of the nucleus decreases, implying that the particle composition in this regime will follow the path to reach a Cu content of $X_{Cu}$ = 0.11. Exceeding $X_{Cu}$ = 0.11 in the Al-Cu nuclei, the critical nucleation energy increases again, indicating that the nuclei are not thermodynamically favourable, i.e., most of the Cu atoms exceeding the limit of $X_{Cu}$ = 0.11 dissolve back to the matrix to eventually form new nuclei.

The GPB zones are described in literature with the stoichiometry $Al_3Cu$ [21]. The stable phase is the θ ($Al_2Cu$) phase in the system Al – 4 wt.% Cu. Following figures depict the critical nucleation energy and the scaled nucleation probability of the GPB zones in the Al-Cu system (Figure 3) and the θ ($Al_2Cu$) phase (Figure 4).

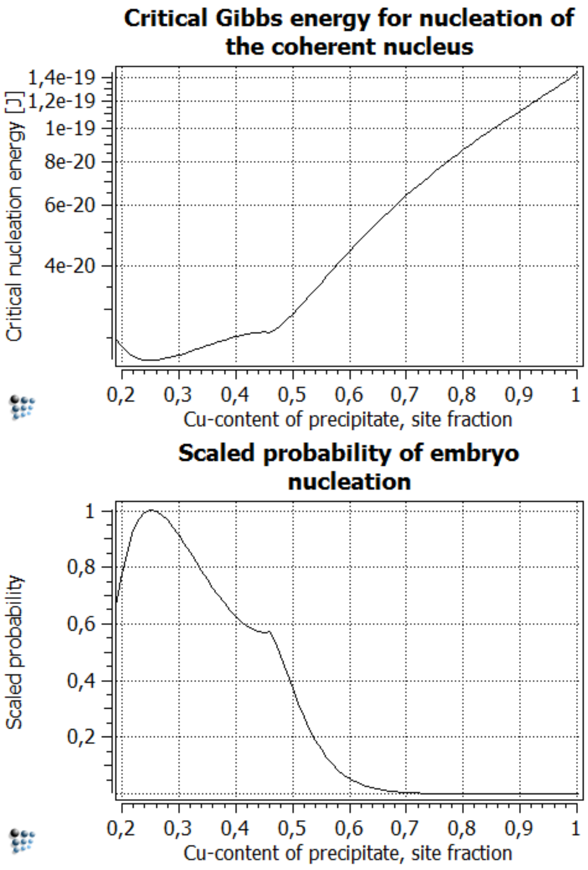

Figure 3: Critical nucleation energy and normalized nucleation probability for $Al_3Cu$ (GPB zone) at 250 °C.

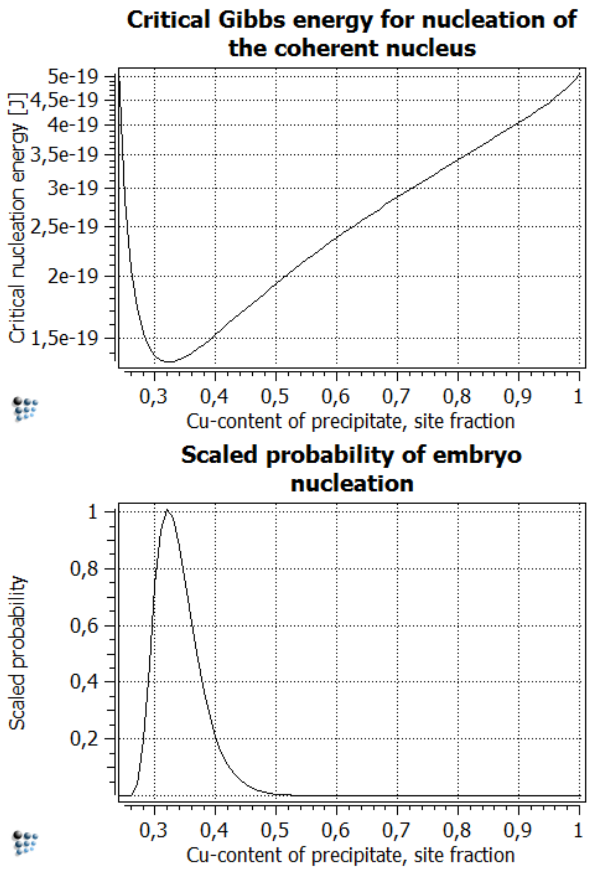

Figure 4: Critical nucleation energy and normalized nucleation probability for $Al_2Cu$ (θ phase) at 500 °C.

As clearly shown in figure 3, the critical nucleation energy for the GPB zones has a minimum at the Cu content of $X_{Cu}$ = 0.25, being completely in agreement with the experiment [21]. The formation of $Al_{1-x}Cu_x$ particles (with $x$ being ~0.33) is highly favoured at equilibrium conditions, leading to the formation of the stable $Al_2Cu$ (θ phase) as depicted in Figure 4.

## 2.2 Growth and coarsening – The SFFK model

In the previous section, theoretical models for nucleation of individual precipitates have been introduced and a numerical procedure for simulation of precipitate populations has been discussed.

In this section, a treatment of precipitate growth is presented, which is particularly suitable for application to higher-component systems due to effects of multi-component thermodynamics and diffusion. The theoretical treatment captures the essential physics in the case of multiple sublattice models and are therefore essential in the description of the evolution of the entire precipitation reactions in Al based alloys, as such systems have an arbitrary number of different particles, which precipitate inside the Al matrix. These precipitates are randomly distributed and each precipitate is in contact with the surrounding homogeneous matrix. It is important to recognize that the representation of the total free energy of the system involves only mean quantities for the composition of the matrix as well as the precipitates. In the following, the used approach is given shortly only for the benefit of clarity. Details on the model are published in refs. [18,19].

Once a precipitate is nucleated, further growth is evaluated based on the evolution equations for the radius and composition of the precipitate derived by Svoboda et al., [18] in a mean-field approach, also known as the SFFK model [18]. In a system containing *n* chemical elements and *m* randomly distributed precipitates with spherical diffusion fields, the total free energy of the system can be written as [18]:

$$G = \sum_{I=1}^{n} N_{0i}\mu_{oi} + \sum_{k=1}^{m} \frac{4\pi\rho_k^3}{3}\left(\lambda_k + \sum_{i=1}^{n} c_{ki}\mu_{ki}\right) + \sum_{k=1}^{m} 4\pi\rho_k^2\gamma_k, \tag{3}$$

where $\mu_{\mathrm{oi}}$ is the chemical potential of the component *i* in the matrix and $\mu_{\mathrm{ki}}$ is the chemical potential of the component *i* in the precipitate *k*. The chemical potentials are expressed as functions of the concentrations $c_{ki}$. $\gamma$ is the interface energy and $\lambda_k$ takes into account the contribution of the elastic energy due to the volume change of precipitates. $\rho_k$ is the radius of the discrete precipitate class. The numerical time integration is performed in the framework of the classical numerical Kampmann – Wagner approach [23].

If a thermodynamic system evolves to a more stable state, the difference in free energy between the initial and final stage is dissipated. This dissipation effect is accounted for in the SFFK model [18].

***Example***: Mean-field approach for the evolution of precipitates in Al alloys

The mean-field evolution equations of the model, denoted as the SFFK model [18], are utilized to calculate the precipitation evolution of an Al – 0.4 wt.% Mg - 1 wt.% Si during natural aging after solutionising and quenching. Homogeneous arrangement of randomly distributed solute atoms in a multicomponent matrix direct after the quench is considered. The evolution of a precipitate, once it has reached the supercritical size (e.g. the minimal size, where further growth leads to energy gain for the particle), can be described by the processes of attachment and detachment of monomers to the precipitate surface. The growth and dissolution of a precipitate is a deterministic process, describable by kinetic laws, whereas the nucleation rate for a second phase can only be formulated in terms of statistical evidences and probabilities. The transport of solute atoms through the matrix is a necessary condition for precipitate growth and it is described by diffusion laws. Accordingly, the radius evolution of the precipitate scales with the square root of time and follows a parabolic growth law. The following Figure 5 sketches a typical heat treatment for heat treatable Al alloys in T4 conditions (solution heat treated and naturally aged to a substantially stable condition).

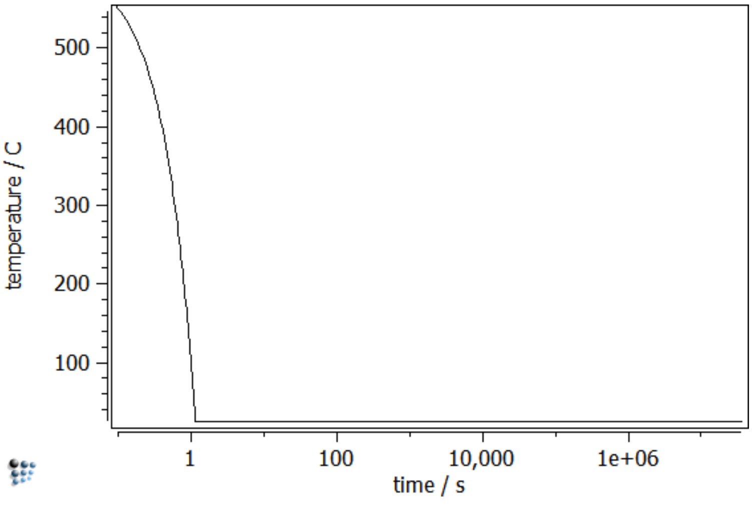

Figure 5: Heat treatment for Al-Mg-Si alloys in T4 condition;
solutionising at 560 °C, quenching and natural aging at 25 °C.

During the solution treatment, the alloy is held at a temperature that is above the solution temperature of the precipitates under consideration. The previously existing precipitates are dissolved and the elements constituting the precipitates are homogeneously distributed in the matrix. From the solution temperature, the alloy is quenched to room temperature, where diffusion of elements is so slow, that almost no precipitation can occur. Therefore, the quench must be performed fast enough that a substantial amount of excess quenched-in vacancies is introduced to the matrix in this step. The effect of excess vacancies is an acceleration on all diffusive processes during the subsequent tempering step. In the final step, the temperature is kept constant at room temperature (25 °C) and the material is naturally aged for $3.6 \cdot 10^7$ s (~ 14 month).

The evolution of the metastable Mg-Si co-cluster and/or GP zones for the given heat treatment is presented in Figure 6., showing the calculated mean radius and the number density evolution of the precipitates.

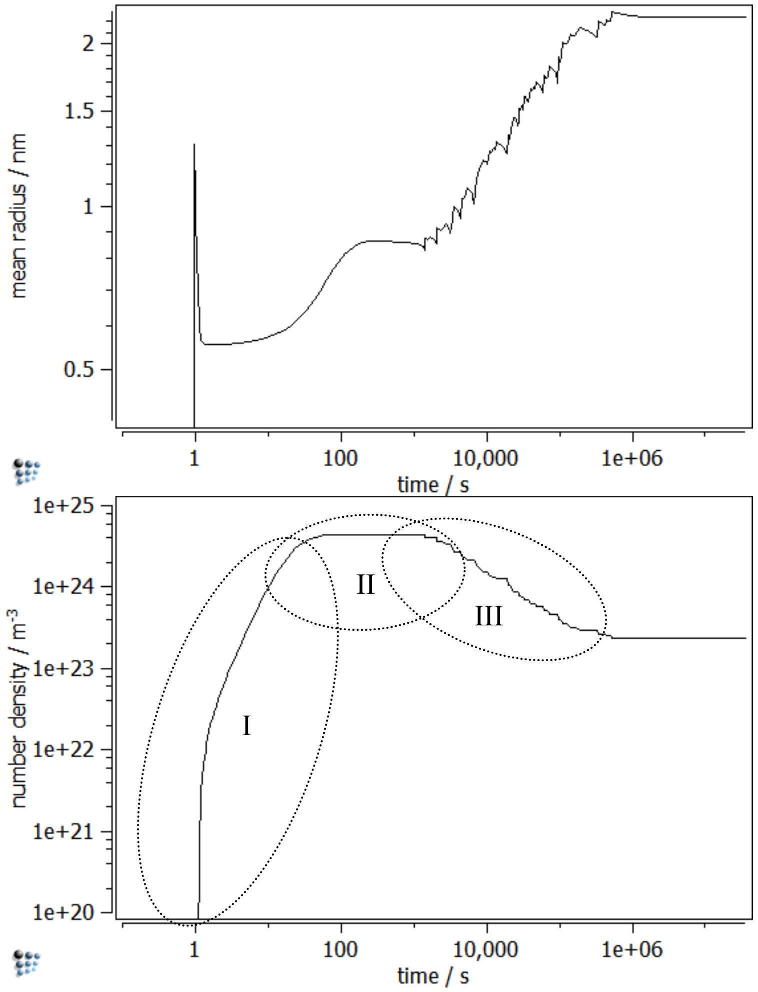

Figure 6: Evolution of radius and number density of metastable precipitates during natural aging after quench

Step I in the heat treatment contains the nucleation process, which is the initial step in precipitate life, characterized by a rapid increase of number density. Due to the positive driving force for precipitation, the nuclei are prone to stable continuous growth by continuous addition of other solute atoms. If the majority of nuclei have become overcritical, the process of growth controls the further life of the precipitates (step II). The supersaturation of the matrix decreases and nucleation is practically stopped. Once the particle growth stagnates and Ostwald ripening takes over, the Gibbs energy can be decreased by reducing the total precipitate-matrix interfacial area in the process of coarsening (step III). Smaller particles with a high surface area to volume ratio dissolve and larger precipitates continue to grow. Thereby, the total interfacial area decreases with a simultaneous decrease of the total free energy.

## 2.3 Numerical solutions of strengthening models

The remarkable strength increase in heat treatable alloys during natural aging can be attributed to a high number density of clusters (Ø ~ 1-3 nm) or GP-zones with 5-20 nm diameter. It is generally accepted that, for the coherent, shearable clusters or GP-zones, which nucleate after or even during the quench, the prominent strengthening mechanism is the coherency misfit stress effect. This effect is investigated in the following section together with the Orowan mechanism. The latter is operative for impenetrable precipitates with incoherent precipitate/matrix interfaces during aging. The topic of precipitation strengthening has recently been analysed by Ahmadi et al. [24] in general and in the case of aluminium alloys class 7xxx by Lang et al. [25]. The theory and approximations needed to build the evolution of strength are described in details. A relevant example regarding the contributions to the yield strength evolution in AA 6xxx is given as an example at the end of this section.

### 2.3.1 Coherency misfit strengthening

This mechanism is the most important strengthening mechanism in 6xxx and 7xxx Al alloys. According to Ardell [26], the increase in yield strength due to this mechanism can be written as

$$\Delta\sigma_{coh} = \alpha MG(\varepsilon)^{3/2}\left(\frac{8\pi r^{4} n_{v}}{3b}\right)^{1/2}, \tag{4}$$

where α is a constant (=3) [26] and ε is the fractional misfit between the precipitate and the matrix. *M* (=3.06) is the Taylor factor, $n_v$ is the number density of precipitates, *b* is the Burgers vector (=0.286 nm), *G* is the shear modulus (=28 GPa) and *r* is the mean radius of the precipitates.

### 2.3.2 Strengthening effect of non-shearable particles

Precipitation strengthening in Al-6xxx and Al-7xxx alloys (and also Al-2xxx alloys) is due to coherent and incoherent phases. The conventional relation for Orowan strengthening for incoherent phases is [26]:

$$\Delta\sigma_{Orowan} = \frac{0.4GbM}{\pi\lambda\sqrt{1-\upsilon}}\ln\left(\frac{2r}{b}\right), \tag{5}$$

where $\upsilon$ (=0.33) is Poisson’s ratio and $\lambda$ is the mean particle spacing in the slip plane of the dislocation.

To calculate the overall precipitation strengthening effect ($\sigma_p$), the different mechanisms for cutting and looping (Orowan mechanism) are superimposed as [26]:

$$\sigma_p = (\sigma_{coh}^{\alpha} + \sigma_{Orowan}^{\alpha})^{\frac{1}{\alpha}} \tag{6}$$

with $\alpha$ being 1.4.

### 2.3.3 Solid solution strengthening

In age hardening aluminium alloys, elements, such as Mg, Si, Zn and Cu, give rise to considerable solid solution strengthening. This effect is described by the following equation:

$$\sigma_{ss} = \sum_i k_i c_i^{2/3} \tag{7}$$

$c_i$ is the concentration (in weight percent) of element $i$ in solid solution and $k_i$ is the corresponding scaling factor, which is 29 MPa/wt.%$^{2/3}$ for Mg, 3 MPa/wt.%$^{2/3}$ for Zn, 66 MPa/wt.%$^{2/3}$ for Si and 46 MPa/wt.%$^{2/3}$ for Cu [27].

### 2.3.4 Calculation of the total yield strength evolution

The total yield strength, $R_{p0.2}$, is treated as a superposition of the inherent lattice strength ($\sigma_0$=20 MPa), solid solution strengthening ($\sigma_{ss}$) and precipitation strengthening ($\sigma_p$) as:

$$R_{p0.2} = \sigma_0 + \sigma_{ss} + \sigma_p \ . \tag{8}$$

***Example***: Modelling the strength evolution in an Al alloy 6061

With the theoretical model approaches for multi-component precipitation kinetics and hardening reactions, described in the previous section, the aging response of an Al alloy 6061 (Mg = 1 wt.%, Si = 0.7 wt.% and Cu = 0.3 wt.%) is studied. Figure 7 summarizes the applied heat treatment and the result of the simulation of the vacancy evolution in the Al alloy 6061.

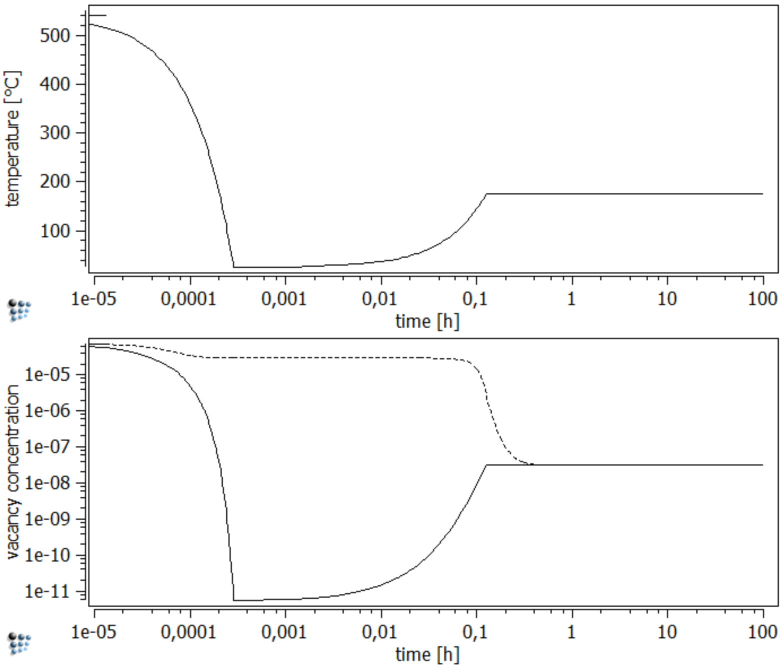

Figure 7: Temperature profile and vacancy evolution (equilibrium – solid line and excess *Va* – dashed line) during heat treatment of AA 6061.

When looking at the temperature profile of the heat treatment (top image of Figure 7), several individual steps can be distinguished. The simulation starts at 540 °C, which is just below the solidus temperature of this alloy. It is assumed that all elements are homogeneously distributed in the matrix at this time and no precipitates exist. The material is then linearly quenched to room temperature (25 °C, with a quenching rate of 500 °C/s). This temperature of 25 °C corresponds to the natural aging condition, where the sample is stored for 1 h. In the next step, the material is reheated for artificial aging and kept at 175 °C for 100 hours.

After quenching from 540 °C, various precipitate phases nucleate homogeneously in the bulk. At room temperature, the formation of clusters, co-clusters and GP-zones are assumed. After reheating to the artificial aging temperature of 175 °C, ß" precipitates, as the main hardening phase, are observed. The earlier phases, clusters, co-clusters and GP-zones, dissolve again during heating and holding at the artificial aging temperature of 175 °C.

Peak aged condition is observed after 8 hours at 175 °C. Subsequent coarsening of the ß" leads to a reduction in the yield strength and such an overaging regime is observed after aging the material for 40 and 100 hours at 175 °C.

During the natural short-term aging, the simulation predicts precipitation of clusters (and/or co-clusters) and GP-zones, which is in accordance with experimental observations. During heating and initial holding at 175 °C, the phase fraction of the ß" phase gradually increases and, simultaneously, the thermodynamically less stable early precipitates, clusters and GP-zones, start to dissolve. Again, this is consistent with literature. It should be noted that, due to the different possible nucleation sites of the early phases, the clusters, the GP-zones, as well as the ß" nucleation is assumed to be homogeneous. The number of substitutional atomic sites is used for the number density of potential nucleation sites, which is calculated by the number of substitutional sites within a matrix unit lattice cell divided by the volume of the matrix unit lattice cell.

Figure 8 summarises the evolution of the phase fraction, the number densities and the mean radii of the metastable phases, Mg-Si co-cluster, GP-zones and ß" phase. For better understanding, only these phases are named in the plots, the other lines represent the later phases ß', ß, Si and Q phase.

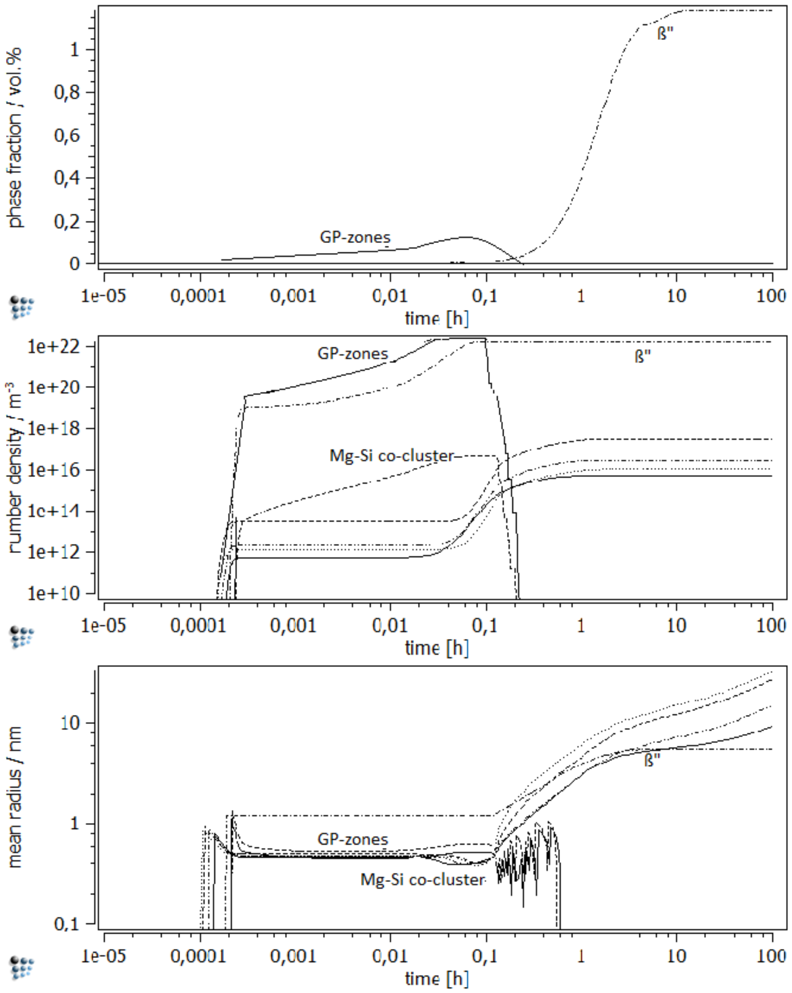

Figure 8: Kinetic simulation of precipitate evolution in AA 6061 during heat treatment, including solutionizing, quenching, room temperature storage and artificial aging.

In the following, the theory and methodology for the strength evolution, described previously, is applied to a prediction of the strength contribution during the heat treatment of the AA 6061. The simulation results shown in Figure 8 are used as a basis configuration of the microstructure evolution during the heat treatment. Figure 9 shows the predicted evolution of the strength contribution and the total yield strength compared to experimental findings.

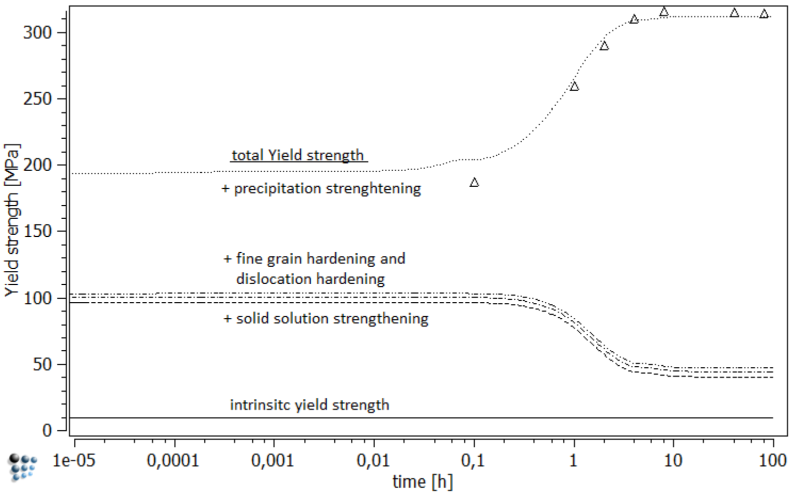

Figure 9: Predicted strength contributions to the total yield strength (lines) compared to experiment (triangles)

With the performance of this simple heat treatment, the strength of ~180 MPa in the "as quenched" conditions could be increased to more than 310 MPa for the AA6061. The results are clearly showing that precipitation strengthening is the key mechanism for improving mechanical properties of this kind of heat treatable Al alloy.

## 2.4 Dislocation density model

To obtain a better physical understanding of the flow stress and the dislocation density evolution, modelling and simulation of the work-hardening behaviour is applied in the framework of a simple but efficient one-parameter model based on the total dislocation density evolution. The term “one-parameter” emphasizes that the stress-strain response is controlled by the evolution of a single state parameter, only.  Lang et al. (unpublished work - P. Lang et al., Mater Sci Eng, under review) recently developed a simple parameterization for the evolution equations that is capable of describing the deformation characteristics of an AA6xxx aluminium alloy in terms of the temperature and strain-rate sensitive yield stress.

In the present model the total dislocation density, evolving as a consequence of the interplay of generation and annihilation terms during deformation in the material, is responsible for an increase in the yield strength.

The general relation between the Yield stress increase due to dislocation hardening, $\sigma_d$, and the total dislocation density, $\rho$, is given as [28,29]

$$\Delta\sigma_d = \alpha M G b\sqrt{\rho}\,, \tag{9}$$

with $M$ being the Taylor factor, $G$ the shear modulus and $b$ the Burger's vector. In the present analysis, $\alpha$ is a proportionality factor with the value of 0.5. This relation between stress and dislocation density holds for the cases where the flow stress is solely controlled by dislocation-dislocation interaction. Although this applies in a strict sense to pure fcc materials [30], only, it can also be used for dilute solid solutions, where the particle and lattice resistance to dislocation motion is negligibly small.

The *ABC* strain hardening one-parameter Ansatz consists of a hardening part, accounting for the strain-induced increase in dislocation density, and a softening contribution due to annihilation or rearrangement of dislocations (dynamic recovery).

### 2.4.1 Hardening

Based on the Kocks-Mecking formalism [31] and assuming that mobile dislocations move a mean free path $L$ before they are immobilized or annihilated, the increase in the dislocation density $\rho$ is given [32] by:

$$\frac{d\rho}{dt} = \frac{M\,\dot{\varphi}}{b\,L} \tag{10}$$

where *M* is the Taylor orientation factor (*M* = 3.06 for fcc crystals [26]), $\dot{\varphi}$ is the plastic strain rate and *b* is the Burger's vector.

The traveling distance is limited by the average spacing between dislocations:

$$L = \frac{A}{\sqrt{\rho}} \tag{11}$$

where *A* is a materials constant. Details to its dependence on strain rate and temperature are given in ref. [28] and in the part II of this thesis, referenced publications, manuscript "Simulation of the plastic deformation response of AA 6082 in W condition".

### 2.4.2 Softening

The reduction in dislocation density due to spontaneous annihilation, when two dislocations with antiparallel Burger's vectors come within a critical distance to each other, can be written as [33]:

$$\frac{d\rho}{dt} = -B\,2\frac{d_{\mathrm{ann}}}{b}\rho M\dot{\varphi} \tag{12}$$

where *B* is a parameter associated with the dependency of dynamic recovery on the strain rate and experimentally evaluated correlations are given in part II of this thesis, referenced publications, manuscript "Simulation of the plastic deformation response of AA 6082 in W condition".

The critical distance $d_{ann}$ is given as [34]:

$$d_{\mathrm{ann}} = \frac{G b^4}{2\pi(1-\nu)Q_v^f} \tag{13}$$

where *G* is the shear modulus of the aluminum matrix, *ν* is the Poisson's ratio (*ν* = 0.33 for aluminium) and $Q_v^f$ is the vacancy formation energy ($Q_v^f$ = 0.67 eV for aluminium).

The model describing recovery by dislocation climb is based on the assumption that thermally activated climb is controlled by substitutional self-diffusion along dislocations $D_d$ (pipe-diffusion) [35]:

$$\frac{d\rho}{dt} = -C\,2\,D_{\mathrm{d}}\,\frac{G\,b^3}{k_{\mathrm{B}}\,T}\left(\rho^2 - \rho_{\mathrm{eq}}^2\right) \tag{14}$$

where $k_B$ is the Bolzmann constant, *T* is the absolute temperature, $\rho_{\mathrm{eq}}$ is the equilibrium dislocation density ($\rho_{\mathrm{eq}} = 10^{11}$) and *C* is a calibration parameter, which can take into account effects, such as, solute trapping. In MatCalc, the dislocation core diffusivity is coupled to the bulk diffusivity via a temperature-dependent factor $\alpha_{\mathrm{d}}$ as [36]:

$$D_{\mathrm{d}} = \alpha_{\mathrm{d}}\,D_{\mathrm{b}}\,. \tag{15}$$

***Example***: Simulation of the deformation behaviour of an Al-Mg-Si alloy in W condition.

The deformation behaviour of an AA6082 aluminium alloy in W condition (solution treated) is investigated in a wide range of temperatures for a constant strain rate. In this study, a simple model is assessed for modelling the stress-strain curves for different testing conditions. There are mainly two aspects in the deformation behaviour of materials, namely: dislocation accumulation and dislocation annihilation.

Equation (8) for the contributions of pure aluminium yield strength, $\sigma_0$, and solid solution hardening, $\sigma_{ss}$, is added to the strain hardening, $\sigma_{\mathrm{d}}$, (eq.(9)) by the generalized form of addition law to calculate the total strength evolution $\sigma_{total}$. Precipitation strengthening, $\sigma_{ppt}$, can be neglected as the material is assumed to be in W condition (i.e. in the solution heat treated condition to avoid effects from natural ageing due to precipitation reactions).

Deformation tests in alloy AA6082, ref. [37], carried out in an Al-matrix with 0.59 wt.% Mg and 0.89 wt.% Si, are compared to the model results for a strain rate of 0.067 $s^{-1}$. Figure 10 summarizes the results of the deformation tests for the three testing temperatures of 25 °C, 200 °C and 300 °C. As deformation starts, the stress increases due to continuous dislocation nucleation and pile up (work-hardening). After the elastic/plastic transition the hardening rate decreases due to dynamic recovery (relaxation).

The model results, as shown in Figure 10, reproduce the stress-strain observations from experiment very well. At 25 °C, a maximum strength of 250 MPa is reached, whereas the strength at 300 °C reaches a plateau at about 150 MPa.

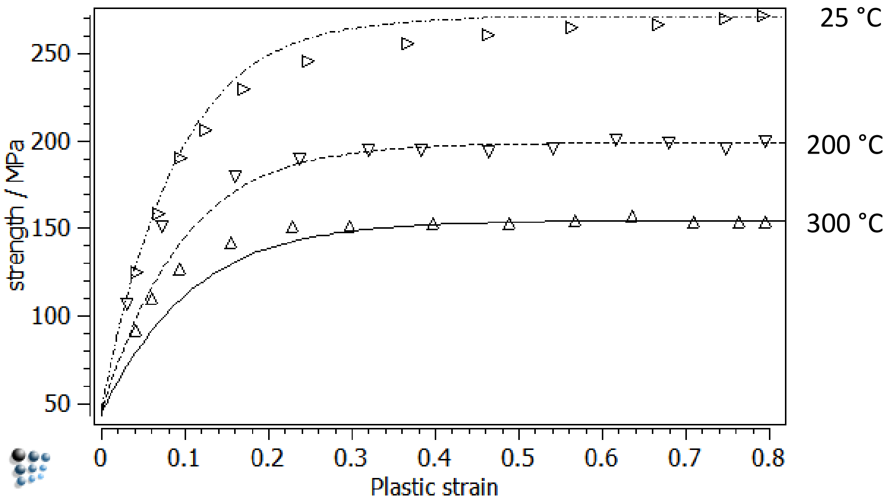

Figure 10: Comparison of experimental (symbols) and computed (curves) stress strain relations for a strain rate of 0.067 $s^{-1}$ at 20 °C, 200 °C and 300 °C for alloy AA6082

The calculated dislocation density evolutions are depicted in Figure 11. The initial equilibrium dislocation density was assumed to be $10^{11}$ $m^{-2}$ for all three conditions.

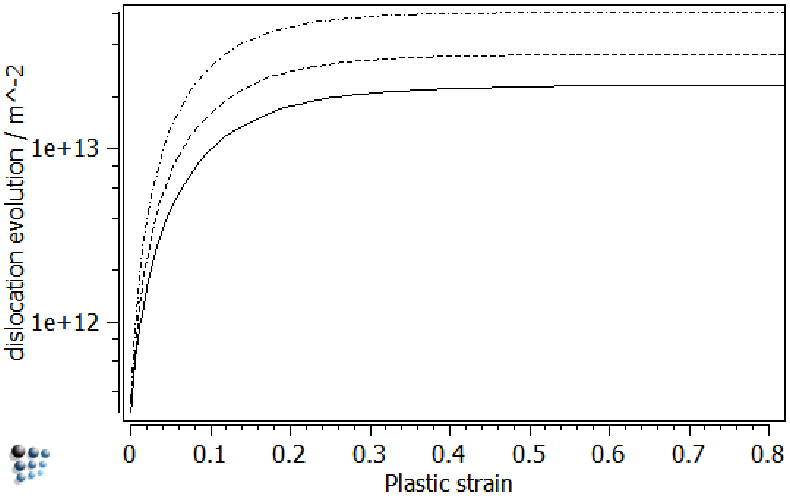

Figure 11: Computed dislocation density evolution for strain rates of 0.067 s$^{-1}$ at 25 °C, 200 °C and 300 °C for alloy Al - 0.59 wt.% Mg - 0.89 wt.% Si.

## 2.5 Vacancy evolution model

A model of the simultaneously generation and annihilation of vacancies in Al alloys is presented in ref. [38], which allows one to find the distribution function of excess vacancies in dependence of microstructure and heat treatment. These model is able to describe effects on the kinetics due to excess vacancies. Temperature and material parameters, such as energetic traps for vacancies, and the initial and evolved microstructure are taken into account. In the following sections these model approaches are discussed in detail.

Excess structural vacancies are produced during deformation by interacting moving jogs [39]. In the present work, the model by Stüwe [40] is used to describe the excess vacancy generation rate with:

$$\frac{dx_V^{ex}}{dt} = \chi_V \frac{M\,\dot{\varphi}\,L}{32\,N_V\,b^2}\rho \qquad (16)$$

where $N_V$ is the number of lattice sites per volume and $\chi_V$ is the vacancy generation coefficient ($\chi_V$ is in the order of $10^6$). We combine this equation with evolution equations for excess vacancy annihilation and generation at different types of sinks represented by jogs at dislocations, grain boundaries and free surfaces, as formulated in the following section.

### 2.5.1 Annihilation of excess vacancies

After solution annealing and quenching, the supersaturated solid solution (SSS) is highly supersaturated with vacancies. These excess vacancies are annihilated at appropriate sinks and sources such as dislocation jogs, incoherent interfaces, grain boundaries and free surfaces.

When a metal is heated and held at elevated temperature (solution annealing), the amount of structural vacancies increases rapidly to its equilibrium value. In the opposite direction, on cooling, time may not be sufficient, however, for the vacancies to reach the nearest vacancy sinks. Thus, annealing and rapid quenching may lead to states with a high amount of non-equilibrium quenched-in vacancies. The following models, derived by Fischer et al. [41], are implemented in the thermo-kinetic software tool MatCalc [18,19].

The two models corresponding to two different annihilation mechanisms are utilized and explained here briefly. The first is the annihilation and generation of excess vacancies at homogeneously distributed dislocation jogs (DJ) with constant density. The second is the annihilation of excess vacancies at grain boundaries (GB) with radius *R*. The vacancy generation / annihilation rates are denoted as $\dot{y}_0^{DJ}$ and $\dot{y}_0^{GB}$, and they are given by [41]:

$$\dot{y}_0^{DJ} = -\frac{2\pi a H y_0 \widetilde{D}_{eq}}{y_{0,eq} f}\left(\ln\frac{y_0}{y_{0,eq}} - \frac{\Omega}{R_g T}\sigma_H\right) \tag{17}$$

and

$$\dot{y}_0^{\,GB} = -\frac{15 y_0 \widetilde{D}_{eq}}{y_{0,eq} f R^2}\left(\ln\frac{y_0}{y_{0,eq}} - \frac{\Omega}{R_g T}\left(\sigma_H - \frac{\gamma_b}{R}\right)\right) \tag{18}$$

with:

| | |
|---|---|
| $a$ | interatomic spacing |
| $H$ | jog density of homogeneously distributed jogs |
| $y_{0,eq}$ | equilibrium site fraction of vacancies |
| $y_0$ | actual non equilibrium site fraction of vacancies |
| $\widetilde{D}_{eq}$ | effective diffusion coefficient of the matrix-forming element (here: Al) |
| $f$ | geometrical correlation factor, for fcc it is equal to 0.7815 |
| $\Omega$ | matrix molar volume corresponding to one mole of lattice sites |
| $\sigma_H$ | hydrostatic stress, which corresponds to the external pressure (if applicable) |
| $\frac{\gamma_b}{R}$ | surface stress contribution from the grain boundary energy |

### 2.5.2 Diffusional kinetics in the presence of non-equilibrium vacancies

Vacancies are the simplest type of lattice defect. However, they play a major role in the kinetics of diffusional processes, where mass transport is directly proportional to the concentration of vacancies. At a given temperature, each solid-state system contains a characteristic concentration of equilibrium structural vacancies, which influence significantly the thermodynamic and kinetic behaviour during manufacturing and processing. Diffusional mass transport by vacancies is the most important mechanism for precipitation, with the vacancies controlling the reaction rate inside the matrix. In most materials, the vacancy concentration at a given temperature follows an Arrhenius dependence. The mole fraction of equilibrium vacancies is in the order of $10^{-4}$ [42] close to the melting point and decreases upon cooling. The vacancies present in equilibrium condition are called thermal vacancies.

The equilibrium concentration of vacancies, $y_{0,eq}$, is predominantly temperature-dependent and is given by:

$$y_{0,eq} = \exp(-G_0 / R_g T) \tag{19}$$

with $G_0$ being the vacancy formation free energy and $R_g$ being the gas constant.

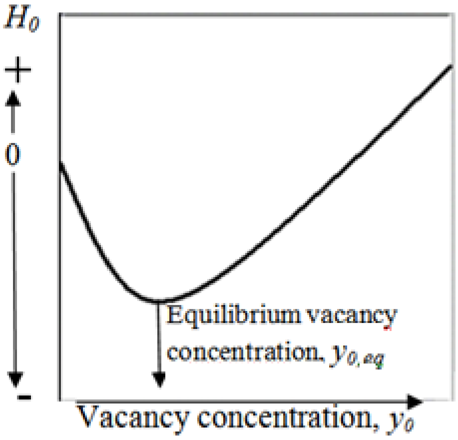

Figure 12: Enthalpy of a system dependent on the vacancy concentration.

The absolute vacancy concentration in a solid material is defined as a function of temperature, time and processing conditions. The amount depends strongly on the specific vacancy formation enthalpy, the applied cooling rates and on the strength of interaction between vacancies and solute atoms and/or solute complexes in solid solutions. Since the commonly applied heat treatment of heat-treatable alloys consists of solution annealing and subsequent quenching, this study focuses on the evolution of quenched-in excess vacancies under presence of vacancy traps, next.

### 2.5.3 Trapping of vacancies

When a specimen, after having been annealed at a relatively high temperature $T_1$, is quenched to some lower temperature $T_2$, imperfections, such as vacancies (in thermal equilibrium at high temperatures) can be frozen-in at low temperature. The diffusion path of vacancies can be manipulated by energetic traps, such as solute atoms or coherent precipitate / matrix interfaces or solute complexes. Strong binding between vacancies and solute atoms is an important factor influencing vacancy diffusion inside the matrix. Such attractive vacancy-solute binding energy can significantly reduce the mobility of vacancies and, thus, the annihilation rate of excess vacancies. The extended lifetime of excess vacancies ensures higher atomic diffusivity for longer aging times at low temperatures, which is a key factor in understanding the natural aging behaviour of Al alloys.

Fischer et al. [43], recently, developed a theory that describes the decrease of the total energy *G* of a system by traps with the binding enthalpies $\Delta E_k$:

$$G = G_0 + R_g T \left\{ \begin{array}{l} [y_{\mathrm{L}} \ln y_{\mathrm{L}} + (1 - y_{\mathrm{L}}) \ln(1 - y_{\mathrm{L}})] N_{\mathrm{L}} \\ \quad + \sum_{k=1}^{m} \left\{ [y_{\mathrm{T}k} \ln y_{\mathrm{T}k} + (1 - y_{\mathrm{T}k}) \ln(1 - y_{\mathrm{T}k})] N_{\mathrm{T}k} - \frac{\Delta E_k}{R_g T} y_{\mathrm{T}k} N_{\mathrm{T}k} \right\} \end{array} \right\} . \tag{20}$$

In our model, these relations are used to describe the interaction of different solutes with vacancies. The knowledge of the effective binding enthalpy $\Delta E_k$ between a trap of sort *k* and a vacancy enables to calculate the site fraction of trapped vacancies. This approach is reproduced briefly, next.

A system of $N_l$ moles of vacant positions in the crystal lattice and *m* different kinds of trapping elements is assumed, where the site fraction of the vacancies is $y_l$ and the site fraction of vacancies in a trap of sort *k* is $y_{Tk}$. The number of trapping positions per atom is *n*. In our case, each sort of trap involves *n*=12 possible trap positions in nearest neighbour positions of the fcc structure. The following relation holds:

$$\frac{y_l(1 - y_{Tk})}{y_{Tk}(1 - y_l)} = \exp\left( \frac{-\Delta E_k}{R_g T} \right) = K_k , \qquad k=1,...m, \tag{21}$$

where $R_g$ is the gas constant and *T* is absolute temperature.

Knowing *ΔE*$_k$, the trapping enthalpy of a vacancy to a solute atom, equation (25) can be resolved with respect to the site fraction of trapped vacancies, $y_{Tk}$, with:

$$y_{Tk} = \frac{y_l}{K_k + y_l(1 - K_k)}, \qquad k=1,\ldots,m. \tag{22}$$

The next case, in which the fractional concentration of solute atoms is high compared to the concentration of vacancies and in which the binding energy $E_{bind}$ of a single vacancy and a solute atom is attractive, is considered. Since the chance to encounter a solute atom is much higher than the chance of formation of di- or multi-vacancies, we neglect this possibility as well as the formation of voids (formation of vacancy-clusters).

Accordingly, the effective diffusion coefficient in the matrix, which is Al in the present case, is described by:

$$\widetilde{D}_{eq} = \left( D_L + \sum\nolimits_{k=1}^{m} D_{Tk} \left. \frac{dc_{Tk}}{dc_L} \right|_{x,t} \right) \left. \frac{dc_L}{dc} \right|_{x,t}, \tag{23}$$

$$\frac{dc_L}{dc} = \left[ 1 + \sum\nolimits_{k=1}^{m} \frac{V_L}{V_{Tk}} \frac{K_k}{\left[ K_k + V_L c_L (1 - K_k) \right]^2} \right]^{-1}, \tag{24}$$

$$\frac{dc_{Tk}}{dc_L} = \frac{V_L}{V_{Tk}} \frac{K_k}{\left[ K_k + V_L c_L (1 - K_k) \right]^2} \tag{25}$$

with:

| | |
|---|---|
| $D_L$ | effective diffusion coefficient (matrix element) in the lattice |
| $D_{Tk}$ | effective diffusion coefficient of trap element *k* |
| *m* | total number of trapping elements |
| $c_L$ | concentration of vacancies in the free lattice |
| $c_{Tk}$ | concentration of vacancies in the trap lattice |

| | |
|---|---|
| $V_L$ | volume of free lattice containing one mole of lattice atoms |
| $V_{Tk}$ | volume of trap lattice containing one mole of trap atoms |
| $K_k$ | equilibrium constant |

In this model, the contributions to the diffusion coefficient are separated into a free part and a trap part, which contains all the positions of the lattice in the vicinity of a trapping element.

The non-trapped fraction (amount of free vacancies) is considered to dominate the diffusion mechanisms at low temperatures.

***Example***: Influences of vacancy trapping on phase decomposition during natural aging.

Microalloying elements in aluminium alloys alter properties by changing the morphology, chemistry, structure and size of precipitates. In Al-Cu alloys, solute atoms clusters are formed in the very early stage of phase decomposition. In the case of Al-Cu alloys with Mg addition, rapid hardening occurs in a very short aging time at low temperatures [44]. It is proposed that the origin of the rapid hardening is related to the interaction between dislocations and Cu-Mg-Va complex clusters. Excess vacancies and their interaction to microalloying elements and solute atoms are important in the cluster formation as already discussed. Al-Cu alloys are one of the essential age-hardening alloys that produce solute clusters and in which the effect of several microalloying elements on the formation of clusters were first examined [44]. Such Microalloying elements are considered to affect the formation kinetics of clusters directly by their interaction with vacancies. The Monte Carlo simulation results for the Al-Cu base and Mg-added alloy are shown in Figure 13. Only the solute atoms are illustrated. With increasing Monte Carlos Steps (MCS), small clusters of Cu atoms are formed in both alloys.

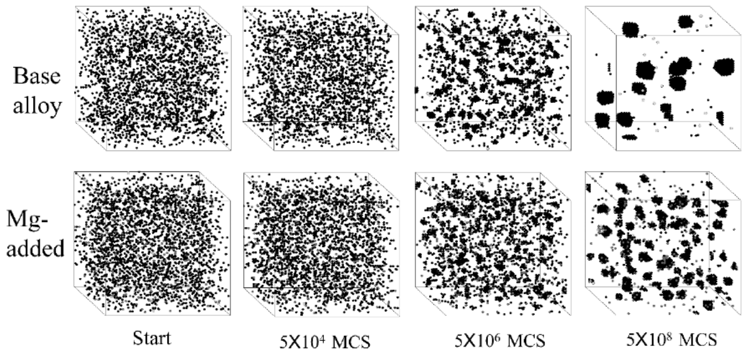

Figure 13: Monte Carlo simulation showing the evolution of clusters for Al-4wt.%Cu and Mg added alloys [44].

From Figure 13 it is obvious that the addition of Mg accelerates the nucleation of clusters and produces finer and more homogeneously distributed clusters than those in the base alloy. Vacancies are preferentially trapped by Mg atoms. The number of free vacancies in the Al-Cu-Mg system is decreased, suppressing Cu diffusion due to the vacancy trapping mechanism. Therefore, it can be concluded that the hardness increase in Mg-added Al-Cu and Al-Li-Cu alloys is due to the formation of more finely distributed clusters compared to the base Al-Cu and Al-Li-Cu alloys [44]. In the subsequent stage of the simulation, complex clusters containing Cu, Mg and vacancies are formed.

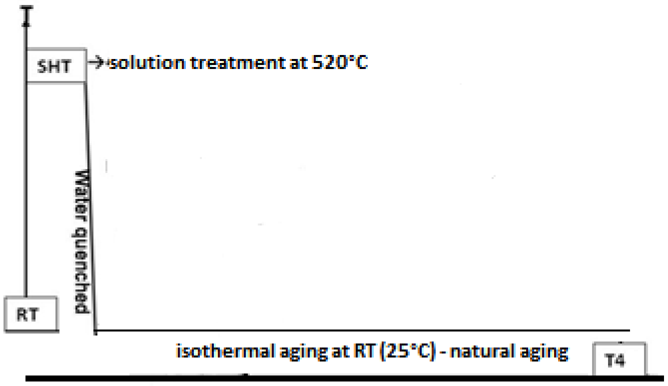

Figure 14: Heat treatment for Al-Cu and Al-Cu-Mg alloys, T4 condition.

Figure 14 shows the temperature-time regime: solution treatment at 520 °C, quenching in water and subsequent natural aging treatment at room temperature (RT) at 25 °C. Exemplarily, the following plots demonstrate the potential of our simulation on an Al–4.5 wt% Cu and a Al–4.0 wt.% Cu–1.5 wt.% Mg alloy during natural aging. In the following figure 15, the phase decomposition for the two alloys is presented, first.

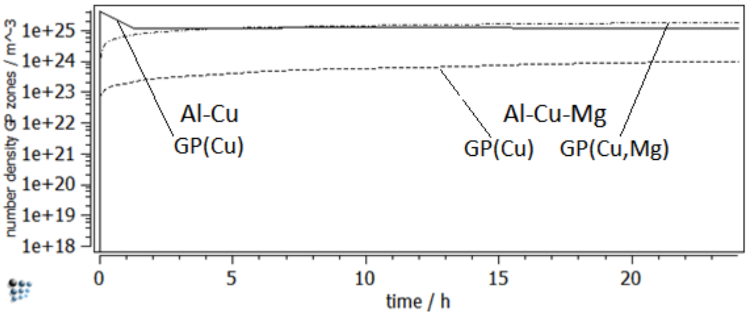

Figure 15: Phase decomposition in Al-Cu and Al-Cu-Mg alloys during natural aging.

In Figure 16, the evolution of the mean precipitate radii is shown. As already mentioned, the addition of Mg supports the nucleation of clusters and produces finer and more homogeneously distributed clusters than those in the Al-Cu base alloy. This behaviour is reflected in the thermo-kinetic simulations, showing that GP zones reach a mean diameter of about 2.3 nm in the Al–Cu alloy, whereas the GP zones (Al-Cu cluster and Al-Cu/Mg cluster) are distributed more finely in the Al–Cu–Mg system.

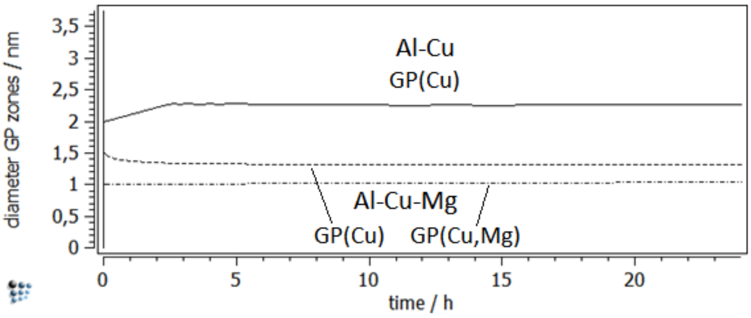

Figure 16: Evolution of mean diameter of GP zones in Al-Cu and Al-Cu-Mg alloys during natural aging.

Addition of Mg markedly retards hardening due to trapping of excess vacancies (Va binding to Mg and Cu/Mg aggregates). Diffusion corrections, based on the solid and cluster interaction with vacancies (trapped fraction), combined with simultaneous annihilation of free vacancies at different types of sinks are taken into account. The total amount of free excess vacancies, calculated by eq. (26), accelerates the mobility of the solute atoms. From Figure 17, we observe a free vacancy concentration of $\sim 1\cdot 10^{-5}$ and $6\cdot 10^{-9}$ direct after the quench step for Al–Cu and Al–Cu–Mg, respectively. The effective trapping behaviour of Mg and Cu/Mg aggregates contribute to a retardation of the response on aging in the Al-Cu-Mg system. The higher amount of free vacancies in the Al-Cu system is responsible for the more rapid aging behaviour of this kind of alloys. The more free vacancies, the faster the nucleation but also the subsequent reactions are accelerated. The high mobility of Cu in the vacancy supersaturated Al-Cu matrix results in faster dissolution of smaller Cu cluster and growth and coarsening of bigger ones. This growth and coarsening of precipitates leads to a decrease of strength already during natural aging (less but bigger precipitates).

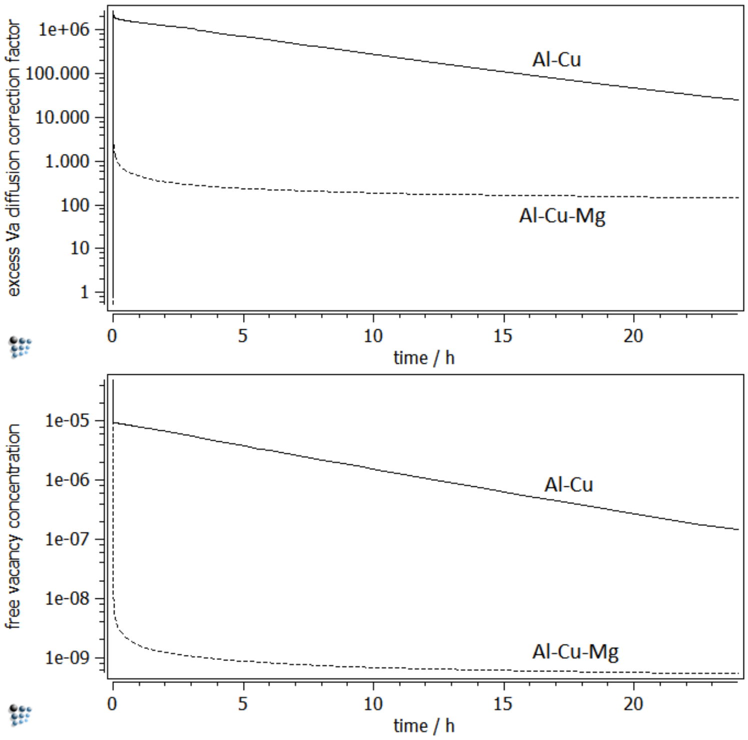

Figure 17: Diffusion correction factor (top) due to free excess vacancy concentration (bottom).

The smaller amount of free excess vacancies in the Al-Cu-Mg systems retards the growth and coarsening of the hardening GP zones and results in a higher level of yield strength due to finer dispersed particles as depicted Figure 18.

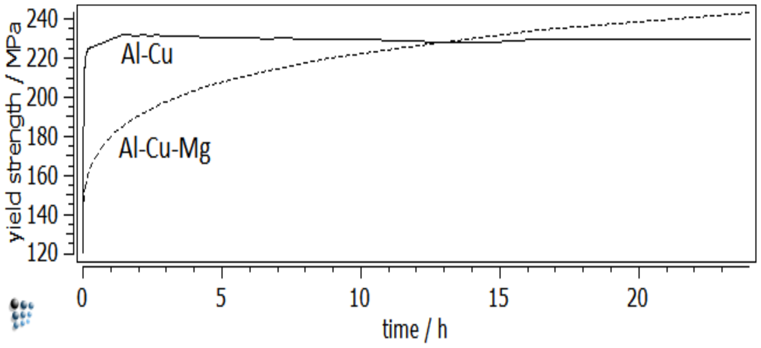

Figure 18: Evolution of yield strength of Al-Cu and Al-Cu-Mg alloy during natural aging.

## 3. Structure and energy calculations from atomistic simulation methods

First principles or ab initio modelling is a popular method for accurate quantum mechanics computing of complex material structures and properties. This approach, based on the Density Functional Theory (DFT), simplifies the Schrödinger equation in such a way that it can be approximately solved for structures in materials science. Ab initio modelling has become a standard technique in the modelling of materials at an atomic level. DFT is extensively used to compute important physical quantities, such as, formation enthalpies, crystal structure geometries, solid solution energies and strain energies. Thus, this approach is used to predict phase stability for the meta- and stable phases in the investigated Al alloys. The calculated enthalpies of formation of the specific phases are valuable input data for the thermodynamic description using the CALPHAD approach [16]. An example of a metastable phase diagram is given in Figure 19, showing the thermal stability of GP-zones, η‘ and η ($MgZn_2$) in an ternary Al-Zn-Mg system.

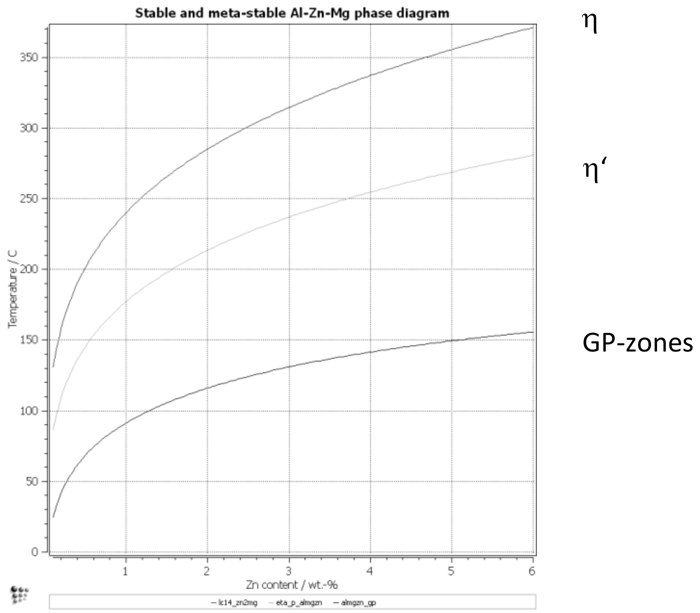

Figure 19: Metastable Al-Mg-Zn phase diagram, Mg = 1.5 wt.%, Zn = 0.0 - 6.0 wt.%, Al = balanced.

By using ab initio methods, it is also possible to calculate the energies of defects in systems. The energy of a structure containing defects e.g. that of vacant substitutional atomic sites and/or solute atoms, is compared to the undisturbed pure lattice. The theory to describe the interaction energies of a single vacancy to a solute atom and to a solute complex is described in ref. [45].

## 3.1 Enthalpy of formation

The ground state free energy is examined by applying a structural relaxation, which means that the geometry optimization of a certain crystal structure is carried out with the aim of finding the structural parameters that yield the global minimum free energy. This relaxation can be analysed in terms of energy to be found as a function of external and internal cell parameters. For a complete structural relaxation, first, the external degrees of freedom need to be relaxed. For this, a relaxation calculation of lattice parameters and angles between the lattice vectors is conducted to relieve the stresses and thus lower the free energy. By relaxing the cells internal degrees of freedom, the atoms are able to move in the cell and may leave their initial lattice position in the attempt to lower the total free energy. The atoms are moved individually in the direction of the calculated force vector until a certain minimum of the forces and energies is reached. The optimised structure gives the global minimum free energy.

The formation enthalpies of a structure α with composition $A_xB_y$ is described as:

$$\Delta H_{ref\ A,B}^{form}\left(A_x B_y^{\alpha}\right) = H\left(A_x B_y^{\alpha}\right) - xH\left(A^{ref\ A}\right) - yH\left(B^{ref\ B}\right), \tag{26}$$

where $H$ are the enthalpies, $x$ and $y$ represent the atomic fractions ($x + y = 1$) of the involved elements. $H(A^{refA})$ and $H(B^{refB})$ are the formation enthalpies of the reference (= ground-) states of the constituents in the system and $H(A_xB_x^{\alpha})$ is the enthalpy of the system in a certain configuration α. The formation enthalpy of the system is calculated by keeping the number of atoms of each species constant.

Generally, the following relationship between the enthalpies of the different metastable and stable phases in aluminium alloys is valid:

*H(solid solution) > H(intermediate precursor phases) > H(equilibrium phase).*

Metastable precipitates are formed during low temperature annealing of supersaturated solid solutions, which were formed by quenching from temperatures with higher solubility of the alloying elements in the matrix. Clusters or co-clusters are the first precipitates formed from the supersaturated solid solution. Guinier-Preston zones (GP-zones) are formed at room temperatures after a sufficient length of time. At elevated aging temperature, metastable precursor phases are formed. At even higher temperatures or after a sufficient length of time at elevated temperatures, the stable phases precipitate. The energy of all phases contributing to the whole precipitation-path can be calculated using DFT calculations. The results of the calculations, in particular the enthalpies of formation, *H*, are important input data to describe the thermo-dynamic properties of each phase.

### 3.2 Binding energy calculations

The binding energy, designated as $E$, to be distinguishable from formation enthalpies $H$, between vacancies and solute atoms or clusters is a key factor determining the kinetics and diffusion in substitutional alloys, where the atomic transport takes place by the direct exchange of a substitutional atom with a neighbouring vacancy. If a vacancy is attracted by individual solute atoms, these may act as vacancy traps and temporarily capture the vacancy on its way through the crystal, leading to a reduction in the total diffusivity in the system.

The binding energy of solute to vacancy can be calculated from the combination of four independent configurations with the following expression:

$$-E_{\text{bind}}(X - Va) = E(Al_{N-2}X_1Va_1) + E(Al_N) - E(Al_{N-1}X_1) - E(Al_{N-1}Va_1) \tag{27}$$

where $E(Al_N)$ is the total energy of a pure Al cell without *X* and *Va*, where the symbol *X* denotes solute atoms and *Va* a vacant position, respectively. $E(Al_{N-1}X_1)$ is the energy of the cell containing one solute atom only, $E(Al_{N-1}Va_1)$ is the energy with one vacancy and $E(Al_{N-2}X_1Va_1)$ is the energy of the system containing both, solute atom and vacancy in direct interaction with each other. Positive binding energies, $E_{\text{bind}}$, indicate attractive interaction between the vacancy and the foreign substitutional atom.

Table 1: Nearest-neighbor solute – vacancy binding energies (in eV) calculated for a 256 atom supercell .

| Solute | DFT-GGA This work | DFT | Exp. values |
|---|---|---|---|
| Mg | 0.026 | -0.02 [46]<br>0.01 [47] | <<0.01 – 0.40 [48]<br>0.00 – 0.10 [49] |
| Si | 0.032 | 0.08 [46]<br>0.05 [47] | 0.12 – 0.31 [48]<br>0.01 – 0.07 [49] |

Next the interaction of vacancies to the very first precipitates (dimer) is discussed. Assuming the very early co-clusters represent a combination of just two atoms, in the range of less than 1nm, they are, thus, beyond any present experimental detectability. The DFT calculated binding energies for different vacancy – cluster and for different vacancy – co-cluster constellations are summarized in Table 2. A cluster formed of two or more different alloying elements is termed co-cluster

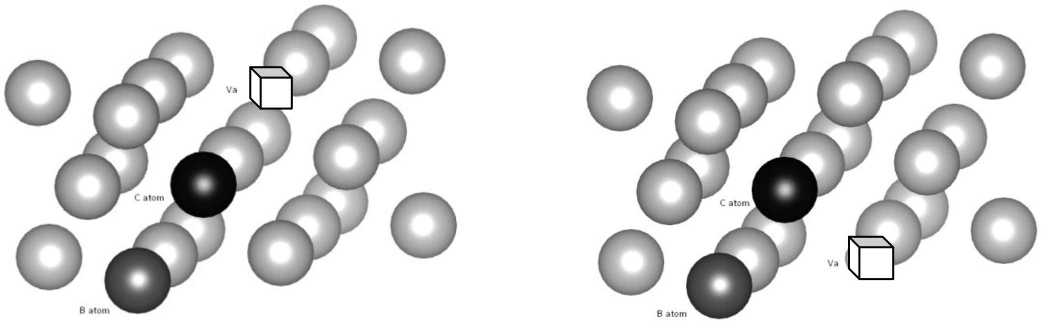

Figure 20: Arrangement of a co-cluster dimer; *Va* in row (left side), *Va* in triangle (right side). The vacancy is displayed by the white cube, the solute atoms by dark grey spheres. The matrix fcc lattice is represented by bright grey spheres.

Different geometries of the constellation of these *Va*- rich co-clusters (substitutional atoms $X_1$ + $X_2$ with 1 *Va* in row or triangle placement) are conceivable. Figure 20 shows a part of the simulation cell with two possible geometries considered. The location of the vacancy, as a next neighbour, is situated in a row or as a triangle arrangement with respect to the co-cluster dimer.

The reference state of the binding energies between a vacancy and a cluster is taken as the energy of the interaction between the solute atoms in the supercell without any vacancy interaction. The effective cluster – vacancy binding energy is given as:

$$\Delta E_{Va-Cluster,eff.-bind.} = E_{bind}(X_1 - X_2 - Va) - E_{bind}(X_1 - X_2). \tag{28}$$

with

$$E_{bind}(X_1 - X_2 -,..., X_n) = E(X_1 + X_2 + ... + X_n) + (n-1)E(Al_N) - \sum_{i=1,...,n} E(X_i) \tag{29}$$

$E_{bind}(X_1 - X_2 - Va)$ is the binding energy between a dimer ($X_1$, $X_2$ = substitutional elements) and a vacancy (*Va*), whereas $E_{bind}(X_1 - X_2)$ is the binding energy between the two substitutional elements, calculated with equation (33). The effective cluster – vacancy interaction energy gives an indication of the interaction effects; whether the vacancy (*Va*) is trapped by a co-cluster ($E_{X1+X2} > E_{X1X2+Va}$) or not ($E_{X1+X2} < E_{X1X2+Va}$).

Table 2: Ab-intio binding energies for vacancy - cluster interaction in a 256 atomic sites fcc supercell. The constellations with the highest positive interaction for each specific cluster type are shown in the left column, followed (left to right) by interactions with less attractive or repulsive binding energy. The Si atoms are displayed as white, Mg as black and Al as grey spheres. The vacancy is represented by the square.

| NN solute-solute atoms: $\Delta E_{Va\text{-}Cluster,eff.\text{-}bind.}$ (eV) | | |
|---|---|---|
| Reference: | **Si – Si cluster** ($E_{bind}$ = -0.158) |  |
| (Si-a) 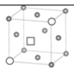<br>0.058 attractive | (Si-b) 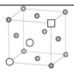<br>0.010 attractive | (Si-c) 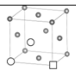<br>0.009 attractive |
| Reference: | **Mg – Mg cluster** ($E_{bind}$ = -0.030) |  |
| (Mg-a) 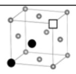<br>0.075 attractive | (Mg-b) 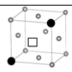<br>0.033 attractive | (Mg-c) 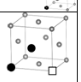<br>0.008 attractive |
| Reference: | **Mg – Si co-cluster** ($E_{bind}$ = 0.064) |  |
| (Mg/Si-a) 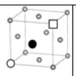<br>0.058 attractive | (Mg/Si-b) 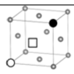<br>0.039 attractive | (Mg/Si-c)[a] 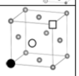<br>0.011 attractive |
| (Mg/Si-d) <br>-0.073 repulsive | (Mg/Si-e)[a] <br>-0.099 repulsive | |

[a] Mg and Si atom positions changed in reference system.

From Table 2, it is obvious that the interaction is attractive for all cases when a vacancy is located in nearest neighbour position of a Si-Si and a Mg-Mg cluster. Formation of a co-cluster in the form of a Mg-Si complex can compensate, in part, the mechanical stress field caused by the atomic size mismatch, showing already attractive binding energy between the Si and Mg atoms. Most investigated constellations of Mg-Si dimers (2-atom clusters) in the presence of one vacancy are energetically even more favourable compared to the case without vacancy.

# 4. Setup used for precipitation modelling

The precipitation reaction of metastable and stable phases in an aluminium matrix is a special case of phase transformation where the new phases grow at the expense of existing ones. In general, precipitation reactions occur when the amount of alloying elements exceeds their equilibrium solubility. Separate populations of metastable and stable precipitates are considered in the simulations, different in chemistry, coherency as well as in the type of nucleation site. Details on the individual simulation assumptions are reported in the publication part of this thesis. The numerical simulations are carried out using the nominal chemistry of the samples and the experimental parameters, such as time/temperature regime, grain sizes or deformation rates. Unfortunately, some input parameters for modelling are unknown from experiment, e.g. initial dislocation density. Therefore, some estimated values, conform to experimental evidence from literature, are used. An initial dislocation density of $10^{11}$ $m^{-2}$ is used for the unstrained, well-annealed aluminium matrix. Apart from the dependence on chemical composition and temperature, the phase decomposition reactions are strongly time-dependent and one must, therefore, look to kinetics. The precipitation process can be divided into three distinct stages:

- Nucleation: The initial stage in precipitate life. A stochastic process driven by microscopic thermal and compositional fluctuations.

- Growth: The controlled attachment of atoms to the precipitate. A deterministic process driven by chemical and/or mechanical driving forces.

- Coarsening: The dissolution of small precipitates in favour of larger ones, driven by curvature-induced pressure, also called the Gibbs-Thomson effect.

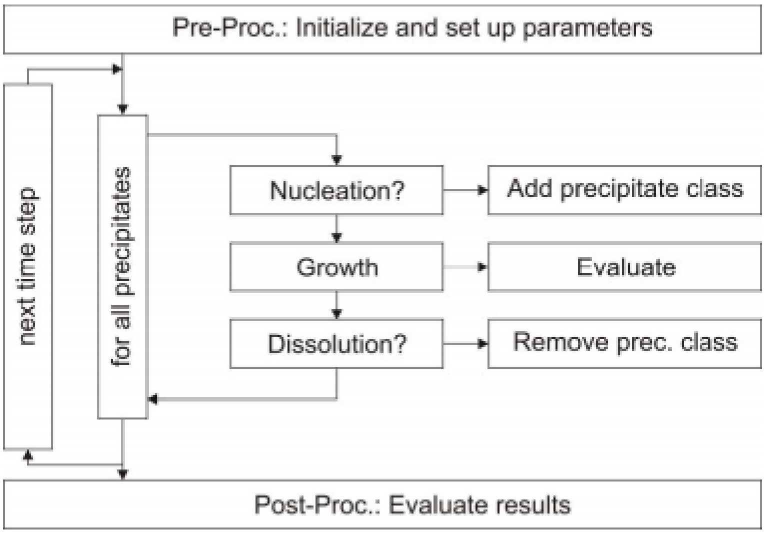

Figure 21: Flow chart of thermo-kinetic simulation [19]

The simulation procedure using MatCalc is as follows:

- Setup the thermodynamic system using the desired database, elements and phases.
- Define nominal chemical composition.
- Create the precipitation domain by selecting the corresponding thermodynamic matrix phase.
- Enter the microstructural information (grain size, dislocation density, subgrain size)
- Create desired precipitates and define desired number of size classes (this number will maintain the maximum number of size classes during the simulation run).
- Select the desired nucleation sites (homogeneous or heterogeneous nucleation) for each precipitate phase.
- Consider the appropriate models (i.e. evolution and influences of excess vacancies).
- Run the simulation program.
- Graphical presentation and interpretation of results.

# 5. Conclusions

The 6xxx and 7xxx series of aluminium alloys are suitable representatives of the precipitation- or age-hardenable alloys. During age-hardening treatment, precipitates form in a supersaturated solid solution. Strength increases as the number and sizes of different kinds of precipitates increase until a maximum in strength is reached. When the number density decreases and coarsening begins, the material becomes overaged and the strength is reduced again. Experimental work and simulations allow for the determination of the material's behaviour. Computational investigations then link mechanical properties to microstructural evolution and provide a better physical understanding of the mechanisms taking place inside the specimen. Precipitation evolution and hardening behaviour of Al-Mg-Si(-Cu) and Al-Zn-Mg(-Cu) has been studied, using a series of experimental tests on pure ternary alloys as well as on industrial alloys. Current physical models, based on nucleation, growth and coarsening models, applied to aluminium alloys, are introduced in the present work. Systematic study was done to determine the properties of the included solute elements and to describe the thermodynamics of metastable types of precipitate. The kinetic behaviour and characteristics of precipitates in Al 6xxx and Al 7xxx series are modelled, compared and validated by experimental findings. The effects of secondary precipitates, induced by rapid quenching, are presented in Part II (publications), including differential scanning calorimetry and age hardening simulations.

In conclusion, the simulation approaches, used in this study, address several important issues concerning precipitation reactions and microstructural evolution in heat treatable Al alloys, including excess vacancy annihilation and trapping phenomena during aging. The method provides an improved understanding of precipitation kinetics and hardening mechanisms in these types of alloys.

# References

[1] C.D. Marioara, S.J. Andersen, J. Røyset, O. Reiso, S. Gulbrandsen-Dahl, T.-E. Nicolaisen, I.-E. Opheim, J.F. Helgaker, R. Holmestad, Met. Mater. Trans. 45A (2014) 2938.

[2] J. Banhart, M. Liu, Y. Yong, Y. Liang, C.S.T Chang, M. Elsayed, M.D.H. Lay, Phys. B Condens Matter, 407 (2012) 2689.

[3] X. Wang, S. Esmaili, D.J. Lloyd, Met. Mater. Trans. 37A (2006) 2691.

[4] A. Gaber, N. Afify, M.S. Mostafa, Gh. Abbady, J. Alloys Comp. 477 (1-2) (2009) 295.

[5] A. Gaber, M.A. Gaffar, M.S. Mostafa, E.F. Abo Zeid, J. Alloys Comp. 429 (2007) 167.

[6] C. Cayron, P.A. Buffat, Acta Mater. 48 (2000) 2639.

[7] C.D. Marioara, S.J. Andersen, J. Jansen, H.W. Zandbergen, Acta Mater. 51 (2003) 789.

[8] G.C. Weatherly, A. Perovic, N.K. Mukhopadhyay, D.J. LLoyd, D.D. Perovic, Met. Mater. Trans. 32A (2001) 213.

[9] S.J. Andersen, C.D. Marioara, A. FrØseth, R. Vissers, H.W. Zandbergen, Mater. Sci. Eng. *A* 390 (2005) 127.

[10] S.J. Andersen, C.D. Marioara, R. Vissers, A. FrØseth, H.W. Zandbergen, Mater. Sci. Eng. *A* 444 (2007) 157.

[11] D.S. Thompson, B.S. Subramanya, S.A. Levy, Metallurgical Transactions 2 (1971) 1149.

[12] G. Sha, A. Cerezo, Acta Mater. 52 (2004) 4503.

[13] A. Deschamps. F. Livet, Y. Brechet, Acta Mater. 47 (1998) 281.

[14] J. Chen, L. Zhen, S. Yang, W. Shao, S. Dai, Mater. Sci. Eng. A 500 (2009) 34.

[15] Thermodynamic database for Al-systems, (mc_al.tdb, version 2.011), Institute of Materials Science and Technology, Vienna University of Technology, Austria.

[16] H.L. Lukas, S.G. Fries, B Sundman, Computational thermodynamics: the Calphad method, Vol. 131, Cambridge University Press (2007).

[17] Mobility database for Al-systems, (mc_al.ddb, version 2.004), Institute of Materials Science and Technology, Vienna University of Technology, Austria.

[18] J. Svoboda, F.D. Fischer, P. Fratzl, E. Kozeschnik, Mater. Sci. Eng. A 385 (1-2) (2004) 166.

[19] E. Kozeschnik, J. Svoboda, P. Fratzl, F.D. Fischer, Mater. Sci. Eng. A 385 (1-2) (2004) 157.

[20] K. Russell, Advances in Colloid and Interface Science 13 (1980) 205.

[21] A. Biswas, D.J. Siegel, C. Wolverton, D.N. Seidma, Acta Mater. 59 (2011) 6187.

[22] B. Sonderegger, E. Kozeschnik, Metallurgical and Materials Trans. A 40 (2009) 499.

[23] R. Kampmann, R. Wagner, Acta-Scripta Metallurgica Conference 91 (1983) 91.

[24] M.R. Ahmadi, E. Povoden-Karadeniz, K.I. Öksüz, A. Falahati, E. Kozeschnik, Comp. Mater. Sci. 91 (2014) 173.

[25] P. Lang, T. Weisz, M.R. Ahmadi, E. Povoden-Karadeniz, A. Falahati, E. Kozeschnik, Advanced Materials Research 922 (2014) 406-411.

[26] A.J. Ardell, Metall. Trans. 16A (1984) 2131.

[27] OR. Myhr, Ø. Grong, SJ. Andersen, Acta Mater. 49 (2001) 65.

[28] P. Sherstnev, P. Lang, E. Kozeschnik, Proc. ECCOMAS 2012 - European Congress on Computational Methods in Applied Sciences and Engineering (2012) 5331.

[29] G.I. Taylor, Proc. Roy. Soc. A 145 (1934) 362.

[30] H. Mecking, U.F. Kocks, Acta Metall. 29 (1981) 1865.

[31] U.F. Kocks, H. Mecking, Prog. Mater. Sci. 48 (2003) 171.

[32] L.E. Lindgren, K. Domkin, S. Hansson, Mechanics of Materials, 40 (2008) 907.

[33] F. Roters, D. Raabe, G. Gotstein, Acta Materialia 48 (2000) 4181.

[34] S. Brinckmann, R. Sivanesapillai, A. Hartmaier, International Journal of Fatigue 33 (2011) 1369.

[35] M.S. Soliman, E.A. El-Danaf, A.A. Almajid, Advanced Materials Research 83-86 (2009) 407.

[36] R. Radis, E. Kozeschnik, Modelling and Simulation in Materials Science and Engineering, 18 (2010) 055003.

[37] K.I. Aastorp, Norwegian University of Science and Technology (NTNU), thesis (2002)

[38] P. Lang, Y.V. Shan, E. Kozeschnik, Materials Science Forum 794-796 (2014) 963.
[39] D. Hull and D.J. Bacon: Introduction to dislocations, Elsevier Ltd., (2001)
[40] H.P. Stüwe, Acta Metallurgica 13 (1979) 1965.
[41] F.D. Fischer, J. Svoboda, F. Appel, E. Kozeschnik, Acta Mater. 59 (2011) 3463.
[42] R.O. Simmons, R.W. Balluffi, Physical Review 117 1 (1960) 52.
[43] F.D. Fischer, J. Svoboda, E. Kozeschnik, Model. Simul. Mater. Sci. Eng. 21 (2013) 025008 (13p).
[44] T. Sato, S. Hirosawa, K. Hirose, T. Maeguci, Metallurgical and Materials Transaction A 34 (2003) 2745.
[45] P. Lang, P. Mohn, A. Falahati, E. Kozeschnik, Proc. 13th International Conference on Aluminum Alloys ICAA13 (2012) 273.
[46] C. Wolverton; Acta Mater. 55 (2007) 5867.
[47] D. Simonovic, M.H.F. Sluiter, Phys. Rev. B 79 (2009) 054304.
[48] L.F. Mondolfo, Aluminium alloys: Structure and Properties, Butterworth&Co, London, 1976.
[49] P. Ehrhart, SpringerMaterials - The Landolt-Börnstein Database (http://www.springermaterials.com) DOI: 10.1007/10011948_57.

# Part II

## Referenced publications

Peter Lang

## Contents

1. P. Lang, P. Mohn, A. Falahati, E. Kozeschnik, “*Ab initio simulations of vacancy-solute clusters in Al-Mg-Si and Al-Zn-Mg alloys*“, Proc. 13th International Conference on Aluminum Alloys ICAA13 (2012) 273-277.

2. P. Lang, Y.V. Shan, E. Kozeschnik, “*The life-time of structural vacancies in the presence of solute trapping*“, Materials Science Forum 794-796 (2014) 963-970.

3. P. Lang, E. Povoden-Karadeniz, A. Falahati, E. Kozeschnik, “*Simulation of the effect of composition on the precipitation in 6xxx Al alloys during continuous-heating DSC*“, Journal of Alloys and Compounds (2014) 443-449.

4. P. Lang, T. Wojcik, E. Povoden-Karadeniz, A. Falahati, E. Kozeschnik, “*Thermo-kinetic prediction of metastable and stable phase precipitation in Al-Zn-Mg series aluminium alloys during non-isothermal DSC analysis*“, Journal of Alloys and Compounds 609 (2014) 129-136.

5. P. Lang, T. Weisz, M.R. Ahmadi, E. Povoden-Karadeniz, A. Falahati, E. Kozeschnik, “*Thermo-kinetic simulation of the yield strength evolution of AA7075 during natural aging*”, Advanced Materials Research 922 (2014) 406-411.

6. P. Lang, M. Rath, P. Sherstnev, E. Kozeschnik, “*Simulation of the plastic deformation response of AA 6082 in W condition*”, Materials Science and Engineering A (2014) under review.

**13th International Conference on Aluminum Alloys (ICAA13)**
*Edited by: Hasso Weiland, Anthony D. Rollett, William A. Cassada*
***TMS (The Minerals, Metals & Materials Society), 2012***

# Ab initio simulations of vacancy-solute clusters in Al-Mg-Si and Al-Zn-Mg alloys.

Peter Lang[1], Peter Mohn[2], Ahmad Falahati[3], Ernst Kozeschnik[3,4]

[1]MCL (Materials Center Leoben Forschung GmbH, Roseggerstraße 12, Leoben, 8700, Austria
[2]Institute of Applied Physics, Vienna University of Technology, Gusshausstraße 25-25a, Vienna, 1040, Austria
[3]Institute of Materials Science and Technology, Vienna University of Technology, Favoritenstraße 9-11, Vienna, 1040, Austria
[4]Christian Doppler Laboratory "Early Stages of Precipitation", Vienna University of Technology, Favoritenstraße 9-11, 1040, Austria

Modeling, co-cluster, Al-Mg-Si, Al-Zn-Mg

## Abstract

The coherent fcc (face-centred-cubic) based cluster stability of Al-Mg-Si and Al-Zn-Mg alloys is studied theoretically using augmented plane wave density functional theory calculations of a periodically repeated supercell containing 32 atoms. In particular, the presence of vacancies within the structure of $Mg_a$-$Si_b$±$Va_c$ and $Zn_d$-$Mg_e$±$Va_f$ clusters is investigated in detail. These fcc type arrays of solutes are considered to bind with vacancies.

The binding energies between two substitutional elements, Mg and Si as well as Zn and Mg, and same arrangements bound to one vacancy in a fcc aluminium matrix are calculated. The binding energies of the co-clusters are taken as reference energies to compare the binding energies of two atom co-clusters to a vacancy in different constellations. These energies are used to predict formations of very early clusters containing single vacancies. Energetically more favourable structures are obtained and discussed.

## Introduction

Due to the continuing need for weight reduction, precipitation-hardenable Al alloys are widely used in automotive- and aircraft industry. Strengthening of these metallic alloys is mostly dependent on the presence of metastable second phases. The formation of such solute-rich precipitates is a process of great technological importance because these particles hinder the motion of dislocations and give raise to hardening in 6xxx and 7xxx aluminum alloys.

Several metastable structures can appear from the supersaturated solution after or even during a quenching process from a high temperature (solutionizing, temperature close to melting point) to room temperature (RT) before ultimately the stable phase(s) start to form and the strength decreases again (over-aged situation). In the case of Aluminum alloys, the very first precipitates are assumed to be co-clusters and are very small in the range of less than one nm. The Term co-clusters is used if the cluster is formed involving two or more alloying elements. Due to difficulties in experimental analysis of such co-clusters, we investigate the co-cluster as dimer (2 atom co-cluster) in theoretical terms only. High resolution transmission electron microscopy (HRTEM) techniques or atom probe experiments might be able to reveal the existence of co-clusters aggregates with more than 10 atoms. Indication of the predicted co-clusters is given by the changes of the heat flow in continuous-heating differential scanning calorimetry (DSC) experiments of quenched Al alloys [1] and can be related to the formation and dissolution of metastable phases.

After solution annealing and quenching, co-clusters start forming first in the highly vacancies (Va) supersaturated solid solution (SSSS). The cluster formation process can be described as follows:

During, or shortly after the quenching process, a single quenched-in vacancy moves through the crystal and may encounter a B or C atom. If the binding energy between the vacancy and the B or C atom is positive, a B- or C-Va complex will form. The lifetime of the complex depends strongly on the strength of the binding energy. The stronger the attraction between B or C atom and the Va is, the longer is the lifetime of the complex. This complex may migrate further and if it encounters another B or C atom, some of these atoms could join the complex. With increasing number of atoms, the complex becomes more stable and could be described as a stationary cluster when reaching a certain number of B and C atoms. The vacancy might still be trapped within the cluster. When cluster growth continues, it might be energetically favourable that the Va leaves the cluster again.

In the present work, we investigate the formation of co-clusters (Mg-Si and Zn-Mg co-clusters in a surrounding fcc Al matrix). The substitutional atoms are placed in the respective next neighbour shell and the total energy of the system is determined from ab initio calculations. Then, a single vacancy is incorporated into the structure and the energies of different co-cluster constellations in the presence of one Va is compared to the binding energy of the co-cluster without the Va in the next neighbourhood.

## Electronic structure calculations

In our density functional theory (DFT) electronic structure simulations, we use the Vienna ab initio simulation package (VASP) in the plane-wave pseudo potential implementation. We assume the very early co-clusters to represent a combination of just two atoms, which are in the range of less than 1nm and are, thus, beyond any present experimental detectability. Using APFIM (atom probe field ion microscopy), Edwards [2] postulated the formation and dissolution of Si- and Mg-clusters preceding the formation of co-clusters. Murayama and Hono [3] reported that the Mg:Si ratio in the Mg-Si co-clusters is close to one. Sha and Cerezo [4] investigated the early-stage precipitation in Al-Zn-Mg-Cu alloys and indicate the composition ratio as being approximately Zn/Mg = 1. Co-cluster compositions cumulate around Mg:Si and Zn/Mg =1:1 for both 6xxx and 7xxx aluminum alloys. Hence, in our simulations, the ratio of A:B elements is set to be 1 within the fcc structure of the surrounding Al matrix. The letter A stands for Mg or Zn, whereas B denotes Si or Mg.

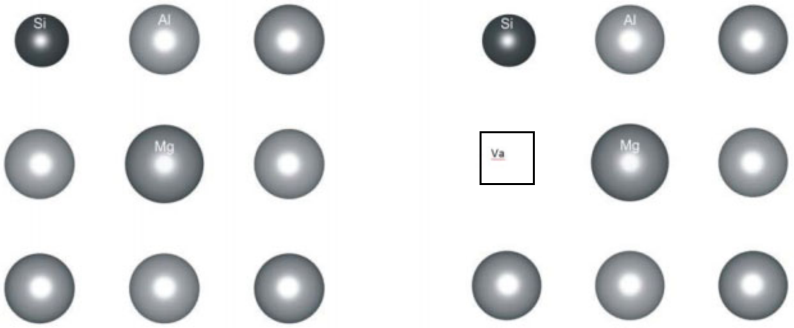

Figure 1. Mg-Si co-cluster (left), Mg-Si-Va co-cluster

The simulation procedure using VASP [5,6,7] is outlined as follows:

- Create a perfect crystal. Calculate the total energy of the pure Al system.
- Remove two atoms and replace two different (Mg+Si / Zn+Mg) substituting elements.
- Remove three atoms and replace two different (Mg+Si / Zn+Mg) substituting elements with one vacancy in the next neighbour shells.
- Relax the system with respect to volume as well as all cell-internal atomic coordinates.
- Evaluate energy states based on different cluster structures.
- Compare the total energies of the different configurations.

For the 32 atom supercell, the k-grid was set to 20x20x20. The electronic structure is calculated using the projected augmented wave (PAW) pseudo-potentials [8,9]. Effects of exchange and correlation are treated within the generalized gradient approximation (GGA) of Perdew, Burke and Ernzerhof (-PBE) [10]. All structures are fully relaxed with respect to volume as well as all cell internal atomic coordinates. Energy convergence was ascertained to limit the uncertainty to less than 1meV/atom.

Figure 2 shows a part of our simulation cell with the two geometries considered. The location of the vacancy, as a next neighbour, is situated either as a row or as a triangle arrangement with respect to the co-cluster dimer.

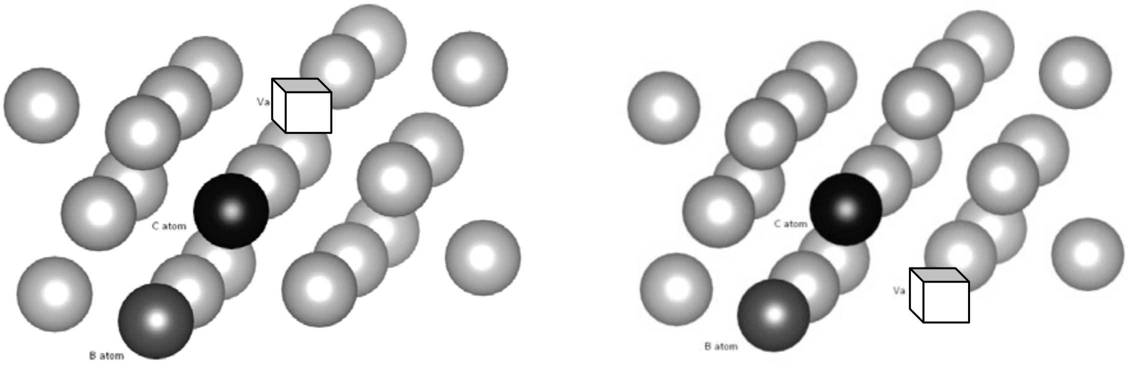

Figure 2. Arrangement of co-cluster dimer; Va in row (left side),
Va in triangle (right side) structure

The binding energy between vacancies and solute atoms or clusters is a key factor in determining the kinetics of diffusion in substitutional alloys, where the atomic transport takes place by the direct exchange with a neighboring vacancy. If the vacancy is attracted by individual solute atoms or clusters, they may act as vacancy traps and temporarily capture the vacancy on its way through the crystal. The results of our calculations thus yield an indication for such effects whether the vacancy is trapped by a co-cluster ($E_{A1+B1} > E_{A1B1+Va1}$) or not ($E_{A1+B1} < E_{A1B1+Va1}$). Within the 32 atom supercells, different geometries of the arrangements of these co-clusters (substitutional atoms A + B with 1 Va in row or triangle arrangement) are investigated and the binding energies are compared in order to determine energetically favored structures.

Calculation of the binding energy: Our calculation gives the total energies (enthalpies) at T=0K of the different systems and allows to determine the thermodynamic stability. The binding energy, formulated as differences of enthalpies, is defined as

$$\Delta E^{bind}_{refA,B,C,Va}(A_x B_y C_z Va) = E(A_x B^{\alpha}_y C^{\alpha}_z Va) - E(N-1+B) - E(N-1+C) - E(N-1+Va) - (n-1)E^{pure\_A} \quad (1)$$

where $x$, $y$ and $z$ are the atomic fractions. $N$ represents the number of atoms in the system; $n$ indicates the number of systems. The formation energy is defined to compare the enthalpy of a system in a certain configuration with the enthalpies of the matrix containing single defects (substitutional atom B or C or one vacancy). When the binding energy of the system in a certain configuration is positive, there is an energy gain with respect to the structures containing only one defect. This case indicates preferred structures.

## Results

The calculations predict that some co-clusters are energetically more favourable when a vacancy is included to their dimer arrangements. In particular for the Al-Mg-Si system most of the arrangements show attractive interaction between Mg-Si co-cluster and one Va. The constellation where the Va is next to the Mg atom, sitting in row, shows repulsive interaction energies. For the system Al-Zn-Mg just the dimer structures, where the Va is nearest to the Zn atom give positive binding energy, indicating favourable binding. The results of the ab initio calculations are summarized in Table 1. The binding energy of the A-B atoms of the co-cluster is taken as reference value and therefore set to 0. Energies are given in kJ/mol.

● A atom: for system Al-Mg-Si….. Mg; for system Al-Zn-Mg…..Mg

○ B atom: for system Al-Mg-Si…..Si; for system Al-Zn-Mg…..Zn

☐ vacancy

Table I. Calculated energies in kJ/mole for different dimer constellations.

| 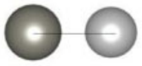 | 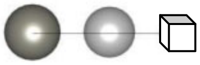 | 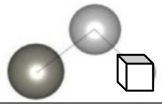 | 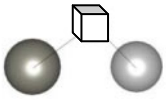 | 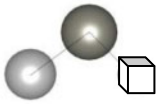 |  |
|---|---|---|---|---|---|
| A-B co-cluster | A-B-Va row | A-B-Va triangle | A-Va-B triangle | B-A-Va triangle | B-A-Va row |
| | | | | | |
| System Al-Mg-Si | | | | | |
| 0 | 11.9 | 6.4 | 1.8 | 2.8 | -8.5 |

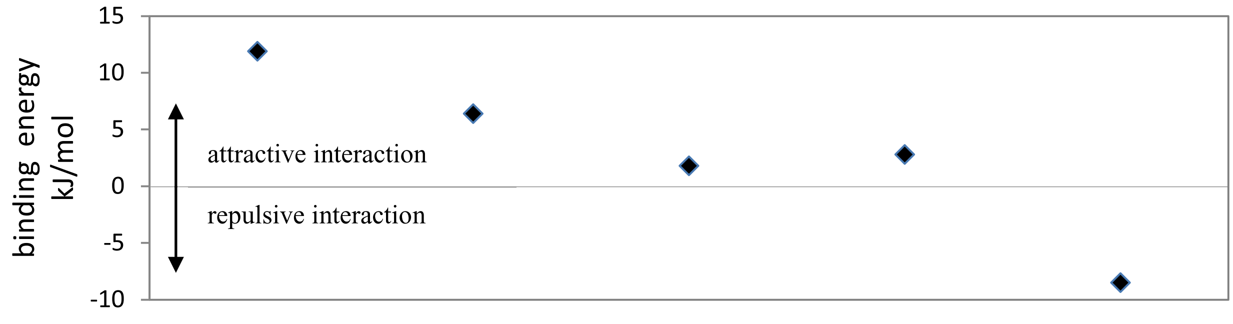

| | | | | | |
|---|---|---|---|---|---|
| Remarks | Most stable: Va next to Si | | | | |
| System Al-Zn-Mg | | | | | |

<table>
<tr><td>0</td><td>- 3.7</td><td>1.8</td><td>-5.3</td><td>-6.3</td><td>-2.5</td></tr>
<tr><td colspan="6">
</td></tr>
<tr><td>Remarks</td><td>Most stable:<br>Va next to Zn</td><td></td><td></td><td></td><td></td></tr>
</table>

## Conclusions

The binding energies of very early clusters containing single vacancies in fcc-based structures are calculated. The results show that, for co-clusters formed by 2 atoms with an A:B ratio of 1, some arrangements with a single vacancy included are energetically favoured. More specifically, the calculations predict that, in Al-Mg-Si alloys, the formation with the vacancy next to Si in row is the most favourable whereas the vacancy binding energy is repulsive if the vacancy is placed next to the Mg atom. For Al-Zn-Mg alloys, the vacancy prefers to sit next to a Zn atom.

## Acknowledgements

Financial support by the Austrian Federal Government (in particular from the Bundesministerium für Verkehr, Innovation und Technologie and the Bundesministerium für Wirtschaft, Familie und Jugend) and the Styrian Provincial Government, represented by Österreichische Forschungsförderungsgesellschaft mbH and by Steirische Wirtschaftsförderungsgesellschaft mbH, within the research activities of the K2 Competence Centre on “Integrated Research in Materials, Processing and Product Engineering”, operated by the Materials Center Leoben Forschung GmbH in the framework of the Austrian COMET Competence Centre Programme, is gratefully acknowledged.
The computational results have been achieved using the Vienna Scientific Cluster (VSC).
E.K. and P.M. acknowledge support by the Austria Science Fund (FWF) within the SFB ViCom F4109 and F4110.

## References

1. Starink M J, Wang S C, Acta mater. 2009;57;2382
2. Edwards GA, et al, Acta mater. 1998;48;3893
3. Murayama M, Hono K, Acta mater. 1999; 47;1537
4. Sha G, Cerezo A, Acta mater 2004;52;4503
5. Kresse G, Hafner J, Phys Rev B 1993;47;558
6. Kresse G, Hafner J, Phys. Rev. B 1993; 48; 13115
7. Kresse G, Thesis, Technische Universität Wien, 1993
8. Blöchl PE, Phys. Rev. B 1994;50;17953
9. Kresse G, Joubert J, Phys. Rev. B 1999;59;1758
10. Perdew JP, Burke K, Ernzerhof M, Phys. Rev. Lett. 1996;77;3865

*Materials Science Forum Vols. 794-796 (2014) pp 963-970*
*© (2014) Trans Tech Publications, Switzerland*
*doi:10.4028/www.scientific.net/MSF.794-796.963*

# The life-time of structural vacancies in the presence of solute trapping

Peter Lang[1,2,a*], Yao V Shan[1,2,b] and Ernst Kozeschnik[2,3,c]

[1] Materials Center Leoben Forschungsgesellschaft mbH, Leoben, Austria
[2] Institute of Materials Science and Technology, Vienna University of Technology, Vienna, Austria.
[3] Christian Doppler Laboratory “Early Stages of Precipitation”, Vienna University of Technology, Vienna, Austria.

[a]peter.lang@tuwien.ac.at, [b]yao.shan@tuwien.ac.at, [c]ernst.kozeschnik@tuwien.ac.at

**Keywords**: vacancies, solute trapping, modelling

## Abstract

Vacancies are the simplest type of lattice defect. However, they play a major role in the kinetics of diffusional processes, such as solid-state precipitation, where mass transport is directly proportional to the concentration of vacancies. We present a physical modelling framework, where we simulate the evolution of excess vacancies on the example of Al-alloys during simplified time-temperature treatments. Interaction energies between solute atoms and vacancies are evaluated by first-principle analysis. Assuming that the escape of vacancies from existing traps is dependent on temperature and binding energies, we explore the life-time of non-equilibrium vacancies and the natural and artificial aging response of Al alloys. The predictions of the model are finally compared to experimental data.

## Introduction

At a given temperature, each solid-state system contains a characteristic concentration of equilibrium structural vacancies, which influence significantly the thermodynamic and kinetic behaviour during manufacturing and processing. Diffusional mass transport by vacancies is the most important mechanism for precipitation, with the vacancies controlling the reaction rate inside the matrix. In most materials, the vacancy concentration at a given temperature follows an Arrhenius dependence. The mole fraction of equilibrium vacancies is in the order of $10^{-4}$ close to the melting point and decreases upon cooling. The vacancies present in equilibrium amount are called thermal vacancies.

The absolute vacancy concentration in a solid material as a function of temperature, time and processing conditions depends strongly on the vacancy formation enthalpy, the applied cooling rates and on the strength of interaction between vacancies and solute atoms and/or complexes in solid solutions. With the help of simulations and based on proper physical models, the total amount and evolution of vacancies in Al alloys can nowadays be predicted on the researchers desktop. Calculation methods, such as first-principle investigations based on density functional theory (DFT), play an important role in this aspect and they are inevitable in improving the understanding of the interactions between vacancies and impurities. The calculated values, in particular the binding energy, are essential in determining the kinetics of diffusion to predict the formation and growth of early clusters or co-clusters in heat treatable Al alloys.

The purpose of the present work is to study the kinetic response of Al-alloys to the vacancy mobility under different boundary conditions, such as chemical composition or temperature profiles, based on binding energies obtained from ab initio calculation. All calculations are performed with the thermo-kinetic software package MatCalc (version 5.53.0031), the thermodynamic database mc_al_v2.002.tdb and the kinetic database mc_al_v2.002.ddb

## Kinetic Equations

The equilibrium concentration of vacancies, $y_{0,eq}$, is predominantly temperature-dependent and it is given by

$$y_{0,eq} = \exp(-G_0 / R_g T) \tag{1}$$

with $G_0$ being the vacancy formation free energy and $R_g$ being the gas constant.

Vacancies are annihilated and generated at appropriate sinks and sources such as dislocation jogs, incoherent interfaces, grain boundaries and free surfaces. When a metal is heated and held at elevated temperature, the amount of structural vacancies increases rapidly to its equilibrium value. In the opposite direction, on cooling, time may not be sufficient, however, for the vacancies to reach the nearest vacancy sinks. Thus, annealing and rapid quenching may lead to states with a high amount of non-equilibrium quenched-in vacancies. The following models, derived by Fischer et al. [1], are implemented in the thermo-kinetic software tool MatCalc [2-4] and they are used for the present simulations.

Two models corresponding to two different annihilation mechanisms are utilized mainly and explained here briefly. The first is the annihilation and generation of excess vacancies at homogeneously distributed dislocation jogs (DJ) with constant density. The second is the annihilation of excess vacancies at grain boundaries (GB) with radius $R$. The vacancy generation / annihilation rates are denoted as $\dot{y}_0^{DJ}$ and $\dot{y}_0^{GB}$, and they are given by [1]

$$\dot{y}_0^{DJ} = -\frac{2\pi a H y_0 \widetilde{D}_{eq}}{y_{0,eq} f}\left(\ln\frac{y_0}{y_{0,eq}} - \frac{\Omega}{R_g T}\sigma_H\right) \tag{2}$$

and

$$\dot{y}_0^{GB} = -\frac{15 y_0 \widetilde{D}_{eq}}{y_{0,eq} f R^2}\left(\ln\frac{y_0}{y_{0,eq}} - \frac{\Omega}{R_g T}\left(\sigma_H - \frac{\gamma_b}{R}\right)\right) \tag{3}$$

where:

| | |
|---|---|
| $a$ | interatomic spacing |
| $H$ | jog density of homogeneously distributed jogs |
| $y_{0,eq}$ | equilibrium site fraction of vacancies |
| $y_0$ | actual non equilibrium site fraction of vacancies |
| $\widetilde{D}_{eq}$ | effective diffusion coefficient of the matrix-forming element (here: Al) |
| $f$ | geometrical correlation factor, for fcc it is equal to 0.7815 |
| $\Omega$ | matrix molar volume corresponding to one mole of lattice sites |

| | |
|---|---|
| $\sigma_H$ | hydrostatic stress, which corresponds to the external pressure (if applicable) |
| $\frac{\gamma_b}{R}$ | surface stress contribution from the grain boundary energy |

We will next consider the case, in which the fractional concentration of solute atoms is high compared to the concentration of vacancies and in which the binding energy $E_{bind}$ of a single vacancy and a solute atom is attractive. Since the chance to encounter a solute atom is much higher than the chance of formation of di- or multi-vacancies, we neglect this possibility as well as the formation of voids (formation of vacancy-clusters). The binding energies describing the solute-vacancy interactions are calculated with density functional theory. A detailed description of the calculation procedure is given in ref. [5].

Table 1: Calculated nearest-neighbor solute-vacancy binding energies

| Solute-vacancy | First-principle value, present work [eV] |
|---|---|
| Mg – Va | 0.026 |
| Si – Va | 0.033 |
| Zn - Va | 0.032 |
| Sn - Va | 0.281 |

For implementation of these values into thermo-kinetic simulations, the recently developed model of Fischer et al. [6] for trapping of interstitial atoms at substitutional traps is used as a first approximation. Accordingly, the effective diffusion coefficient in the matrix, which is Al in the present case, is described by

$$\widetilde{D}_{eq} = \left( D_L + \sum\nolimits_{k=1}^{m} D_{Tk} \left. \frac{dc_{Tk}}{dc_L} \right|_{x,t} \right) \left. \frac{dc_L}{dc} \right|_{x,t} , \tag{4}$$

$$\frac{dc_L}{dc} = \left[ 1 + \sum\nolimits_{k=1}^{m} \frac{V_L}{V_{Tk}} \frac{K_k}{[K_k + V_L c_L (1-K_k)]^2} \right]^{-1} , \tag{5}$$

$$\frac{dc_{Tk}}{dc_L} = \frac{V_L}{V_{Tk}} \frac{K_k}{[K_k + V_L c_L (1-K_k)]^2} \tag{6}$$

with

| | |
|---|---|
| $D_L$ | effective diffusion coefficient (matrix element) in the lattice |
| $D_{Tk}$ | effective diffusion coefficient of trap element *k* |
| $m$ | total number of trapping elements |
| $c_L$ | concentration of vacancies in the free lattice |
| $c_{Tk}$ | concentration of vacancies in the trap lattice |
| $V_L$ | volume of free lattice containing one mole of lattice atoms |
| $V_{Tk}$ | volume of trap lattice containing one mole of trap atoms |
| $K_k$ | equilibrium constant |

In this model, the contributions to the diffusion coefficient are separated into a free part and a trap part, which contains all the positions of the lattice in the vicinity of a trapping element. The interested reader is referred to the original work, where the full evaluation of the parameters is described.

## Vacancy Evolution during Quenching

When a specimen, after having been annealed at a relatively high temperature $T_1$, is quenched to some lower temperature $T_2$, imperfections, such as vacancies, in thermal equilibrium at high temperatures, can be frozen-in at low temperature. Solute atoms or complexes can then trap some of these excess vacancies. The non-trapped fraction (free vacancies) is considered to dominate the diffusion mechanisms at low temperatures.

In the following, a parameter study is presented, where the values of the binding energies $E_b$ between a single vacancy and a solute atom are taken to be 0.1, 0.2 and 0.3 eV, respectively. The matrix system is Al with 0.001 at.% of a substitutional element in solid solution. The grain size of the dilute Al alloy is taken to be 1 mm, the dislocation density is set to $10^{11}$ $m^{-2}$. We assume that the density and efficiency of sinks (grain boundaries and dislocations) remains constant and do not change during the quench. The annealing temperature is 400°C. The specimen is cooled to room temperature with a quenching rate of $10^4$ °C/s. The concentrations of the free vacancies $c_{vf}$, the ones which are not trapped, as well as the trapped fraction $c_{vt}$ of the total vacancy amount are plotted in Fig. 1.

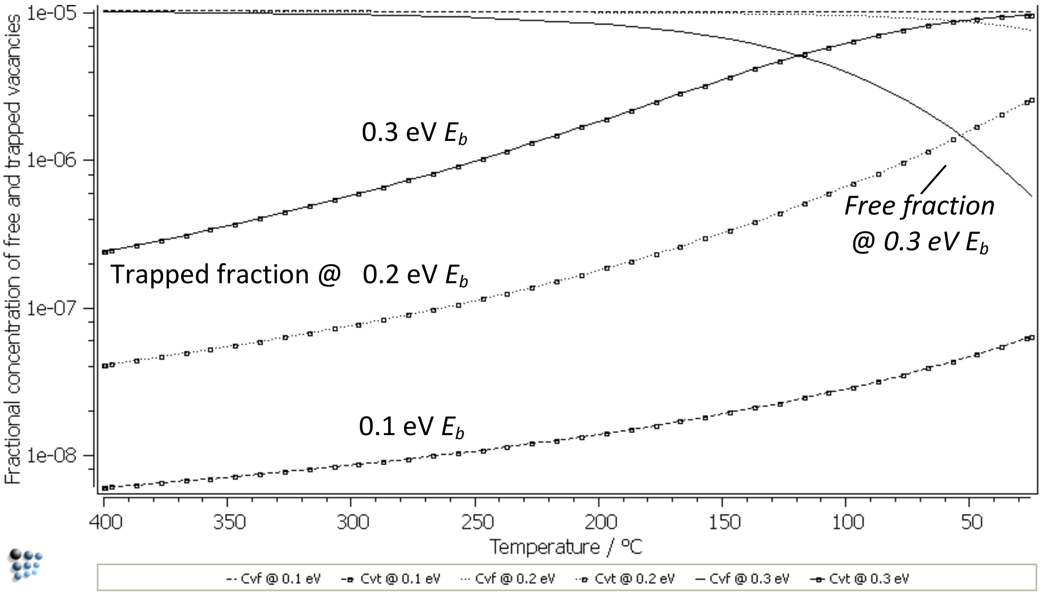

Figure 1: The change of free and trapped vacancy concentration during quenching in dilute aluminium alloys with a trap density of 0.001at.%.

The total vacancy concentration at 400°C is calculated to be about $1.05 \cdot 10^{-5}$. The higher the binding energy, the more and faster the trapping of single vacancies at possible trapping positions, such as solute atoms, occurs. Therefore, less free vacancies are actually present to increase the diffusivity of the system at low temperatures. The traps with 0.3 eV binding energy to a single vacancy represent almost irreversible trapping positions, as the vacancy is not or just very hardly, after very long time, able to escape from this deep trap at room temperatures. For the given microstructure and alloying content, the trapped fraction correlated to a binding energy of 0.3 eV (solute – vacancy interaction), is almost equal to the free fraction of the total vacancy concentration at a temperature of 120°C, as shown in Fig. 1. As quenching goes on, the fraction of trapped vacancies increases and nearly all vacancies, which have been generated at the annealing temperature, are captured at the deep traps at room temperature.

In practical experiments, the cooling rate is finite and the vacancies can migrate and annihilate at appropriate sinks during quenching. Fig. 2 shows the simulated evolution of the equilibrium and the total vacancy concentration during quenching in pure Al (100% Al) for a T1 of 600°C (solutionizing) and a quenching rate of 500°C/s.

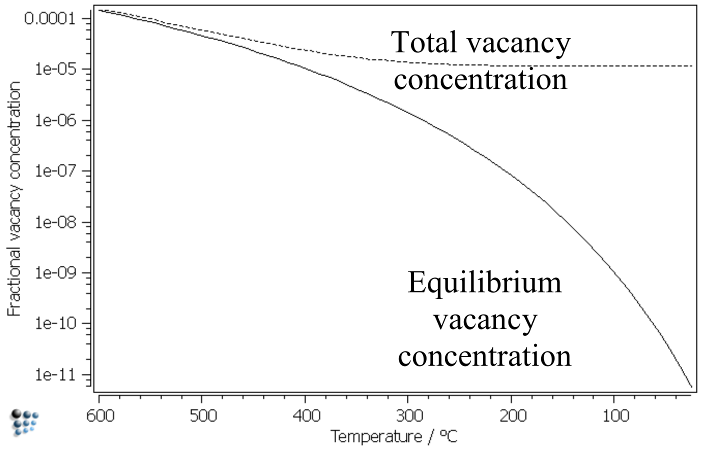

Figure 2: Evolution of the vacancy concentration in pure Al during a quench (cooling rate = 500°C/s)

When pure aluminium is quenched rapidly from close below its melting point to room temperature, a uniform distribution of vacancies is generated at a total site fraction of $1.16 \cdot 10^{-5}$. The parameters assumed for the pure Al matrix are given in Table 2.

Table 2: Precipitation domain, input parameter

| Solute [at.%] | Grain size | Dislocation density |
|---|---|---|
| Al - 100 | 100 µm | $10^{11}$ m$^{-2}$ |

The situation changes for solid solutions involving vacancy-affine impurity atoms. The equilibrium vacancy concentration at a given temperature then depends on the nature and strength of the interactions between vacancies and solute atoms or solute cluster.

The equilibrium fractional concentration of vacancies in a metal containing solute atoms is higher than that in a pure metal if the binding energy between the vacancy and the solute atom is attractive. The difference in the total vacancy concentration is dependent upon the content of the solute atoms, the temperature and the binding energy $E_b$. The values of the total vacancy evolution (free and trapped fraction) for an Al-Mg binary system with different solute contents of Mg during a cooling from 600°C to 25°C with a quenching rate of 500°C/s are plotted in Fig. 3.

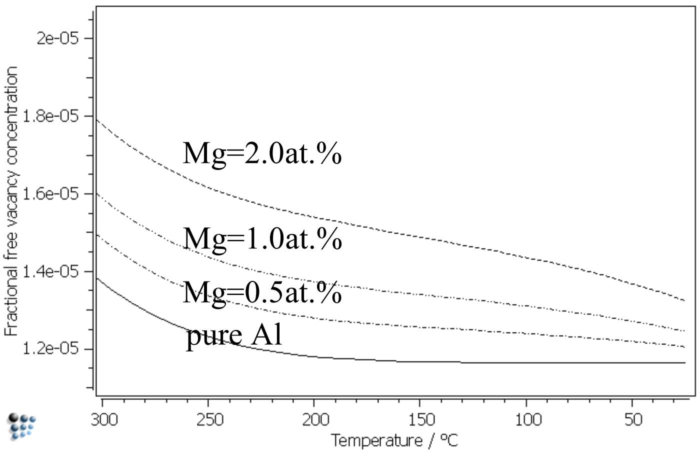

Figure 3: Simulation of the substitutional free vacancy site fraction evolution during 500 °C/s quench in an Al-xMg (x=2; 1 and 0.5at.%) alloy

For clarity, just the temperature range between 300 and 25 °C is plotted in Fig. 3. The solid line represents the pure Al system without any alloying element. When comparing the total vacancy concentration in pure Al (Fig. 2) to the free vacancy concentration in pure Al, plotted in Fig. 3, it is evident that all vacancies are free to move and, therefore, not trapped. We calculate a total = free vacancy concentration of $1.16 \cdot 10^{-5}$.

Already a content of 0.5 at.% Mg with a binding energy of 0.026eV per vacancy-solute pair increases the free vacancy fraction in the specimen after quenching from 600°C to 25°C by 4% directly after reaching room temperature. At a solid content of 2 at.% Mg, the calculated trapped fraction is approximately ¼ of the total vacancy site fraction ($1.8 \cdot 10^{-5}$), reaching a value of $4.8 \cdot 10^{-6}$ directly after the quenching process. The mean grain diameter is set to 100 μm and the dislocation density is $10^{11}$ $m^{-2}$, identical to the settings in the pure Al system.

## Vacancy Evolution during Complex Heat Treatment

Utilizing the models outline in the previous section, we perform precipitation kinetic simulations in an Al-Zn-Mg alloy with the thermo-kinetic software MatCalc [2,3,4]. The following important features, among others, are taken into account: chemical composition, temperature, size dependent interfacial energies [7,8], solid and cluster interaction with vacancies, diffusion correction based on excess vacancies and annihilation of vacancies at different types of sinks.

Exemplarily, we demonstrate the potential of our simulations on the yield strength evolution of a typical Al-5.7wt.%Zn-2.6wt.%Mg alloy class 7075 during artificial aging. In the following figures 4 - 6 the heat treatment process, the calculated vacancy evolution and the calculated phase fractions are displayed. Without taking the vacancy trapping effect into account, the excess vacancies would be annihilated immediately after the quenching.

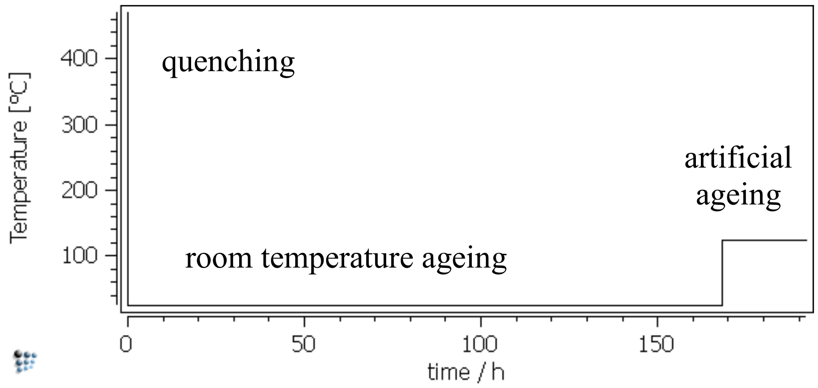

Figure 4: Temperature-time regime: quenching, natural aging (at 25°C) and artificial aging at 125°C

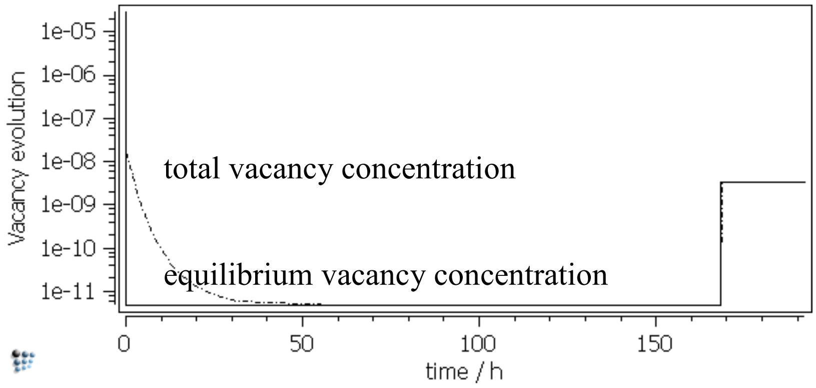

Figure 5: Vacancy concentration during quenching, natural aging and artificial aging artificial aging at 125°C

The total vacancy concentration, taking into account the vacancy trapping mechanisms, drops down to the equilibrium vacancy concentration approximately after 55 hours,. Especially within the first 24 hours after quenching the specimen, we observe a substantial increase of strength (Fig. 7), which is only plausible due to the nucleation and growth of GP-zones. This phase transformation reactions are driven by the higher mobility of the system due to the extended life-time of excess vacancies. 24 hours after quenching, the ratio of total / equilibrium vacancy concentration is still about 2.

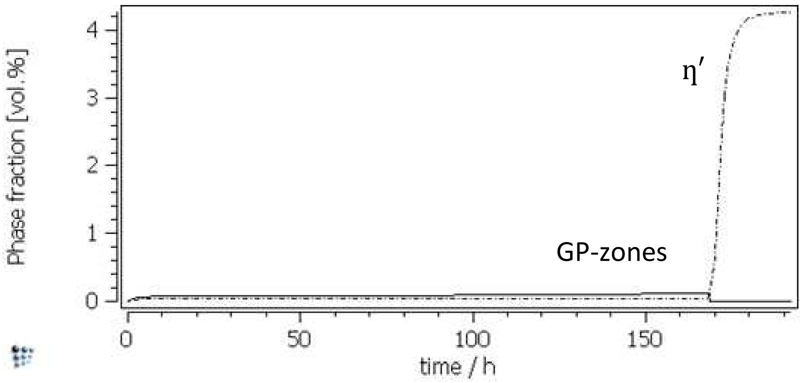

Figure 6: Evolution of phase fraction of a typical 7075 Al alloy (GP-zones and η')

As shown in Fig. 6, the main hardening phase during artificial aging is the η' phase, whereas the GP-zones get dissolved during the heating step already. This effect is reproduced clearly in Fig. 7. The triangles represent the experimentally observed yield strength measurements after applying the same heat treatment to the specimen as given in Fig. 4.

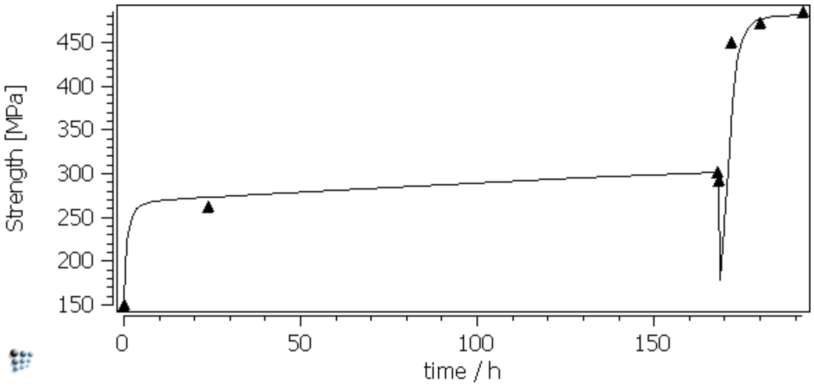

Figure 7: Evolution of yield strength of a typical 7075 Al alloy during natural aging and subsequent artificial aging at 125°C

The vacancy trapping model is essential for the initial stages of precipitation in Al-Zn-Mg alloys. Solute atoms and/or fine dispersed GP-zones trap excess vacancies and based on the trap density and the interaction energies, the life-time of excess vacancies is extended dramatically, leading to the formation of strengthening particles in the matrix due to longer and higher diffusivity.

## Conclusions

Using thermo-kinetic simulations, we discuss and emphasize the role of solute atoms in the kinetic effects attributed to vacancy trapping. In our parameter study, the total impurity content in the Al matrix is assumed to be rather small, but even at this concentration levels, significant vacancy trapping is observed depending on the strength of the vacancy-solute binding energies. The trapping effect strongly influences the concentration of lattice free vacancies, which, in turn, determines the diffusion rates of atoms in the bulk metal.

We present a model to simulate these observations also in complex realistic heat treatments. Calculated binding energies as well as physically-based descriptions of the annihilation and generation of excess vacancies are included and taken into account in the thermo-kinetic simulations. Finally, in an example, we show that all of these mechanisms, vacancy generation and annihilation as well as vacancy trapping, need to be combined to be able to simulate the precipitation kinetics and furthermore mechanical properties of Al alloys in a predictive and quantitative manner.

## References

[1] F.D. Fischer, J. Svoboda, F. Appel, E. Kozeschnik, Acta Mater. 59 (2011) 3463-3472.

[2] E. Kozeschnik, J. Svoboda, P. Fratzl, F.D. Fischer, Mater. Sci. Eng. A 385 (1-2) (2004) 157-165.

[3] J. Svoboda, F.D. Fischer, P. Fratzl, E. Kozeschnik, Mater. Sci. Eng. A 385 (1-2) (2004) 166-174.

[4] E. Kozeschnik, J. Svoboda, F.D. Fischer, Calphad 28 (2005) 379-382.

[5] P. Lang, E. Povoden-Karadeniz, W. Mayer, A. Falahati, E. Kozeschnik, Proceedings 8th Pacific Rim International Congress on Advanced Materials and Processing TMS (2013) 3181-3188.

[6] F.D. Fischer, J. Svoboda, E. Kozeschnik, Model. Simul. Mater. Sci. Eng. 21 (2013) 025008 (13p).

[7] B. Sonderegger, E. Kozeschnik, Metall Mater. Trans. 40A (2009) 499-510.

[8] B. Sonderegger, E. Kozeschnik, Scripta Materialia 60 (2009) 635-638.

Journal of Alloys and Compounds 612 (2014) 443–449

Contents lists available at ScienceDirect

Journal of Alloys and Compounds

journal homepage: www.elsevier.com/locate/jalcom

# Simulation of the effect of composition on the precipitation in 6xxx Al alloys during continuous-heating DSC

Peter Lang [a,b,*], Erwin Povoden-Karadeniz [b,c], Ahmad Falahati [b], Ernst Kozeschnik [b,c]

[a] *Department of Materials Science and Metallurgy, University of Cambridge, Charles Babbage Road 27, Cambridge CB3 0FS, UK*
[b] *Institute of Materials Science and Technology, Vienna University of Technology, Favoritenstraße 9-11, Vienna 1040, Austria*
[c] *Christian Doppler Laboratory "Early Stages of Precipitation", Institute of Materials Science and Technology, Vienna University of Technology, Favoritenstraße 9-11, Vienna 1040, Austria*

ARTICLE INFO

*Article history:*
Received 10 April 2014
Received in revised form 23 May 2014
Accepted 26 May 2014
Available online 7 June 2014

*Keywords:*
Al–Mg–Si alloys
Thermo-kinetic simulation
Thermal analysis
Linear heating

ABSTRACT

The precipitation behaviour of Al–Mg–Si alloys has been studied by differential scanning calorimetry (DSC) and by thermo-kinetic modelling. Three industrial alloys with different main solute contents, namely Mg, Si, Cu are used. Main aspect is given to the different Mg/Si ratios of the investigated alloys. Observed exothermic and endothermic peaks, accompanying the formation or dissolution of precipitates, are attributed to the formation or dissolution of individual phases, a procedure, which becomes rather involved if precipitation peaks of phases overlap. In the present paper, we propose a combination of experimental DSC analysis and computer simulation of precipitation kinetics to overcome this problem. By an iterative thermo-kinetic optimization of the simulation parameters and comparison with the heat flow evolution of the experiment, a unique picture of the complex precipitation process for different Mg/Si ratios is obtained. Exemplarily, experimental heat flow curves of various 6xxx Al alloys are unravelled and compared to the heat flow evaluated with thermo-kinetic computer simulations.

## 1. Introduction

The use of age-hardenable aluminium alloys of the 6xxx series, containing Mg and Si as major elemental additions, is hoped to lead to weight reductions of vehicles, e.g. as car body panel material. This is particularly essential due to the need to weight saving for reduction of fuel consumption and exhaust emissions. Al–Mg–Si alloys also can provide a wide range of mechanical properties for a variety of commercial applications. The ternary 6xxx Al series (Al–Mg–Si) is strengthened by precipitation of the metastable precursor precipitates $\beta''$ of the equilibrium $\beta$ ($Mg_2Si$) phase. In Al–Mg–Si–Cu alloys, dependent on the copper content, other phases such as Q′, L, S, C or QC may precipitate also and replace $\beta''$ partially as the most efficient strengthening phase [1].

Differential scanning calorimetry (DSC) is a powerful thermo-analytical technique for studying the thermodynamics and kinetics of phase changes and has been widely used to study the precipitation process in Al–Mg–Si alloys. The method is based on the difference in the amount of heat required to increase the temperature of a sample and a reference material, respectively. In the experiment, sample and reference material are heated linearly in a furnace. The sample in the test crucible can undergo phase transformations, which either release (exothermic) or consume (endothermic) energy in the form of heat (enthalpy under constant pressure). Nucleation and growth of precipitates is an exothermic reaction that releases energy (heat) from the system to the surroundings, whereas the dissolution of precipitates is endothermic and requires energy from the surrounding.

The precipitation sequence in hardenable 6xxx Al-alloys is generally accepted as [2–9].

$$\text{SSS} \rightarrow \text{clusters/co-clusters of Mg and Si} \rightarrow \text{GP zones} \rightarrow \beta''(\text{L, C}) \\ \rightarrow \beta'(\text{Q}', \text{B}', \text{U1}, \text{U2}) \rightarrow \beta(\text{Q}, \text{Si}).$$

To evaluate the sequence of precipitates and to assign the individual peaks of a DSC curve to the formation and dissolution of precipitates, in the present work, experimental DSC curves are compared to precipitation kinetics model predictions for three different 6xxx Al alloys. The impact of alloy composition, in particular the Mg:Si ratio (excess Si, near-balanced Mg/Si alloy) and the influence of Cu on the observed precipitation sequence is analysed and discussed.

---

* Corresponding author at: Department of Materials Science and Metallurgy, University of Cambridge, Charles Babbage Road 27, Cambridge CB3 0FS, UK.
*E-mail address:* pl404@cam.ac.uk (P. Lang).

http://dx.doi.org/10.1016/j.jallcom.2014.05.191
0925-8388/

## 2. Experimental

Three different wrought Al–Mg–Si alloys (designated as alloys A, B and C, with chemical compositions (listed in Table 1) are used for the DSC investigation. The aluminium alloys were provided by AMAG rolling GmbH in the form of wrought sheets.

Fe and Mn are known to bind Si in intermetallic dispersoid phases, which are assumed to be stable over the entire investigated temperature range. Therefore, the effective amount of solute Si, available for precipitation reactions, becomes reduced. The atomic ratios of Mg/Si for the three alloys, corrected for Si tied up in Fe–Mn-containing intermetallics, are summarized in Table 2. Here, we assume that the $\alpha$-$Al_{24}(Fe, Mn)_6Si_2$ phase is the predominant intermetallic dispersoid phase in a ratio 3(Fe + Mn):1Si.

The experiments are carried out in a TA Instruments 2920 modulated DSC, using a continuous heating rate under pure nitrogen flow at a rate of 50 ml/min. The samples are solution treated for 30 min at 540 °C in an air furnace and quenched into water of approx. 25 °C (RT) prior to DSC analysis. The samples are mounted in the DSC chamber immediately after quenching (within one minute natural aging at RT). Differential scanning calorimetry scans are made over the temperature range from 25 to 550 °C. Annealed Al of technical purity (99.98%) and of comparable shape and weight to the sample is used as a reference to ensure a flat baseline. A rerun is used as a baseline correction. Test runs for alloy A under argon atmosphere and a solution heat treatment for 60 min at 540 °C are carried out in addition to the experiments shown in this manuscript to ensure that (i) the DSC tests are inert to the nitrogen gas and that (ii) the solution treatment for 30 min is sufficiently long to dissolve the secondary Mg–Si–Cu particles. Heating rates of 5 °C/min for alloys A and C and 10 °C/min for alloy B are conducted to show the effect of the heating rate on the peak temperatures and to validate the ability of the model for different heating rates. With increasing heating rate, the reaction temperatures are displaced to higher temperatures. For comparison, the heat flow evolution of Alloy B is calculated for 5 and for 10 °C/min and discussed briefly.

## 3. Thermo-kinetic computation

All calculations presented in this work are performed using the software package MatCalc [10–15].

MatCalc [10–15] is a thermo-kinetic software package developed for the simulation of the precipitation kinetics of various metallurgical phases. The characteristics of this program can be summarized as a mean-field treatment of nucleation, growth and coarsening of multi-component, multi-phase and multi particle systems. This approach is based on the Onsager thermodynamic extremal principle [16], assuming that a thermodynamic system evolves along the particular kinetic path, where maximum entropy is produced.

The theory is described by Svoboda et al. [10] and the treatment of the numerical implementation in the software package MatCalc was done by Kozeschnik et al. [11]. The basis for the calculation of the thermodynamics of the system are CALPHAD type databases, providing chemical potentials of the phases as well as diffusivities of the involved elements on the basis of the chemical composition of the alloy and the present temperature.

The metastable precipitates that are considered in the simulations are disordered Mg–Si co-clusters [17], coherent, ordered Al-containing GP zones [18], semi-coherent needle-like $\beta''$ ($Mg_5Si_6$) and the metastable, semi-coherent later phase included in the simulation is $\beta'$ [19]. Recently, Li et al. [20] showed that Cu can partially substitute Mg in the atomic structure of $\beta''$ in Cu-containing Al–Mg–Si alloys. To take the Cu solubility in $\beta''$ into account, we have adopted our thermodynamic description. Li et al. determined the Cu content in the $\beta''$ structure with approximately 5 at.% using atom probe tomography [20]. Our model, presently, predicts the highest Cu content to be about 2 at.% for the given chemical composition in alloy C. The stable phases considered are $\beta$, Q, Si. The models implemented in MatCalc [10–15] contain a number of input parameters, which are obtained from experimental observation, such as dislocation density, grain size and the Young's modulus of the matrix. The degree of interface coherency, the shape of the different particles, the volumetric misfit and nucleation site preferences used in the simulations are listed in Table 2 and represent the key input data for the simulation.

**Table 1**
Nominal composition in wt.% and calculated at.% of investigated alloys.

| Alloy | Mg | | Si | | Cu | | Fe | | Mn | |
|---|---|---|---|---|---|---|---|---|---|---|
| | wt.% | at.% | wt.% | at.% | wt.% | at.% | wt.% | at.% | wt.% | at.% |
| Alloy A | 0.35 | 0.39 | 1.06 | 1.02 | 0.07 | 0.03 | 0.16 | 0.07 | 0.07 | 0.03 |
| Alloy B | 0.78 | 0.87 | 1.06 | 1.02 | 0.04 | 0.02 | 0.21 | 0.10 | 0.74 | 0.36 |
| Alloy C | 0.90 | 1.00 | 0.65 | 0.63 | 0.22 | 0.09 | 0.18 | 0.08 | 0.78 | 0.38 |

**Table 2**
Effective main solute content (at.%) and effective Mg/Si ratio.

| Alloy | Effective Si (at.%) | Effective Mg/Si ratio |
|---|---|---|
| Alloy A | 0.99 | 0.39 |
| Alloy B | 0.87 | 1.00 |
| Alloy C | 0.50 | 2.00 |

The choice of the nucleation site is an important input parameter as it represents the probability for nucleation (e.g. nucleation site: bulk, each single atom in the structure represents a potential nucleation site). The aspect ratio describes the morphology of the precipitates and thus the solute diffusion field geometry during growth for non-spherical particles.

Using results from atom probe tomography experiments [22] and high-resolution electron microscopy, spherical shape is assumed for the co-clusters. GP zones are assumed to form platelets [23]. The very early phases are fully coherent with the matrix and are expected to have fcc structure. The needle-shaped $\beta''$ phase has a different structure (monoclinic unit cell) from the surrounding matrix (fcc) and appears to be semi-coherent from the start [24]. The rod shaped $\beta'$ precipitates are semi-coherent and characterized by a hexagonal structure [25]. The $\beta$ phase is the equilibrium phase in this system. It is a $CaF_2$ type fcc structure with the stoichiometry $Mg_2Si$ [24]. The morphology of the $Mg_2Si$ phase is found to appear in platelet [26], cuboid [27] and rod-like [28] variants. For computational simplification, the aspect ratio for the $Mg_2Si$ particles is assumed to be unity (sphere) in the simulation set-up. The U1 phase is trigonal and has composition $MgAl_2Si_2$, the U2 phase is orthorhombic (AlMgSi) and related to the $\beta''$ and $\beta'$ phase [8,9].

The physical properties of the matrix used in the simulations are summarized in Table 3. The dislocation density and the mean grain diameter are realistic assumptions (in the range mentioned in Ref. [31]), but have not been investigated in detail.

All calculations are performed with the same input parameter as listed in Tables 3 and 4.

## 4. Results

### 4.1. Alloy A

The experimentally observed DSC curve in Fig. 1 exhibits five exothermic peaks and four endothermic peaks. These are related

**Table 3**
Summary of input data for precipitation kinetics simulation.

| Phase | Co-clusters | GP zones | $\beta''$ | $\beta'$ | Q′ and Q | $\beta$ | Si |
|---|---|---|---|---|---|---|---|
| Interface[a] | C | C | SC | SC | SC and IC | IC | IC |
| Volume misfit (%)[b] | 0.1 | 1 | 5 | 10 | 0 | 0 | 0 |
| Nucleation sites[c] | B | B | B | D | D | G | G |
| Shape factor[d] | 1 | 0.1 | 10 | 5 | 0.5 | 1 | 0.5 |

[a] C ... coherent, SC ... semi-coherent, IC ... incoherent.

[b] Volumetric misfit only relevant for coherent/semicoherent phases (values chosen are close to ab initio calculations by van Huis et al [21]).

[c] B ... bulk, D ... dislocations, G ... grain boundaries.

[d] Aspect ratio: 0.1 ... plate, 0.5 ... lath, 1 ... sphere, 10 ... needle (note: 10 – growth is reduced, only the face side of a needle is expected to adsorb solute atoms to make the needle grow, 0.1 – growth is accelerated, face side is comparable large to the shape of a disc).

to the formation and dissolution of the various precipitates in alloy A. Figs. 2 and 3 summarize the main results of the corresponding MatCalc simulations in the form of the precipitate phase fraction evolution as well as the evolution of the matrix chemical composition.

In an analysis of structural vacancies based on the recently developed FSAK (Fischer–Svoboda–Appel–Kozeschnik) model [15], first, we find that the amount of excess vacancies, which is quenched-in at room temperature prior to heating inside the DSC chamber, adopts a total mole fraction of $5 \cdot 10^{-6}$ directly after quenching. This huge amount of non-equilibrium vacancies facilitates the precipitation of coherent early phases by accelerating solute diffusion to a remarkable extent even at room temperature, thus supporting the formation of Mg–Si co-clusters in the beginning of the precipitation reactions (peak I, Fig. 1). The cluster volume fraction reaches a maximum of 0.04 vol.% (Fig. 2), having a Mg:Si ratio of 1, which is consistent with literature [29]. On further heating, however, these clusters become thermodynamically unstable and start to dissolve (endothermic reaction).

The large (−15 mW/g) exothermic peak II (see Fig. 3) at ~230 °C is associated with the formation of the β″ phase. With a high number density ($>10^{22}/m^3$) and precipitate sizes of maximum 20 nm in length (needle-like shape), a volume fraction of almost 0.4% is achieved. The formation of β″ is followed by the precipitation of β′ (peak III) at approximately 300 °C. From the composition evolution in Fig. 4, we observe a pronounced reduction of Si within the matrix at approximately 400 °C. When comparing this with the experimental DSC signal in Fig. 1, we find a good correlation of the evolution of Si content in the matrix with the exothermic peak IV and the endothermic peak VI. From the calculated phase fraction evolution in Fig. 2, we furthermore observe that these two peaks coincide well with the precipitation and dissolution temperatures of the Si-rich phases (pure Si precipitates or also the U1-$MgAl_2Si_2$ or U2-MgAlSi phase). Obviously, the two peaks IV and VI are mainly caused by these precipitates, which, on formation, temporarily deplete the matrix from Si atoms. Precipitation of Si-rich particles is expected, since the alloy is characterized by excess Si. Stable β ($Mg_2Si$) and/or U1-MgAlSi precipitates, where Mg is partially replaced by Al, are responsible for peak V at approximately 400–420 °C. At around 460 °C, the simultaneous dissolution of the stable Mg–Si and Si-rich precipitates lead to the occurrence of the endothermic peak VI.

### 4.2. Alloy B

The simulation result for the alloy B is shown in Fig. 4 together with the experimentally observed DSC curve. The higher absolute values of the measured and simulated heat flow of alloy B in comparison to alloys A and C are due to the higher heating rate (10 °C/min for alloy B, 5 °C/min for alloys A and C) and the higher content of alloying elements. The latter is also reflected in the higher volume fractions of precipitate phases.

Exemplarily, we show the calculated DSC thermograms for alloy B for two different heating rates in Fig. 5. The peak temperature for the exothermic reactions, i.e. peaks II and IV, are displaced to higher temperatures for the higher heating rate. The shift is approximately 15 °C when the heating rate is changed from 5 to 10 °C/min.

**Table 4**
Summary of input data for precipitation domain (Al-matrix).

| Parameter | Value/unit |
|---|---|
| Dislocation density | $10^{11} \cdot m^{-2}$ |
| Grain diameter | 50 μm |

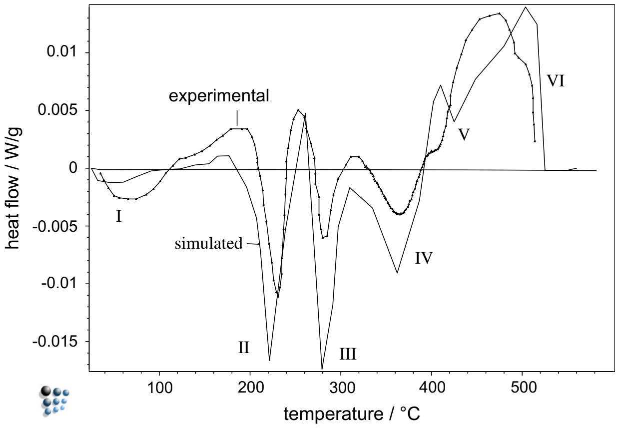

**Fig. 1.** DSC model prediction of the heat flow compared with experimental scan for alloy A.

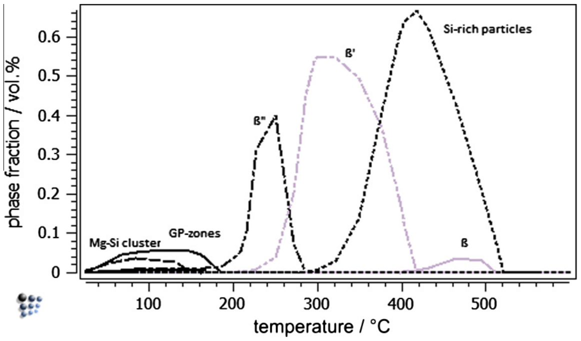

**Fig. 2.** Simulated molar phase fraction evolution for alloy A over temperature during DSC run.

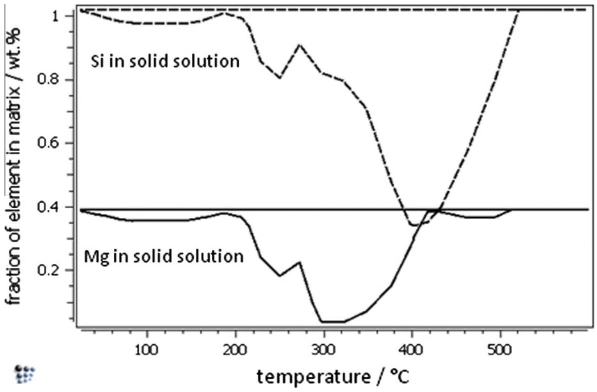

**Fig. 3.** Simulated evolution of the chemical composition of the matrix for alloy A over temperature during DSC run.

Alloy B does not contain as much excess silicon such as alloy A, but also a higher total solute content. As a consequence, larger precipitate sizes and higher volume fractions are observed for alloy B. The influence of the different solute content is reflected in the different phase fractions of the phases in alloys A (Fig. 2) and B (Fig. 6). Alloy A shows half the phase fraction of the very early phases compared to alloy B. The higher solute content of alloy B leads to coarser β″ precipitates in our simulations. Alloy B exhibits a phase fraction of β″ of almost 1 vol.%.

On basis of the simulated evolution of phase fractions shown in Fig. 6, a correlation of DSC peaks with precipitation and dissolution of second phases is attempted. The exothermic peak IV (Fig. 4) at

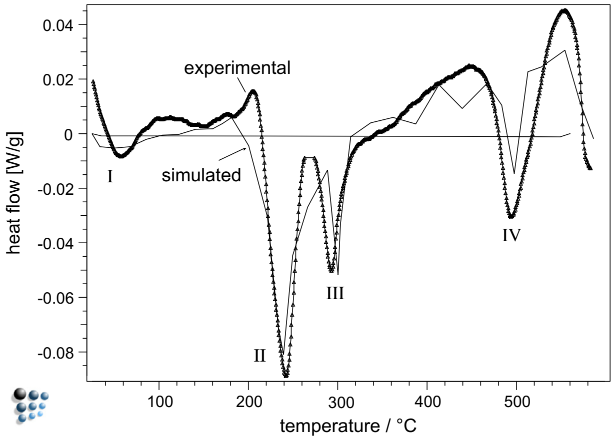

**Fig. 4.** DSC model prediction of the heat flow compared with experimental data for alloy B.

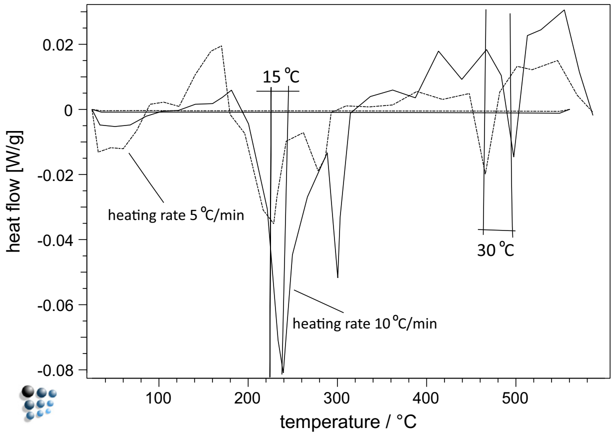

**Fig. 5.** DSC heat flow evolution calculated for 5 and 10 °C/min for alloy B.

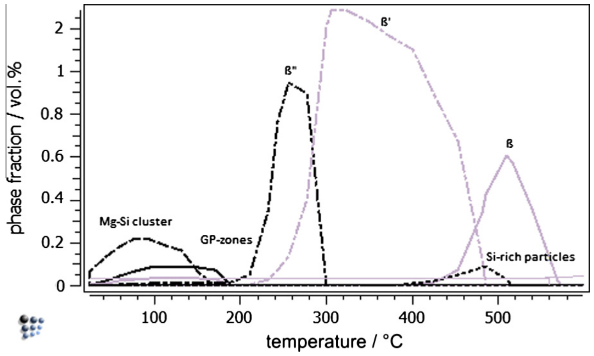

**Fig. 6.** Simulated phase fraction evolution in alloy B during DSC analysis.

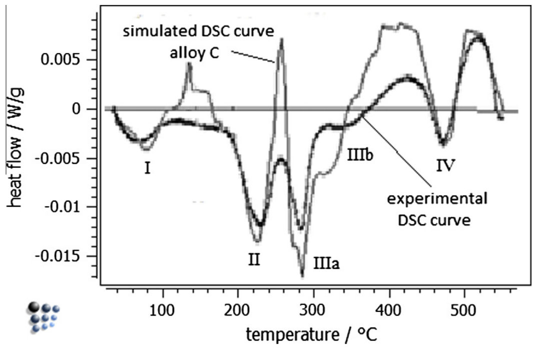

**Fig. 7.** DSC simulation of the heat flow compared with the experimental signal for alloy C.

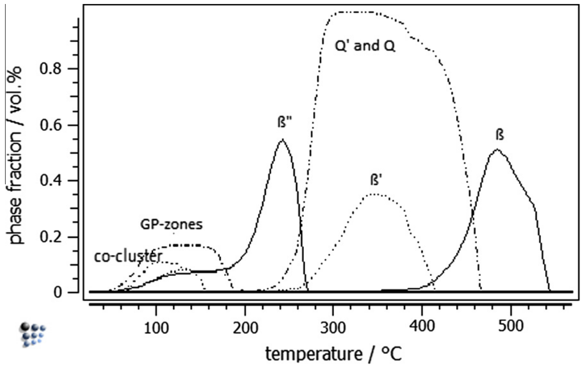

**Fig. 8.** Calculated phase fraction evolution for alloy C during DSC simulation.

approximately 490 °C is related to the formation of the stable β phase ($Mg_2Si$). The formation temperature of β during DSC continuous heating is in good agreement with literature [30]. The exothermic reaction is occurring at higher temperature compared to alloy A, which might indicate that the peak V (Fig. 1) is mainly associated with the U1 phase coexisting to the $Mg_2Si$ phase. The predominance of the stable $Mg_2Si$ over the pure Si phase is a consequence of the higher Mg:Si ratio. This is the most significant difference between alloys A and alloy B at high temperatures.

### 4.3. Alloy C

Alloy C is distinguished from the previous two alloys by a considerable higher amount of Cu. If copper is added in sufficient amount for the Cu-containing quaternary alloys the equilibrium phase Q and its precursor phase Q′, L, S, C, QC are reported [1,2,31,32,37] during artificial aging.

Figs. 7 and 8 show the evolution of the DSC signal and the phase fractions for alloy C. We observe good agreement between experiment and simulation for precipitation stages in terms of the formation and dissolution temperatures. This indicates that the thermodynamic description of Cu-containing metastable phases with Mg–Cu substitution represents the observed thermo-kinetic reactions reasonably well. Different types of Cu-containing Q precursors are reported in Refs. [2,33,34]. Accordingly, the L phase is different form Q′ and represents a precursor to Q′. With increasing Cu content, the relative proportion of L to β″ increases at peak-aged conditions [35]. The L phase was observed to be disordered, whereas the C phase was found to be ordered within a monoclinic unit cell. However, because of the uncertainty of exact structures, compositions and missing sublattice models applicable to Cu containing precursor phases, we have to neglect these precursor phases in our present modelling, where Cu containing β“ is the only phase contributing to the peak at 225 °C. We also consider this deficiency as the reason for the only fair quantitative agreement in the integral heat flow of the individual peaks. Quantitative correlation would require an entire reassessment of the early phases in this system, which is certainly beyond the scope of this work.

Due to the substitution of Mg with Cu in the early phases, Cu can be tied up by the metastable phases, in our simulation. The later precipitate phase including Cu in our simulation is the Q phase. Since the metastable Q′ and the stable Q phases are described by the same stoichiometry [32], we do not distinguish between Q′ phase and main Q phase in our simulation, but treat them together as just one kind of precipitate (Q′ and Q). The experimental as well as simulated exothermic peak III in Fig. 7 is more prominent than that in alloy A. The reaction is characterized by the co-existence of Q′ (IIIa) and β′ (IIIb). The Q′ phase is coherent with the Al matrix along the needle direction and is mainly found in the overaged stage [32]. This is reflected also in Fig. 8, which shows the pronounced presence of Cu-containing Q′ and Q. The last stable phase in the sequence is β, reflected in the exothermic peak IV in Fig. 8.

## 5. Discussion

The DSC curves of all three alloys are similar to each other. The main phase transformation reactions occur under similar temperatures. Unique for all Al–Mg–Si(–Cu) heat-treatable alloys is the significant increase in hardness upon ageing. The increase is caused by a large number of tiny metastable precipitates that form after quenching from the solid solution. It is generally believed that excess Si (wt.% Mg < 1.732 wt.% Si) in the composition of Al–Mg–Si alloys affects the formation kinetics, characteristics and thermodynamics of clusters and other early precipitates but does not alter the precipitation sequence, structure or lattice parameters of metastable precursors [36].

The presence of excess Si changes the density of metastable β” particles, as validated by the thermo-kinetic simulations, which is consistent with the literature [37]. As shown in Fig. 9 the number density of the main hardening phase β″ in alloy A (high amount of excess Si) is double as high as for alloy B.

The alloy A has denser precipitate structure during continuous heating compared to alloy B, resulting in finer and denser structure of β″ precipitates as shown in Figs. 9 and 10. Fig. 10 shows the calculated mean radii of β″. For clarity, the extension of the needle is represented by the mean radius of an equivolumetric sphere.

From literature, the experimentally observed shape of the various different precipitates is well known [25,22–31,24,38]. Accordingly, in our simulations, we use an aspect ratio model for non-spherical morphologies [39], which is able to predict the evolution of radius and length of the precipitates in a more accurate way than a simple model based on spherical morphology. For the β″ phase, which is the most important phase for precipitation strengthening in the ternary Al–Mg–Si alloys, TEM [24,33] indicates that these precipitates adopt needle-like form. With an aspect ratio of 10 in our simulation, the models give realistic predictions of mean diameter and mean length, see Fig. 11. The simulated sizes are in good agreement with typical values of this kind of precipitate having approximately 10–16 nm in length and 2 nm in diameter [33,38].

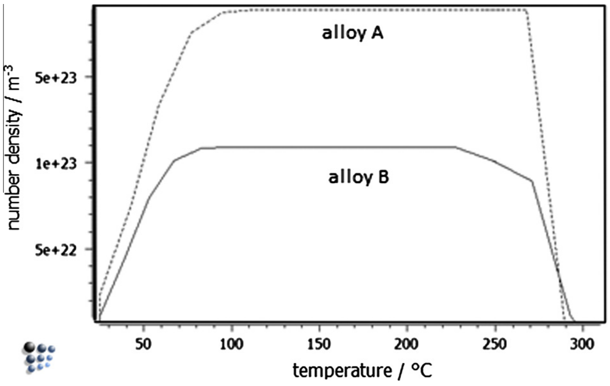

**Fig. 9.** Calculated number densities of β″ for alloy A and alloy B during continuous heating.

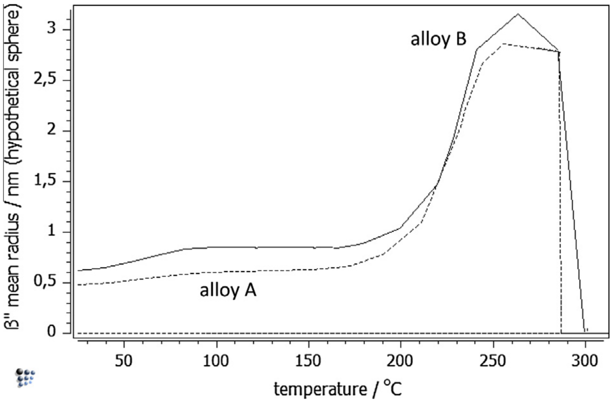

**Fig. 10.** Calculated equivolumetric sphere mean radii for β″ for alloy A and alloy B during continuous heating.

Cu additions to the Al–Mg–Si system affect the precipitation sequence as mentioned in Section 4.3. Further investigations regarding Cu containing metastable phases are necessary to improve the thermodynamic and thermo-kinetic modelling. Marioara et al. [33] found three – so-called – Q′ precursors, namely L, S and C, all with typically lath shape. The equilibrium phase in Cu added Al–Mg–Si alloys are the Q and the β phases [32]. β“ still appears, but other precipitate phases are also present at peak hardness. For the quaternary Al–Mg–Si–Cu system, the precipitation sequence is reported to be [33]

$$\text{SSS} \rightarrow \text{atomic clusters} \rightarrow \text{GP zones} \rightarrow \beta'', \text{L}, \text{S}, \text{C}, \text{QC}, \text{QP} \rightarrow \beta', \text{Q}' \rightarrow \text{Q}, \beta.$$

The large number of precursor phases renders the precipitation sequence rather complex and more overlapping reactions are reported to occur relative to the Cu-free alloys.

For the time being Cu, containing early phases (GP zones and intermediate β″ phases) are described and calculated by the facilitated substitution of Mg with Cu. Marioara et al. [33] found that up to 70–80% of the precipitates at peak hardness are Cu containing precipitates. This leads to the conclusion that, especially the overaged condition, is very well reproduced with our simulations, taking the most prominent phases into account. Accordingly, the Q′

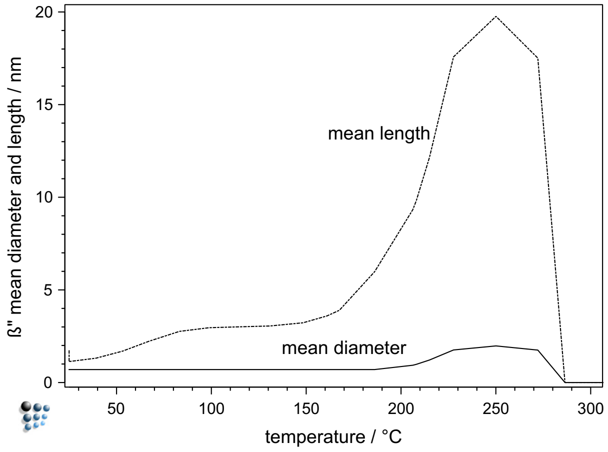

**Fig. 11.** Mean diameter and mean length of β″ during continuous heating in the DSC (alloy B).

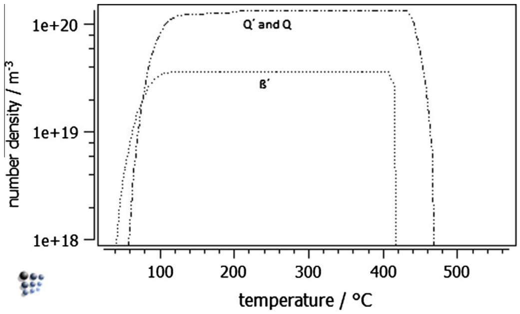

**Fig. 12.** Calculated number densities of β′ and Q′ for alloy C during continuous heating.

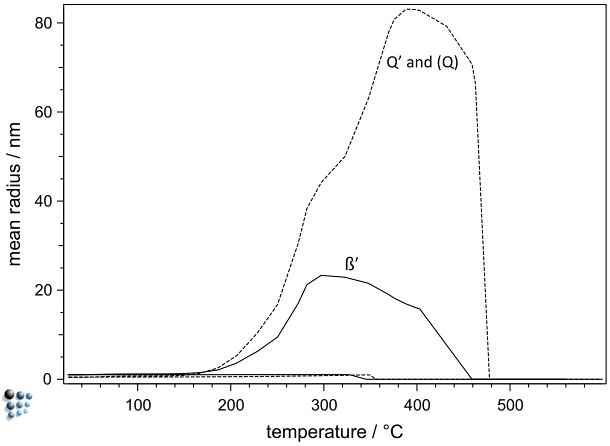

**Fig. 13.** Calculated mean radii of β′ and Q′ (Q) for alloy C during continuous heating.

precipitates account for about 80% of the total number of β‘ and Q precipitates as shown in Fig. 12, which is in good agreement with experimental findings.

The Q’ phase appears in peak age condition and/or during over-aging [32]. Unlike a transition, which involves a change in crystal structure, the Q′ phase maintains in same crystal structure and morphology as Q through the overaged conditions. Only its size increases [32]. Same behaviour is observed in our simulation of the alloy C (Cu containing system). The evolution of the mean radii of the β′ and the Q′ (Q phase) are given in Fig. 13.

## 6. Conclusion

The aging process in as-quenched Al–Mg–Si alloys proceeds with the formation of clusters and GP-zones, followed by sequential precipitation of β″ and other metastable phases until the precipitation of the equilibrium phases occur. Experimental DSC thermograms are rather complicated due to the appearance of overlapping reactions caused by simultaneous precipitation of different phases. Thermo-kinetic modelling is a powerful tool to establish the complex precipitation kinetics during different stages of aging. Even the initial stages of precipitation, characterized by the clustering reactions can be identified and described by the usage of suitable computer simulations. The models obtain access to otherwise hidden details of the complex precipitation sequences of the Al–Mg–Si(–Cu). The simulated DSC curves of the three alloys are in good agreement with the experimental curves, both, qualitatively as well as quantitatively, with the peaks and troughs related to individual phase formation and dissolution being of similar amplitude over the entire temperature range.

## Acknowledgement

P.L would like to express sincere thanks to T. Weisz and St. Zellhofer for their help in DSC experiments.

## References

[1] C.D. Marioara, S.J. Andersen, J. Røyset, O. Reiso, S. Gulbrandsen-Dahl, T.-E. Nicolaisen, I.-E. Opheim, J.F. Helgaker, R. Holmestad, Improving thermal stability in Cu-containing Al–Mg–Si alloys by precipitate optimization, Met. Mater. Trans. 45A (2014) 2938–2949.
[2] X. Wang, S. Esmaili, D.J. Lloyd, The sequence of precipitation in the Al–Mg–Si–Cu alloy AA6111, Met. Mater. Trans. 37A (2006) 2691–2699.
[3] A. Gaber, N. Afify, M.S. Mostafa, Gh. Abbady, Effect of heat treatment on the precipitation in Al–1 at.% Mg–$x$ at.% Si ($x$ = 0.6, 1.0 and 1.6) alloys, J. Alloys Comp. 477 (1–2) (2009) 295–300.
[4] A. Gaber, M.A. Gaffar, M.S. Mostafa, E.F. Abo Zeid, Precipitation kinetics of Al–1.12 $Mg_2Si$–0.35 Si and Al–1.07 $Mg_2Si$–0.33 Cu alloys, J. Alloys Comp. 429 (2007) 167–175.
[5] C. Cayron, P.A. Buffat, Transmission electron microscopy study of the β′ phase (Al–Mg–Si alloys) and QC phase (Al–Cu–Mg–Si alloys): ordering mechanism and crystallographic structure, Acta Mater. 48 (2000) 2639–2653.
[6] C.D. Marioara, S.J. Andersen, J. Jansen, H.W. Zandbergen, The influence of temperature and storage time at RT on nucleation of the β″ phase in a 6082 Al–Mg–Si alloy, Acta Mater. 51 (2003) 789–796.
[7] G.C. Weatherly, A. Perovic, N.K. Mukhopadhyay, D.J. LLoyd, D.D. Perovic, The precipitation of the Q phase in an AA6111 alloy, Met. Mater. Trans. 32A (2001) 213–218.
[8] S.J. Andersen, C.D. Marioara, A. FrØseth, R. Vissers, H.W. Zandbergen, Crystal structure of the orthorhombic U2-$Al_4Mg_4Si_4$ precipitate in the Al–Mg–Si alloy system and its relation to the β′ and β“ phases, Mater. Sci. Eng. A 390 (2005) 127–138.
[9] S.J. Andersen, C.D. Marioara, R. Vissers, A. FrØseth, H.W. Zandbergen, The structural relation between precipitates in Al–Mg–Si alloys, the Al-matrix and diamond silicon, with emphasis on the trigonal phase U1-$MgAl_2Si_2$, Mater. Sci. Eng. A 444 (2007) 157–169.
[10] J. Svoboda, F.D. Fischer, P. Fratzl, E. Kozeschnik, Modelling of kinetics in multi-component multi-phase systems with spherical precipitates: I: theory, Mater. Sci. Eng. A 385 (1–2) (2004) 166–174.
[11] E. Kozeschnik, J. Svoboda, P. Fratzl, F.D. Fischer, Modelling of kinetics in multi-component multi-phase systems with spherical precipitates: II: numerical solution and application, Mater Sci. Eng. A 385 (1–2) (2004) 157–165.
[12] E. Kozeschnik, J. Svoboda, F.D. Fischer, Modified evolution equations for the precipitation kinetics of complex phases in multi-component systems, Calphad 28 (4) (2004) 379–382.
[13] B. Sonderegger, E. Kozeschnik, Generalized nearest-neighbor broken-bond analysis of randomly oriented coherent interfaces in multicomponent fcc and bcc structures, Met. Mater. Trans. 40A (2009) 499–510.
[14] B. Sonderegger, E. Kozeschnik, Size dependence of the interfacial energy in the generalized nearest-neighbor broken-bond approach, Scr. Mater. 60 (2009) 635–638.
[15] F.D. Fischer, J. Svoboda, F. Appel, E. Kozeschnik, Modeling of excess vacancy annihilation at different types of sinks, Acta Mater. 59 (2011) 3463–3472.
[16] L. Onsager, Reciprocal relations in irreversible processes I, Phys. Rev. 37 (1931) 405–427.
[17] J. Banhart, C.S.T. Chang, Z. Liang, N. Wanderka, M.D.H. Lay, J. Hill, Natural aging in Al–Mg–Si alloys – a process of unexpected complexity, Adv. Eng. Mater. 12 (7) (2010) 559–571.
[18] C.D. Marioara, S.J. Andersen, J. Jansen, H.W. Zandbergen, Atomic model for GP-zones in a 6082 Al–Mg–Si system, Acta Mater. 49 (2001) 321–328.
[19] E. Povoden-Karadeniz, P. Lang, P. Warczok, A. Falahati, E. Kozeschnik, CALPHAD modeling of metastable phases in the Al–Mg–Si system, Calphad 43 (2013) 94–104.
[20] K. Li, A. Beche, M. Song, G. Sha, X. Lu, K. Zhang, Y. Du, S.P. Ringer, D. Schryvers, Scr. Mater. 75 (2014) 86–89.
[21] M.A. van Huis, J.H. Chen, M.H.F. Sluiter, H.W. Zandbergen, Phase stability and structural features of matrix-embedded hardening precipitates in Al–Mg–Si alloys in the early stages of evolution, Acta. Mater 55 (2007) 2183–2199.
[22] A. Serizawa, S. Hirosawa, T. Sato, Three-dimensional atom probe characterization of nanoclusters responsible for multistep aging behavior of an Al–Mg–Si alloy, Met. Mater. Trans. A 39 (2008) 243–251.
[23] K. Matsuda, H. Gamada, K. Fujii, Y. Uetani, T. Sato, A. Kamio, S. Ikeno, High-resolution electron microscopy on the structure of Guinier–Preston zones in an Al-1.6 mass pct $Mg_2Si$ alloy, Met. Mater. Trans. A 29 (1998) 1161–1167.
[24] S.J. Andersen, H.W. Zandbergen, J. Jansen, C. Traeholt, U. Tundal, O. Reiso, The crystal structure of the β″ phase in Al–Mg–Si alloys, Acta Mater. 46 (1998). pp. 3283–2398.
[25] J.Y. Yao, D.A. Graham, B. Rinderer, M.J. Couper, A TEM study of precipitation in Al–Mg–Si alloys, Micron 32 (2001) 865–870.

[26] M.H. Jacobs, The structure of the metastable precipitates formed during ageing of an Al–Mg–Si alloy, Philos. Mag. 26 (1972) 1–13.

[27] Y. Ohmori, L.C. Doan, K. Nakai, Ageing processes in Al–Mg–Si alloys during continuous heating, Mater. Trans. 43 (2) (2002) 246–255.

[28] C. Phongphisutthian, H. Tezuka, E. Kobayashi, T. Sato, Effects of β-$Mg_2Si$ precipitates on semi-solid microstructures of wrought Al–Mg–Si alloys produced by deformation-semi-solid-forming process, Mater. Trans. 54 (4) (2013) 609–617.

[29] M.J. Starink, L.F. Cao, P.A. Rometsch, A model for the thermodynamics of and strengthening due to co-clusters in Al–Mg–Si-based alloys, Acta Mater. 60 (2012) 4194–4207.

[30] Y. Birol, The effect of sample preparation on the DSC analysis of 6061 alloy, J. Mater. Sci. 40 (2005) 6357–6361.

[31] K. Matsuda, S. Taniguchi, K. Kido, Y. Uetani, S. Ikeno, Effects of Cu and transition metals on the precipitation behaviors of metastable phases at 523 K in Al–Mg–Si alloys, Mater. Trans. 43 (11) (2002) 2789–2795.

[32] D.J. Chakrabarti, D.E. Laughlin, Phase relations and precipitations in Al–Mg–Si alloys with Cu additions, Prog. Mater. Sci. 49 (2004) 389–410.

[33] C.D. Marioara, S.J. Andersen, T.N. Stene, H. Hasting, J. Walmsley, A.T.J. vanHelvoort, R. Holmestad, The effect of Cu on precipitation in Al–Mg–Si alloys, Philos. Mag. 87 (2007) 3385–3413.

[34] H.S. Hasting, A.T.J. van Helvoort, J.C. Wamsley, C.D. Marioara, S.J. Andersen, R. Holmestad, Z-contrast of precipitation phases in AlMgSiCu alloys, proc. International Microscopy Congress IMC16 (2006) 1593.

[35] D.J. Chakrabarti, Y. Peng, D.E. Laughlin, Precipitation in Al–Mg–Si alloys with Cu additions and the role of the Q′ and related phases, Mater. Sci. Forum 396–402 (2002) 857–862.

[36] M. Murayama, K. Hono, W.F. Miao, D.E. Laughlin, The effect of Cu additions on the precipitation kinetics in an Al–Mg–Si alloy with excess Si, Met. Mater. Trans. A 32 (2001) 239–246.

[37] A.K. Gupta, D.J. Lloyd, S.A. Court, Precipitation hardening in Al–Mg–Si alloys with and without excess Si, Mater. Sci. Eng. A 316 (1–2) (2001) 11–17.

[38] G.A. Edwards, K. Stiller, G.L. Dunlop, M.J. Couper, The precipitation sequence in Al–Mg–Si alloys, Acta Mater. 46 (1998) 3893–3904.

[39] E. Kozeschnik, J. Svoboda, F.D. Fischer, Shape factors in modeling of precipitation, Mater. Sci. Eng. A 441 (2006) 68–72.

Journal of Alloys and Compounds 609 (2014) 129–136

Contents lists available at ScienceDirect

Journal of Alloys and Compounds

journal homepage: www.elsevier.com/locate/jalcom

# Thermo-kinetic prediction of metastable and stable phase precipitation in Al–Zn–Mg series aluminium alloys during non-isothermal DSC analysis

Peter Lang [a,*], Tomasz Wojcik [b], Erwin Povoden-Karadeniz [b,c], Ahmad Falahati [b], Ernst Kozeschnik [b,c]

[a] Department of Materials Science and Metallurgy, University of Cambridge, Charles Babbage Road 27, Cambridge CB3 0FS, UK
[b] Institute of Materials Science and Technology, Vienna University of Technology, Favoritenstraße 9-11, Vienna 1040, Austria
[c] Christian Doppler Laboratory "Early Stages of Precipitation", Institute of Materials Science and Technology, Vienna University of Technology, Favoritenstraße 9-11, Vienna 1040, Austria

ARTICLE INFO

*Article history:*
Received 1 March 2014
Received in revised form 17 April 2014
Accepted 18 April 2014
Available online 30 April 2014

*Keywords:*
Al–Zn–Mg alloys
Precipitation sequence
DSC analysis
Thermo-kinetic simulation

ABSTRACT

The technological properties of heat treatable Al–Zn–Mg alloys originate in the morphology and distribution of metastable particles. Starting from the solution-annealed condition, this paper describes the precipitate evolution during non-isothermal temperature changes, namely continuous heating differential scanning calorimetry (DSC) analysis. The distribution and the morphology of the metastable and stable precipitates and the heat flow accompanying the precipitation process is investigated experimentally and calculated by numerical thermo-kinetic simulations. The computer simulation results of the sizes and distributions are confirmed by transmission electron microscopy (TEM). The theoretical background and the results of the investigations are discussed.

## 1. Introduction

Al–Zn–Mg alloys are widely used in aerospace and automotive industry. The 7xxx series Al alloys are precipitation-hardening alloys with the main alloying elements Zn and Mg, as well as additions of Cu. Especially, this series of Al alloys with high mechanical strength are attractive as structural materials to reduce weight. Different investigation techniques, such as high-resolution microscopy and diffraction or differential scanning calorimetry are available to identify and define metastable or stable precipitate particles during different time–temperature regimes. However, there is clearly a need to design physical modelling approaches to describe the whole range of a precipitation sequence in Al alloys. In general, processing and testing of different kinds of alloys involves many operations and are time- and cost consuming. Thermo-kinetic simulation offers new possibilities in the alloy and process development. In the present work, a computational tool for simulation of phase transformations is utilized to calculate precipitation kinetics in Al–Zn–Mg alloys. The approach has already been successfully employed for kinetics simulation in other types of Al alloys [1]. In this work, particular focus is laid on the formation of metastable and stable phases in the Al–Zn–Mg system.

Differential scanning calorimetry (DSC) is utilized to study the precipitation sequence in pure Al–Zn–Mg and in industrial 7075 Al alloys. Differential scanning calorimetry (DSC) is a powerful thermo-analytical technique for studying the thermodynamics and kinetics of phase changes. The method is based on the difference in the amount of heat required to increase the temperature of a sample (S) and a reference material (R), respectively. In the experiment, sample and reference material are heated linearly in a furnace. The sample in the test crucible can undergo phase transformations, which either release (exothermic) or consume (endothermic) energy in the form of heat (enthalpy under constant pressure). This heat is directly compared to the enthalpy evolution of the reference specimen, which is known from independent prior experiment. In the continuous-heating DSC experiment, either the heat flux between two thermally connected reference and test samples is measured, or, by excess cooling or heating, the energy, which is necessary to compensate for the temperature change in the reference pan.

In continuous heating DSC of quenched Al-alloys, solid-state precipitation is causing peaks in the heat flux curve as a function of temperature. The area under the peak, with respect to the base line measured in the reference sample (R), is proportional to the enthalpy change accompanying the precipitation process [2].

---

* Corresponding author.
*E-mail address:* pl404@cam.ac.uk (P. Lang).

http://dx.doi.org/10.1016/j.jallcom.2014.04.119

Nucleation and growth of precipitates is an exothermic reaction that releases energy (heat) from the system to the surroundings, whereas the dissolution of precipitates is endothermic and requires energy from the surrounding. In the experimental DSC setup of this study, shown in Fig. 1, the difference in the amount of heat required to maintain the same temperature of the sample and the reference material, during continuous heating of the system, is scanned.

With the development of suitable thermo-kinetic models, physically-based modelling of precipitation kinetics has made significant progress. Hersent et al. [2] simulated a differential scanning calorimetry curve of a 2024 Al-Cu-Mg alloy using a Kampmann–Wagner type model [3]. Khan and Starink [4] reported simulated DSC curves for precipitation and dissolution in 2xxx Al alloys. Povoden-Karadeniz et al. [5] presented a DSC-curve of 6016 Al–Mg–Si alloy based on the thermodynamic modelling of metastable precipitates. Falahati et al. [1] combined thermo-kinetic simulation and experimental analysis to investigate the precipitation behaviour in 6xxx AlMgSi alloys. They utilized a mean-field approach for complex systems (SFFK model [6,7]) to capture the essential physics of the phase transformation process. This latter approach is utilized also in the present work.

The precipitation sequence in hardenable 7xxx Al-alloys is generally accepted as [8–10]

$$\text{SSS} \rightarrow \text{metastable GP zones} \rightarrow \text{metastable } \eta' \rightarrow \text{stable } \eta,$$

with SSS representing the supersaturated solid solution condition after solution treatment and quenching. In this state, the sample contains randomly distributed substitutional Zn and Mg atoms in a face-centred cubic (fcc) $\alpha$-Al matrix and, typically, a high amount of non-equilibrium quenched-in lattice vacancies.

GP-zones are generally accepted as precipitates formed during room temperature ageing and the early stages of artificial ageing [11]. In combination with the evolution of quenched-in excess vacancies, these precipitates strongly influence the subsequent precipitation of the metastable hardening phase $\eta'$, which is commonly considered as the main hardening phase in 7xxx Al-alloys. The over-aged situation is represented by the nucleation and growth of the stable phase $\eta$.

To evaluate the sequence of precipitates and to assign the individual peaks of a DSC curve to the formation and dissolution of precipitates, in the present work, experimental DSC curves are compared to precipitation kinetics model predictions. One laboratory Al–Zn–Mg alloy is compared to an industrial alloy 7075. The effect of quenched-in vacancies is taken into account in our simulation approach.

## 2. Experimental

Two 7xxx Al alloys (pure Al–Zn–Mg and AA 7075), with chemical compositions listed in Table 1 are used for the experimental investigations. The pure Al–Zn–Mg alloy used in this work was prepared from high-purity materials in a high-vacuum pilot casting machine. The alloy ingots were homogenized at 480–495 °C for 12 h to modify the as-cast structure, and then hot and cold rolled to 1.25 mm thick sheets. The solution heat treatment was given at 475 °C for 30 min in a laboratory recirculation air furnace, followed by water quenching. The mean linear metal quenching rate was measured to be about 500 °C/s, using a thermocouple embedded into a dummy specimen.

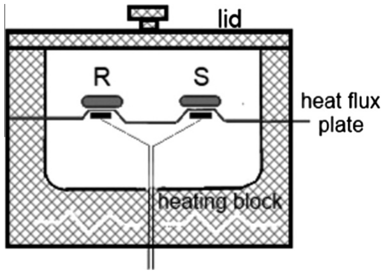

**Fig. 1.** Schematic illustration of a DSC heat flux cell.

**Table 1**
Main chemical composition (wt.%) of investigated alloys.

| Alloy | Zn | Mg | Cu | Fe | Cr |
|---|---|---|---|---|---|
| Pure Al–Zn–Mg | 4.0 | 2.0 | – | – | – |
| AA 7075 | 5.8 | 2.5 | 1.5 | 0.1 | 0.2 |

The DSC experiments on disks, having a diameter of 6 mm and a thickness of 1 mm thickness, are carried out in a TA Instruments 2920 modulated DSC, using a continuous heating rate of 5 °C/min under pure nitrogen flow at a rate of 50 ml/min. The samples are mounted in the DSC chamber immediately after quenching (within one minute natural ageing at RT). Differential scanning calorimetry scans are made over the temperature range from 25 °C to 480 °C. Annealed Al of technical purity (99.98%) and of comparable shape and weight to the sample is used as a reference. The reference does not undergo any phase change during the heat treatment.

For TEM investigation, the specimen were prepared as disks with a diameter of 3 mm and a thickness of 0.3 mm and further electro-polished until being transparent for a 200 kV electron probe. The TEM investigations were carried out on a Tecnai F20 FEGTEM. The grain sizes of the solution heat treated samples are investigated using light optical microscopy.

### 2.1. Thermo-kinetic calculation

Computational thermo-kinetic simulation using multi-component classical nucleation theory and mean-field evolution equations for the size and composition of precipitates has become a standard technique in order to understand nucleation, growth and dissolution of precipitates in a super-saturated solid solution. The precipitation simulation approach presented here is based on a combination of compiled and assessed Gibbs energy functions of matrix and precipitate phases and solute element diffusivities (CALPHAD-type databases) [5] with parameter-free physical models, allowing for predictive precipitation kinetics simulation. The Onsager thermodynamic extremal principle [12,13] has been employed in the modelling according to the approach described in Svoboda et al. [6]. The numerical implementation in the solid-state transformation simulation software package MatCalc has been described in detail by Kozeschnik et al. [7,14].

The precipitate-matrix interfacial energy, which is a key input parameter in solid-state nucleation theory, is evaluated from the generalized broken-bond model [15]. Size correction for the interface energy of small precipitates is accounted for in the simulations [16].

The FSAK model [17] is utilized to describe the evolution of the excess quenched-in vacancies and their interaction with precipitate formation. This is particularly important at the early stages of precipitation after quenching and during heating up in the DSC. The thermo-kinetic simulation approach itself has been described in application to numerous precipitation problems and the interested reader is referred to Refs. [18–20] for more details. The theoretical concepts behind the thermo-kinetic simulations have been compiled recently [21].

### 2.2. Modelling of heat flow curves

For the precipitation simulations, the system of matrix and precipitates is set up in terms of basic information (elements, phases, Gibbs energies and mobility data) as well as microstructural input parameters. Whereas the basic information is read routinely from thermodynamic and kinetic databases [22,23], the microstructural input parameters (homogeneous or heterogeneous nucleation sites of precipitates, aspect ratio of non-spherical precipitates, dislocation density of the matrix, volumetric misfit between precipitate and matrix, etc.) are defined specifically for each alloy system based on experimental information. In the course of the simulation, MatCalc monitors nucleation, growth, coarsening and dissolution of all precipitates and keeps record of the chemical composition of the matrix on basis of the amount of precipitated phases and global mass conservation. From this information, the thermo-chemical properties of the system, such as the enthalpy and heat capacity, are evaluated and, finally, the DSC curves are calculated.

The heat treatment schedule defined in the simulation is identical to the experimental procedure. Solution treatment is conducted at 475 °C, followed by water-quenching to 25 °C (RT) with a mean quenching rate of 500 °C/s. At RT, within 1 min, the sample is inserted into the DSC chamber, followed by continuous heating from 25 to 480 °C at a rate of 5 °C/min.

For analysis of the simulation results, we utilize the relation between the heat flow signal in the DSC and the specific heat capacity as

$$\frac{\Delta Q}{\Delta t} = \frac{C_p \cdot \Delta T}{\Delta t} \tag{1}$$

where $\Delta Q/\Delta t$ is the heat flow [J/(s * g)], $C_p$ is the heat capacity [J/(K * g)] and $\Delta T/\Delta t$ is the heating rate [K/s].

In the computer simulations, we mimic the situation inside the calorimeter by introducing an additional virtual matrix phase into the system, which has the same composition as the reference sample (in the presented case, pure Al). From the Gibbs energies of the pure Al reference phase, the solid solution α-Al matrix phase and the precipitates of the system, the system enthalpy $H$ is calculated based on the well-known relation between enthalpy ($H$), Gibbs energy ($G$) and entropy ($S$) as

$$H = G + TS \tag{2}$$

The heat flow Q per gram of the sample relative to the pure Al reference is given as

$$Q = \frac{d(H_S - H_{ref.})}{dT}\frac{\Delta T}{\Delta t} = \frac{d(\Delta H)}{dT}\frac{\Delta T}{\Delta t} \tag{3}$$

$H_s$ is the specific enthalpy per gram of the alloy system and $H_{ref.}$ is the specific enthalpy per gram of the reference phase of pure Al. $\Delta T/\Delta t$ represents the heating rate.

Eqs. (2) and (3) are determined by changes of the system as a function of time and temperature. The presented mathematical relations are utilized further in the following analysis of heat flow during DSC probing.

### 2.3. Setup and calibration of the kinetic model

The precipitation process occurring in the course of heating in the DSC is simulated by nucleation and growth of individual precipitates. The precipitates considered in the simulations for the pure Al–Zn–Mg system are the coherent GP zones ($Al_8MgZn_{1.2}$), the platelet η′ phase ($Zn_{1.65}Mg_{0.75}Al_{0.6}$) and the stable η-phase (Laves phase $MgZn_2$) [22]. In the case of the industrial alloy, the S-phase ($Al_2CuMg$) and the T-phase (AlCuMgZn) are taken into account, too [22]. The additions of Fe and Cr in the industrial alloy are not considered in thermo-dynamic aspects in the simulation, but the grain size in the modelling is adjusted to experimentally measured sizes, since such microalloying elements, by formation of intermetallic phases, pin the grain boundaries during homogenization and solution heat treatment to avoid grain growth.

The models implemented in MatCalc contain a number of input parameters, which are obtained from experimental observation, such as dislocation density, grain size and the Young's modulus of the matrix. The degree of interface coherency, the shape of the different particles, the volumetric misfit and nucleation site preferences used in the simulations are listed in Table 2 and represent the key input data for the simulation.

One important input parameter for the nucleation process is the choice of the nucleation sites. When considering homogeneous nucleation (nucleation site: bulk), each single atom in the structure represents a potential nucleation site. For heterogeneous nucleation, dislocations or grain boundaries are used as potential nucleation sites. The number density of potential nucleation sites at dislocations is assumed to be the sum of all atomic sites along the dislocation core. The potential number of nucleation sites at grain boundaries is evaluated on the basis of a geometrical model (tetrakaidecahedron), representing polycrystalline grain morphology, again as the number of atoms located at the grain boundaries.

Another important input parameter concerns the morphology of the particles. A single aspect ratio is set for each kind of precipitate, describing their platelet, spherical or needle shape and thus defining the solute diffusion field geometry during growth. Thus, the evolution of mean thickness and width is obtained on a realistic basis and accounts for the modified growth kinetics of non-spherical precipitates. This is shown on the example of the metastable phase η′ in Fig. 9.

The physical properties of the matrix used in the simulations are summarized in Table 3. With our computational approach, the DSC curves of the studied alloys are described with the identical set of calibrated input parameters, except the grain size. The grain size was roughly estimated by light optical microscopy (Fig. 2) in the solutionized and quenched specimen (T4 condition).

**Table 2**
Summary of input data for precipitation kinetics simulation.

| Phase | GP zones | η′ | η | S-phase | T-phase |
|---|---|---|---|---|---|
| Interface[a] | C | SC | IC | IC | IC |
| Volume misfit (%)[b] | 6 | 15 | 0 | 0 | 0 |
| Nucleation sites[c] | B | D | G | G | G |
| Shape factor[d] | 0.1 | 0.1 | 1 | 1 | 1 |

[a] C – coherent, SC – semi-coherent, IC – incoherent.
[b] Volumetric misfit only relevant for coherent/semicoherent phases (values as chosen in simulation).
[c] B – bulk, D – dislocations, G – grain boundaries.
[d] Aspect ratio: 0.1 – plate, 1 – sphere.

**Table 3**
Summary of input data for precipitation domain (Al-matrix).

| Parameter | Value/unit |
|---|---|
| Young's modulus | $80.2 \times 10^9 - (4.01 \times 10^7\ T)$ Pa |
| Poisson's ratio | 0.33 |
| Dislocation density | $10^{11}\ m^{-2}$ |
| Grain diameter | 150 μm (pure Al–Zn–Mg)<br>20 μm (AA 7075) |

## 3. Results

Differential scanning calorimetry (DSC) curves serve as an indicator for precipitation and dissolution reactions in metallurgical alloys. The evolution of microstructure for the observed heat effects in the DSC scans was studied through TEM analysis.

In a first step, we investigate the influence of alloy composition on the DSC signal of the pure Al–Zn–Mg alloy by thermo-kinetic simulation. We emphasize that the DSC signal depends mainly on the evolution of the matrix chemical composition, which, in turn, is determined by the evolution of particle size and number density of precipitates. The DSC curves for the pure Al–Zn–Mg system and for the industrial material AA7075 are reproduced next by modelling. The experimental DSC result is compared to the simulation. The modelling provides the important information on the origin of the peaks and responsible precipitate types. Finally, the predictions about precipitate radii and densities are compared to TEM results. Keeping in mind that the simulation approach is of predictive character, this last step is the vital procedure in interpretation of results and identification of precipitation phases.

### 3.1. Pure Al–Zn–Mg alloy

The experimentally observed DSC curve in Fig. 3 exhibits four distinctive exothermic peaks. These are related to the formation and dissolution of the various precipitates in the pure Al–Zn–Mg alloy. Figs. 4 and 5 summarize the main results of the corresponding MatCalc simulations in the form of the precipitate phase fraction evolution as well as the evolution of the matrix chemical composition.

For a given heating rate, the change in heat flow and, thus, the DSC signal is mainly controlled by the change of matrix composition due to precipitation. This is plausible, because the total volume fraction of all precipitates reaches maximally around 1 volume percent at any time during the DSC run (see Fig. 4), which is insufficient in terms of volume fraction to contribute remarkably to the enthalpy of the system. The heating rate is influencing the kinetics of precipitation reactions and, consequently, the heat flow. For thermally activated processes, it is well known, that exo- and endothermic reaction peaks shift to higher temperatures as the heating rate increases. Fig. 6 shows the effect of three different heating rates, 5 °C/min, 10 °C/min and 20 °C/min, on the simulated heat flow of the pure Al–Zn–Mg alloy. With increasing heating rate, the exothermic DSC peaks, due to precipitation of η′ and η, occur at slightly higher temperatures.

In Fig. 3, neither a pronounced exothermic peak, related to the formation of GP zones, is observable in the experimental DSC curve, nor is a considerable reduction of the alloying elements in the matrix calculated for the temperature up to 100 °C (Fig. 5), which is a priori surprising. The experimental DSC curve shows small formation and dissolution stages from 70 °C to 120 °C that reveal very early solute aggregation taking place. Although the presence of small GP zones in the as-quenched sample cannot be excluded, we associate the reactions with solute clusters, not being defined in our thermodynamic models yet. These clusters might be

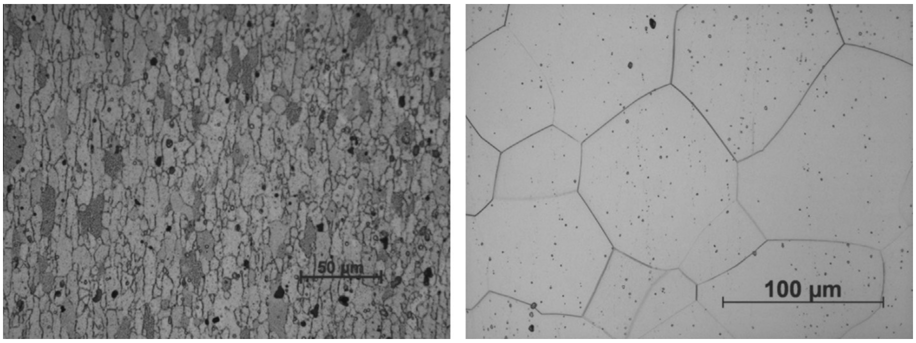

**Fig. 2.** Microstructure of AA7075 (left) and pure Al–Zn–Mg (right) in T4 condition.

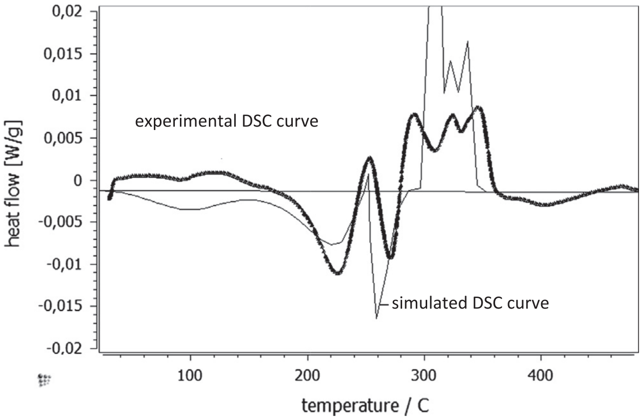

**Fig. 3.** DSC model prediction of the heat flow compared with experimental scan for the pure Al–Zn–Mg alloy. Heating rate is 5 °C/min.

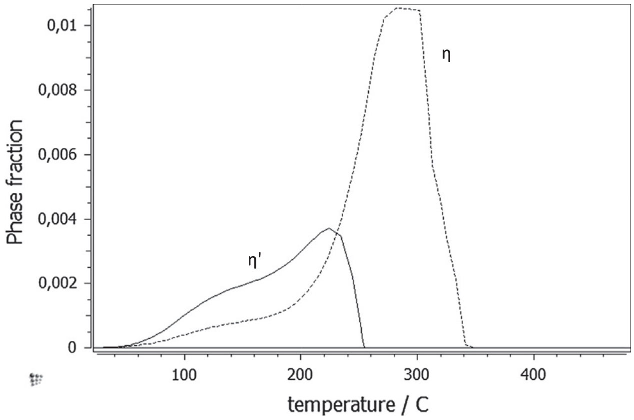

**Fig. 4.** Simulated molar phase fraction evolution for the pure Al–Zn–Mg alloy over temperature during the DSC run (5 °C/min).

vacancy-rich and form during or shortly after quenching the specimen from higher temperatures. A definite TEM identification of the origin of this precipitation stage was not possible in this temperature range (90 °C). According to the investigations, it concluded that the growth of GP zones at this chemical composition does not take place at room temperature in a time scale of just one minute. The choice of the Zn/Mg ratio in the pure Al–Zn–Mg sample might explain this finding. For further inspection of this issue, a calculation with the same input parameters for the precipitates and the matrix is conducted for a system containing 6 wt.% Zn and 2 wt.% Mg. The results are given in Fig. 7.

According to our simulations, a GP-zone phase fraction of about 5 vol.% is predicted in the alloy with 6 wt.% Zn, leading to a strong exothermic peak in the DSC curve at a temperature around 100 °C. In contrast, the GP-zone volume fraction in the alloy with 4 wt.% Zn is negligibly small, which is in accordance with the experiment. The fact that our simulations predict a strong GP-zone signal in the 6 wt.% Zn alloy and almost no GP-zone formation in the 4 wt.% Zn alloy adds confidence to the calculation results.

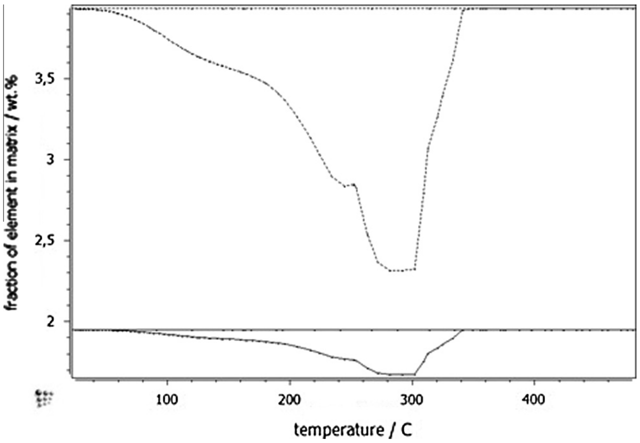

**Fig. 5.** Simulated weight fraction of elements in the matrix for the pure Al–Zn–Mg alloy over temperature. The horizontal line corresponds to the unaltered composition during quenching.

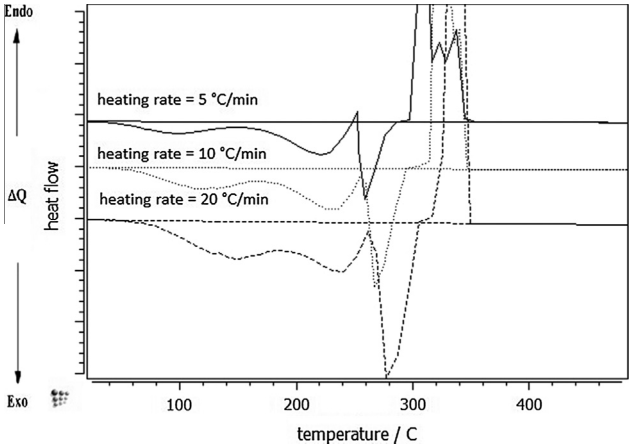

**Fig. 6.** Simulated DSC thermograms of Al–4 wt.% Zn–2 wt.% Mg at different heating rates.

On basis of the simulated evolution of phase fractions shown in Fig. 3, a correlation of DSC peaks with precipitation and dissolution of second phases is attempted. Except for the temperature range

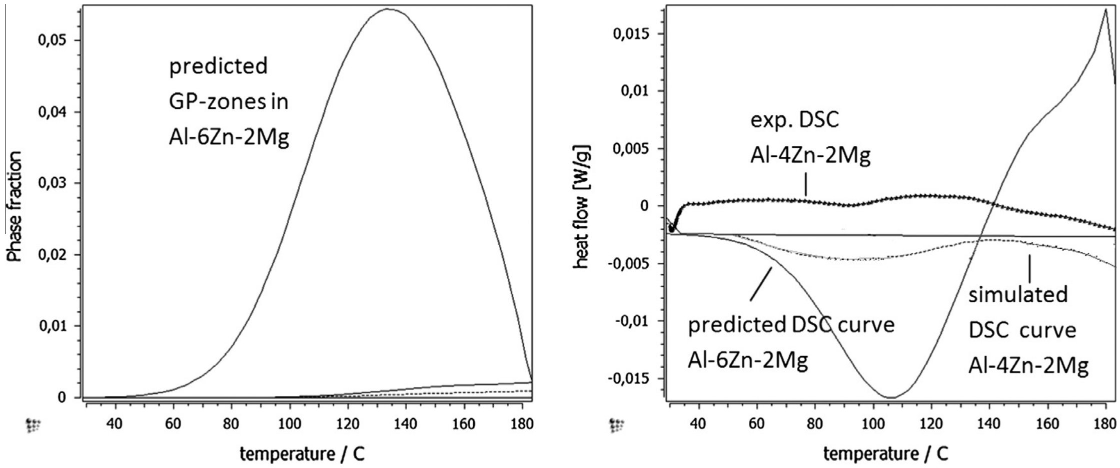

**Fig. 7.** Simulated predicted phase fraction of GP zones (left) and DSC curve comparison for Al–6Zn–2Mg and Al–4Zn–2Mg for a heating rate of 5 °C/min.

40–160 °C, where solute clusters are assumed to form, the experimental trend is well reproduced. Since we do not consider solute clusters in our modelling, the simulated precipitation reactions for the $\eta'$ phase starts at too low temperatures than experimentally observed. The first large ($-10$ mW/g) exothermic peak at $\sim$220 °C is associated with the main formation of the $\eta'$ phase. The following exothermic peak at $\sim$280 °C is associated with the formation of the stable $\eta$-phase. The smaller exothermic peaks at $\sim$320 °C and $\sim$340 °C are assumed to coincide with coarsening or changing the morphology of the stable $\eta$-phase. To investigate the precipitate reactions, represented by the main exothermic peaks at 220 °C, 280 °C and 320 °C, TEM analysis is conducted. After the specimens have been heated at a rate of 5 °C/min and kept at the peak specific peak temperatures (220 °C, 280 °C and 320 °C) for 3 min, the specimens are subjected to TEM examination. The assumptions put on the DSC exothermic reactions are confirmed by the TEM/HRTEM observations. The precipitate microstructure for the examinations at 220 °C are shown in Fig. 8, showing fine dispersed $\eta'$ precipitates, mainly. High Resolution Transmission Electron Microscope (HRTEM) and the corresponding Fast Fourier Transform (FFT) diffraction images are shown in Fig. 8. The image simulations were performed and analysed using Java Electron Microscopy Simulation (JEMS) software [24].

With the changes of the matrix composition and the source of the DSC signal investigated, the nature of the $\eta'$ phase and evolution of the corresponding precipitation parameters are examined, next, and discussed. From literature and from the HRTEM images, the experimentally observed shape of this precipitate is well confined [25,9]. Accordingly, in our simulations, we use an aspect ratio model for non-spherical morphologies [26], which is able to predict the evolution of radius and length of the precipitates in a more accurate way than a simple model based on spherical morphology. For the $\eta'$ phase, which is the most important phase for precipitation strengthening in this kind of alloys, our TEM results indicate that these precipitates adopt disc-like form. With an aspect ratio of 0.1 in our simulation, the models give realistic predictions of mean diameter and mean length, see Fig. 9. The simulated sizes are in good agreement with the measured values from TEM, having approximately 5–20 nm in length and 2–4 nm in diameter. The calculated number density of the $\eta$' is approximately $4 \times 10^{21}$ m$^{-3}$, which is in the same order of magnitude as the ones measured by TEM image analysis (0.6–$4 \times 10^{21}$ m$^{-3}$). Due to the small sample volumes in TEM, uncertainties in determination of the foil thickness and a heterogeneous distribution of precipitates in the specimens, we can only provide estimates for the number density in the form of a density range.

In a next step, the exothermic peak at 280 °C, associated with the formation of the stable $\eta$ phase, is investigated by TEM analysis. The corresponding images are given in Fig. 10.

The calculated mean diameter of the nearly spherical $\eta$ particles during the DSC run is shown in Fig. 11. The mean diameter for a temperature of 280 °C is calculated about 32 nm, which is in good agreement with the dimensions of typical precipitate representatives at this temperature stage, as observed in the TEM investigation (Fig. 10).

As clearly observable in Fig. 10, the number density of $\eta$ precipitates is lower than that of $\eta'$. We calculate a value of about $9 \times 10^{19}$ m$^{-3}$. The outputs of the modelling, e.g. the particle sizes,

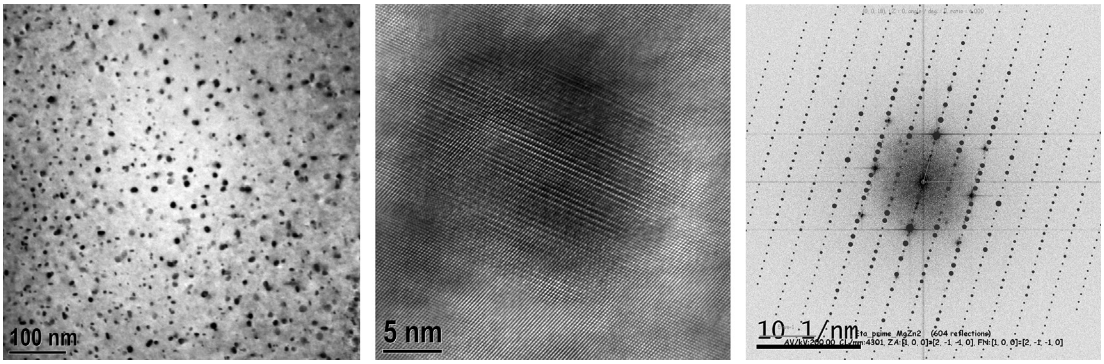

**Fig. 8.** Bright-field imaging (TEM) of the precipitate microstructure (left), HRTEM image of $\eta'$ phase (middle) at 220 °C in pure Al–Zn–Mg along [001] matrix orientation. Simulated diffraction patterns (FFT) by JEMS programme [24] (right) of $\eta'$ phase and the aluminium matrix.

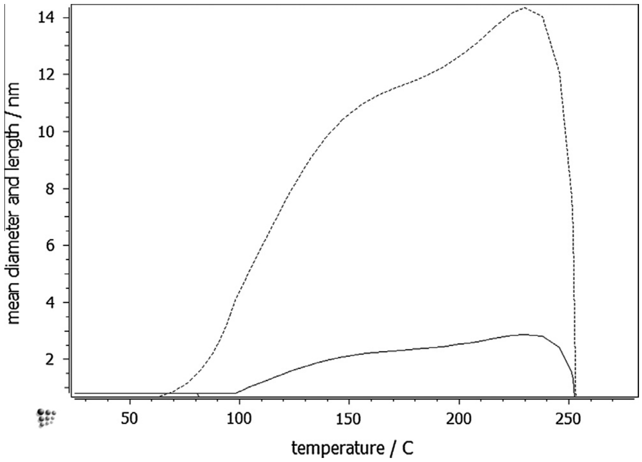

**Fig. 9.** Calculated mean diameter (max. 14.2 nm) and mean width (max. 2.8 nm) of η′ in the pure Al–Zn–Mg alloy during continuous heating with 5 °C/min.

the volume fractions, the particle densities and the concentration in the matrix are in good agreement with the experimentally found values.

The TEM investigation at 320 °C shows coarsening of the η phase, as shown in Fig. 12. This coarsening stage is also reproducible with the modelling approach we use. In Fig. 11 the calculated mean diameter of the η phase is plotted. At a temperature of 320 °C, we calculate a mean diameter of 43 nm.

### 3.2. Industrial AA 7075

The simulation result for the industrial alloy is shown in Fig. 13 together with the experimentally observed DSC curve.

The experimental DSC signal in Fig. 13 exhibits four exothermic peaks. Sequentially, the peaks are assumed to be associated with GP zone formation, formation of η′ phase, the precipitation of the stable phase η and, finally, the formation of the T and/or S – phases in the temperature range from 240 °C to 280 °C. In our calculations, we consider the same phases as used for the pure Al–Zn–Mg system with the same input parameters, as given in Table 2.

The corresponding phase fractions of the industrial alloy 7075 are given in Fig. 14, showing the unambiguous formation of GP-zones, followed by η′ and subsequently the stable phases during continuous DSC scan.

Although the overall simulation corresponds well with the experimental results, we observe some deviation for the initial precipitation stages. The calculated peak is slightly shifted to lower temperature and it is also a bit lower in its height. However, this observation may be explained by the absence of Cu-containing early phases in the present thermo-kinetic treatment. Due to the absence of Cu in the early phases, in our simulation, Cu remains uniformly distributed in the matrix, initially.

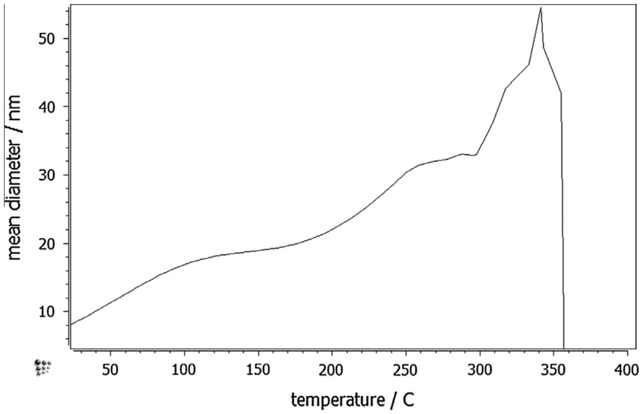

**Fig. 11.** Calculated mean diameter of η in the pure Al–Zn–Mg alloy during continuous heating with 5 °C/min.

The later stage of precipitation in the temperature range between 240 °C and 280 °C is a challenge at the present state of thermo-kinetic modelling. Since we have focused mainly on the understanding of the thermodynamics and kinetics of the metastable and stable phases of the Al–Zn–Mg system, more and detailed future work is necessary to improve the thermo-kinetic simulations for complex 7xxx Al alloys. Especially, for the understanding of the formation of Cu-containing phases, more experimental investigations are required to optimize modelling of important phases in the 7xxx Al series.

## 4. Summary

In this study, we present a thermo-kinetic model for simulation of the heat flow evolution of Al–Zn–Mg alloys. It is shown that the present simulation framework is capable of describing the decomposition of the supersaturated matrix, involving the formation and identification of the most relevant metastable and stable precipitates. In addition, the simulations deliver information about number densities and mean diameter of each specific phase, which are commonly only available through extensive experimental work. In the combination of theoretical models, based on physical principles and experimental observations, we are able to correlate and interpret the heat flux curve to the enthalpy changes accompanying complex precipitation reactions in Al–Zn–Mg series aluminium

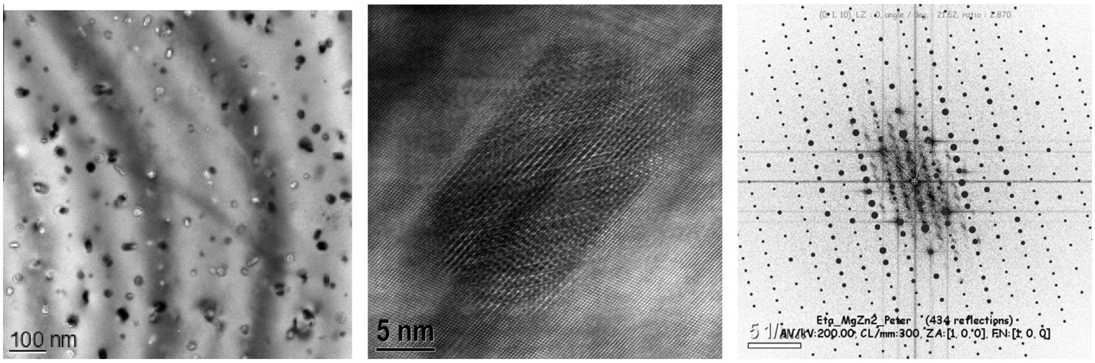

**Fig. 10.** Bright-field imaging (TEM) of the precipitate microstructure (left), HRTEM image (middle) in pure Al–Zn–Mg along [1 1 1] matrix orientation. FFT (JEMS) image of η-phase at 280 °C (right).

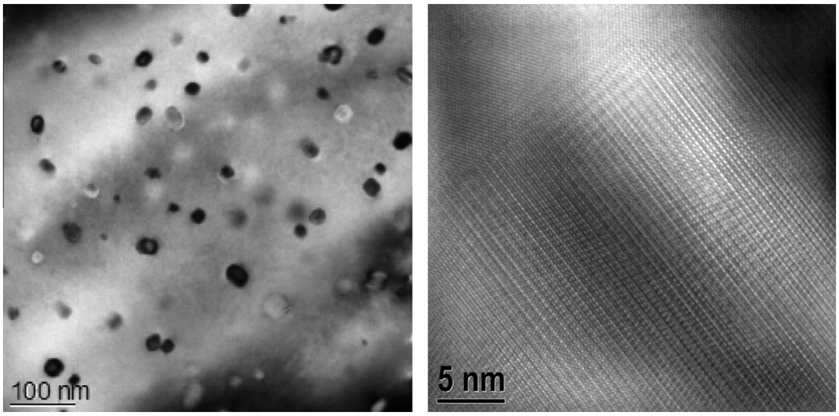

**Fig. 12.** Bright-field imaging (TEM) of the precipitate microstructure (left) and HRTEM image of η phase (right) at 320 °C in pure Al–Zn–Mg along [1 1 1] matrix orientation.

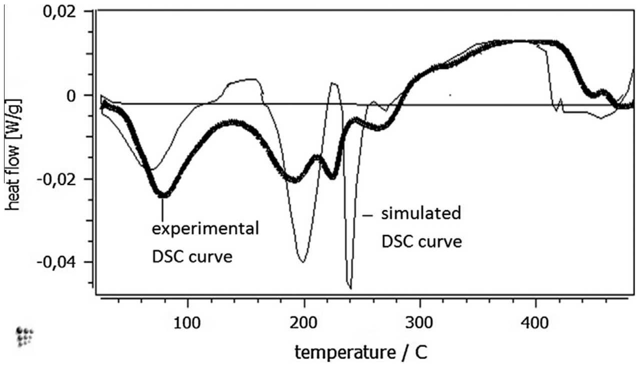

**Fig. 13.** DSC model prediction of the heat flow compared with experimental scan for the industrial AA 7075 alloy.

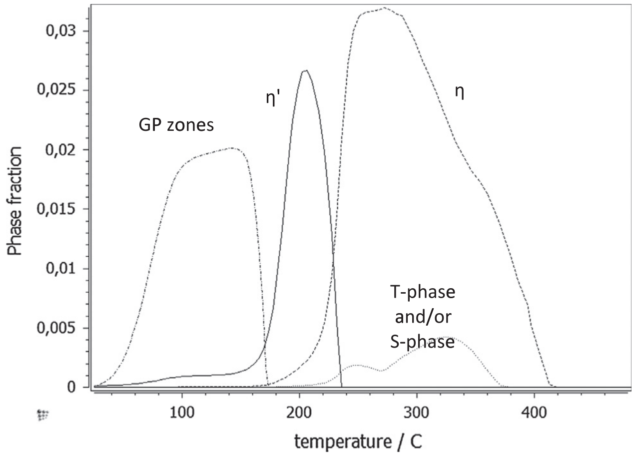

**Fig. 14.** Simulated molar phase fraction evolution for the Al alloy 7075 over temperature during the DSC run (5 °C/min).

alloys during non-isothermal DSC analysis in a self-consistent manner.

## Acknowledgements

Financial support by the Austrian Federal Government (in particular from the Bundesministerium für Verkehr, Innovation und Technologie and the Bundesministerium für Wirtschaft, Familie und Jugend) and the Styrian Provincial Government, represented by Österreichische Forschungsförderungsgesellschaft mbH and by Steirische Wirtschaftsförderungsgesellschaft mbH, within the research activities of the K2 Competence Centre on "Integrated Research in Materials, Processing and Product Engineering", operated by the Materials Center Leoben Forschung GmbH in the framework of the Austrian COMET Competence Centre Programme, is gratefully acknowledged. TEM investigations are carried out using facilities at the University Service Centre for Transmission Electron Microscopy, Vienna University of Technology, Austria.

The authors acknowledge the supply of samples by AMAG/Austria.

## References

[1] A. Falahati, E. Povoden-Karadeniz, P. Lang, P. Warczok, E. Kozeschnik, Evolution of metastable phases in the Al–Mg–Si system – part II: heat flux evolution during DSC probing, Int. J. Mater. Res. (2010/2009) 1089–1096.

[2] E. Hersent, J.H. Driver, D. Piot, Modelling differential scanning calorimetry curves of precipitation in Al–Cu–Mg, Scripta Mater 62 (2010) 455–457.

[3] R. Kampmann, R. Wagner, Decomposition of alloys: the early stages, Acta Scripta Metall. Series (1984) 91–103.

[4] I.N. Khan, M.J. Starink, Microstructure and strength modelling of Al–Cu–Mg alloys druing non-isothermal treatments: part 1 – controlled heating and cooling, Mater. Sci. Technol. 24 (2008) 1403–1410.

[5] E. Povoden-Karadeniz, P. Lang, P. Warczok, A. Falahati, W. Jun, E. Kozeschnik, CALPHAD modeling of metastable phases in the Al–Mg–Si system, CALPHAD 43 (2013) 94–104.

[6] J. Svoboda, F.D. Fischer, P. Fratzl, E. Kozeschnik, Modelling of kinetics in multi-component multi-phase systems with spherical precipitates: I: theory, Mater. Sci. Eng. A 385 (1–2) (2004) 166–174.

[7] E. Kozeschnik, J. Svoboda, P. Fratzl, F.D. Fischer, Modelling of kinetics in multi-component multi-phase systems with spherical precipitates: II: numerical solution and application, Mater. Sci. Eng. A 385 (1–2) (2004) 157–165.

[8] D.S. Thompson, B.S. Subramanya, S.A. Levy, Quench rate effects in Al–Zn–Mg–Cu alloys, Metall. Trans. 2 (1971) 1149–1160.

[9] G. Sha, A. Cerezo, Early-stage precipitation in Al–Zn–Mg–Cu alloy (7050), Acta Mater. 52 (2004) 4503–4516.

[10] A. Deschamps, F. Livet, Y. Brechet, Influence of predeformation on ageing in an Al–Zn–Mg alloy—I. Microstructure evolution and mechanical properties, Acta Mater. 47 (1998) 281–292.

[11] J. Chen, L. Zhen, S. Yang, W. Shao, S. Dai, Investigation of precipitation behaviour and related hardening in AA 7055 aluminium alloy, Mater. Sci. Eng. A 500 (2009) 34–42.

[12] L. Onsager, Reciprocal relations in irreversible processes. I, Phys. Rev. 37 (4) (1931) 405–426.

[13] L. Onsager, Reciprocal relations in irreversible processes. I, Phys. Rev. 38 (12) (1931) 2265–2279.

[14] E. Kozeschnik, J. Svoboda, F.D. Fischer, Modified evolution equations for the precipitation kinetics of complex phases in multi-component systems, CALPHAD 28 (2005) 379–382.

[15] B. Sonderegger, E. Kozeschnik, Generalized Nearest-Neighbor Broken-Bond analysis of randomly oriented coherent interfaces in multicomponent fcc and bcc structures, Met. Mater. Trans. 40A (2009) 499–510.

[16] B. Sonderegger, E. Kozeschnik, Size dependence of the interfacial energy in the generalized nearest-neighbor broken-bond approach, Scripta Mater. 60 (2009) 635–638.

[17] F.D. Fischer, J. Svoboda, F. Appel, E. Kozeschnik, Modeling of excess vacancy annihilation at different types of sinks, Acta Mater 59 (2011) 3463–3472.

[18] A. Falahati, P. Lang, E. Kozeschnik, Precipitation in Al-alloy 6016–the role of excess vacancies, Mater. Sci. Forum 706–709 (2012) 317–322.

[19] E. Povoden, E. Kozeschnik, Simulation of precipitation kinetics and precipitation strengthening of B2-precipitates in martensitic PH 13–8 Mo steel, ISIJ Int. 52 (2012) 610–615.

[20] S. Zamberger, E. Kozeschnik, Carbo-nitride precipitation in tempered martensite-computer simulation and experiment mater, Sci. Forum 706–709 (2012) 1586–1591.

[21] E. Kozeschnik, Modeling solid-state precipitation, Momentum Press, LLC, 2013. ISBN 978-1-60650-062-0.

[22] Thermodynamic database for Al-systems, (mc_al.tdb, version 2.002), Institute of Materials Science and Technology, Vienna University of Technology, Austria.

[23] Mobility database for Al-systems, (mc_al.ddb, version 2.002), Institute of Materials Science and Technology, Vienna University of Technology, Austria.

[24] P. Stadelmann, http://cimewww.dpfl.ch/people/Stadelmann/jemsWebSite/jems.html.

[25] A. Kverneland, V. Hansen, R. Vincent, K. Gjonnes, J. Gjonnes, Structure analysis of embedded nano-sized particles by precession electron diffraction. $\eta'$-precipitate in an Al–Zn–Mg alloy as example, Ultramicroscopy 106 (2006) 492–502.

[26] E. Kozeschnik, J. Svoboda, F.D. Fischer, Shape factors in modeling of precipitation, Mater. Sci. Eng. A 441 (2006) 68–72.

*Advanced Materials Research Vol. 922 (2014) pp 406-411*
*Online available since 2014/May/07 at www.scientific.net*
*© (2014) Trans Tech Publications, Switzerland*
*doi:10.4028/www.scientific.net/AMR.922.406*

# Thermo-kinetic simulation of the yield strength evolution of AA7075 during natural aging

Peter Lang[a], Thomas Weisz[b], Mohammad Reza Ahmadi[b,c],
Erwin Povoden-Karadeniz[b,c], Ahmad Falahati[b] and Ernst Kozeschnik[b,c]

[a] Materials Center Leoben Forschungsgesellschaft mbH, Leoben, Austria.
[b] Christian Doppler Laboratory "Early Stages of Precipitation", Institute of Materials Science and Technology, Vienna University of Technology, Vienna, Austria.
[c] Institute of Materials Science and Technology, Vienna University of Technology, Vienna, Austria.

**Keyword:** simulation, natural aging, AA7075, excess quenched in vacancies, binding energy

## Abstract

The yield strength evolution in aluminum alloy 7075 is investigated during natural aging. The thermo-kinetic simulation, capable of predicting nucleation, growth, coarsening and dissolution of metastable and stable hardening precipitates in Al-Zn-Mg-Cu during natural aging, is outlined briefly. A recent strengthening model for shearing and bypassing of precipitates by dislocations is utilized to calculate the evolution of the macroscopic yield strength at room temperature. The simulation accounts for vacancy-solute binding energies calculated with the help of first principles simulations that influence the diffusivity of the system due to the presence of excess quenched-in vacancies. These results provide predictions about the amount of excess vacancies trapped by solid solution alloying elements and how the lifetime of vacancies changes due to attractive or repelling binding forces between vacancies and different solid atoms in the aluminum matrix. In our approach, we calculate the strength evolution after quenching due to interaction between dislocations and changes in the microstructure by precipitation of different kinds of secondary phases. The predicted evolution of yield strength is finally verified on experimental measurements.

## Introduction

The commercial Al-Zn-Mg(-Cu) (7075) alloys are widely used for high-strength structural applications in aerospace industry as well as for sporting goods. The 7xxx series of aluminum alloys are age-hardenable. The industrial processing route of these alloys includes a solution treatment followed by a quench, a tensile deformation and finally a multistep ageing treatment. During solution heat-treatment, the specimen is kept at high temperature for sufficiently long time to ensure the complete dissolution of secondary precipitates. Primary precipitates may stay inside the matrix. When the solutionized sample is rapidly cooled to below the solvus line, two phases are commonly thermodynamically stable: alpha and beta. For quenching rates, which are sufficiently high, metastable precipitates form in the supersaturated solid solution at low temperature.

The precipitation sequence of an AA7xxx (Al-Zn-Mg-Cu) with a Zn to Mg ratio greater than two [1] is generally accepted as: high density of coherent spherically shaped GP zones [2] followed by semicoherent intermediate metastable η'. The stable phase is η ($MgZn_2$). During aging, the strength increases as the number and sizes of precipitates increases. This effect is known as precipitation hardening, which is controlled by the chemical composition of the system, the phases that form, the kinetics of the precipitation reactions, time and temperature. In 7xxx series alloys, aging occurs even at room temperature. This is called natural aging and it commonly starts within several hours after quenching.

In order to increase aging kinetics, artificial aging is normally done at higher temperature. During natural aging, the peak strength often reaches a plateau after given time. In artificial aging, the strength reaches a maximum and, after long time or high aging temperatures, the strength decreases again and the alloy becomes overaged [3]. Due to the utilization of these alloys in aerospace application, also the interest in natural aging in Al-Zn-Mg(-Cu) alloys has raised in recent time. In this work, we propose a quantitative analysis to determine the aging kinetics based on the age hardening response of AA7075. We present models to predict the yield strength evolution during room temperature storage. The work consists of modeling the precipitation kinetics as well as the strengthening components to study the effect of natural aging in 7xxx Al alloys.

## Numerical Simulation

The vacancy evolution process in the bulk material during quench and subsequent aging is described in section 2.1. The mathematic relations for description of the effective strengthening mechanisms are given in section 2.2.

### Vacancy evolution

The present heat treatment, including a quench from elevated temperature to room temperature, produces a high amount of excess vacancies. These excess non-equilibrium vacancies are called quenched-in vacancies. They substantially enhance the diffusivity even at low temperature, however, with ongoing time, the excess vacancies are annihilated at sources and sinks, such as jogs at dislocation or grain boundaries. We consider the annihilation at homogeneously distributed jogs at existing dislocations with a constant density $H_{disl}$ of $1\cdot10^{11}$ m/m$^{-3}$ and the annihilation at grain boundaries with a mean diameter $d_{grain}$ of 50 µm. Fischer et al. [4] developed models to calculate the total rate of vacancy site fraction corresponding to these mechanism, which are fully taken into account in our simulation. Successful implementation of this formalism has been published earlier [5] and will not be discussed here in detail.

The excess vacancies move to the sinks to be annihilated by diffusion. The diffusion path can be manipulated by vacancy traps, such as solute atoms or precipitate / matrix interfaces. Strong binding between vacancies and solute atoms are an important factor influencing vacancy diffusion inside the matrix. Strong attractive vacancy - solute binding energy can significantly reduce the mobility of vacancies and, thus, the annihilation rate of excess vacancies. The extended lifetime of excess vacancies ensures higher diffusivity for longer aging times at low temperatures, which is a key factor in understanding the natural aging behavior of Al-Zn-Mg(-Cu) alloys. Fischer et al. [6], recently, presented a theory, which describes the decrease of the total energy of a system by attractive binding enthalpies $\Delta E_k$ and a modified diffusion coefficient $D_{Tk}$ including the effects of existing traps for interstitials. In our work, their relations are utilized for the interaction of different solutes to vacancies, too. The knowledge of the effective binding enthalpy $\Delta E_k$ between a trap of sort *k* and a vacancy enables one to calculate the site fraction of trapped vacancies. This approach is reproduced briefly, next.

Let us assume a system of $N_l$ moles of vacant positions in the crystal lattice and *m* different kinds of trapping elements. The site fraction of the vacancies are $y_l$ and the site fraction of the vacancies in a trap of sort k are $y_{Tk,n}$. The possible trapping positions are indicated with the symbol *n*. In our case, each sort of trap involves *n*=12 possible trap positions due to the coordination number of the fcc structure. The following relation holds

$$\frac{y_l(1-y_{Tk})}{y_{Tk,n}(1-y_l)} = \exp\left(\frac{-\Delta E_k}{R_g T}\right) = K_{k,n}, \qquad k=1,...m;n=12. \tag{1}$$

where $R_g$ is the gas constant and $T$ is temperature.

When knowing $\Delta E_k$, the trapping enthalpy of a vacancy to a solute atom, equation (1) can be resolved with respect to the site fraction of trapped vacancies $y_{Tk}$ with

$$y_{Tk,n} = \frac{y_l}{K_{k,n} + y_l(1-K_{k,n})}, \qquad \text{k=1,...,m;n=12.} \tag{2}$$

We assume that the trapping atoms are also mobile but with different diffusivity compared to those without attractive forces. In consideration of the mass balance and the corresponding volume, the concentration of the trapped vacancies $c_{Tk}$ and of the free vacancies $c_l$ in the lattice can be calculated. The distinctive concentrations allow the formulation of the diffusive flux of the system with effective traps [6] as

$$j = -D_l grad(c_l) - \sum_{k=1}^{m} D_{Tk} grad(c_{Tk}) \tag{3}$$

The quantity $D_l$ is the diffusion coefficient in the system without traps and $D_{tk}$ is the diffusion coefficient of the vacancy in the trap of sort k. For deep traps, $D_{tk}$ becomes zero. Entropic effects, dependent only on temperature, and the element specific binding enthalpy (equation 2) define the concentration of trapped vacancies $c_{Tk}$ and, therefore, the evolution of diffusivity of the system.

The annihilation and generation of quenched-in vacancies at different kinds of sources and sinks are fully taken into account [4] in the diffusion coefficient. Furthermore, the kinetic effects of trapping of vacancies at different alloying elements are included in the model.

Table 1: Calculated binding enthalpies using first principle calculations (present work).

| Solute-vacancy | First-principle value, present work [eV] |
|---|---|
| Zn – Va | 0.032 |
| Mg – Va | 0.026 |
| Cu - Va | 0.124 |

## Simulation of precipitation strengthening

The remarkable strength increase in Al-Zn-Mg(-Cu) alloys during natural aging can be attributed to a high number density of GP-zones with 5-20 nm diameter [7]. It is generally assumed that, for the coherent, shearable GP-zones, which precipitate after or even during the quench, the operative strengthening mechanisms is the coherency strain effect. This effect is investigated in the following together with the Orowan mechanism. The latter is operative for impenetrable precipitates with incoherent precipitate/matrix interfaces during aging.

## Coherency misfit strengthening

This mechanism is the most important strengthening mechanism in 7xxx Al alloys. According to Ardell [8], the increase of yield strength due to this mechanism can be written as

$$\Delta\sigma_{coh} = \alpha MG(\varepsilon)^{3/2}\left(\frac{8\pi r^4 n_v}{3b}\right)^{1/2} \tag{4}$$

where α is a constant (=3) [8] and ε is the fractional misfit between the precipitate and the matrix. *M* (=3.06) is the Taylor factor, $n_v$ is the number density of precipitates, *b* is the Burgers vector (=0.286 nm), *G* is the shear modulus (=28 GPa) and *r* is the mean radius of the precipitates.

## Strengthening effect of non-shearable particles

Precipitation strengthening in Al-Zn-Mg(-Cu) alloys is due to coherent and incoherent phases. The conventional equation for Orowan strengthening for incoherent phases can be written as [8]

$$\Delta\sigma_{Orowan} = \frac{0.4GbM}{\pi\lambda\sqrt{1-\upsilon}}\ln\left(\frac{2r}{b}\right), \tag{5}$$

where υ (=0.33) is Poisson's ratio and λ is the mean particle spacing in the slip plane of the dislocation.

To calculate the overall precipitation strengthening effect ($\sigma_p$), the different mechanisms for cutting and looping (Orowan mechanism) are superimposed as

$$\sigma_p = (\sigma_{coh}^{\alpha} + \sigma_{Orowan}^{\alpha})^{\frac{1}{\alpha}} \tag{6}$$

with *α* chosen as 1.4.

## Solid solution strengthening

In age hardening aluminium alloys, elements including Mg, Zn and Cu give rise to considerable solid solution strengthening. This effect is described by the following equation

$$\sigma_{ss} = \sum_i k_i c_i^{2/3} \tag{7}$$

$c_i$ is the concentration (mole fraction) of a specific alloying element in solid solution and $k_i$ is the corresponding scaling factor, which is 29 MPa/wt.%$^{2/3}$ [9] for Mg, 3 MPa/wt.%$^{2/3}$ for Zn and 46 MPa/wt.%$^{2/3}$ for Cu [9].

## Calculation of the yield strength evolution

The total yield strength $R_{p0.2}$ is treated as a superposition of the inherent lattice strength ($\sigma_0=20MPa$), solid solution strengthening ($\sigma_{ss}$) and precipitation strengthening ($\sigma_p$) as

$$R_{p0.2} = \sigma_0 + \sigma_{ss} + \sigma_p \tag{8}$$

## Material and Experimental Methods

The composition of the AA7075 used in the investigations is shown in Table 1. The experimental data are supplied by AMAG rolling GmbH. The tensile test specimens were solution annealed at 480°C for 30 min, quenched into water and then stored at room temperature (~ 25°C) for 300 hrs.

Table 1: Chemical composition of AA 7075

| Element | Zn | Mg | Cu | Zr | Al |
|---|---|---|---|---|---|
| wt.% | 5.81 | 2.56 | 1.48 | 0.03 | rest |

## Results and Discussion

All simulations carried out in this work are performed with the software package MatCalc version 5.52.1002. The aging of rapidly quenched Al-Zn-Mg(-Cu) alloys from solution temperature (=480°C) to room temperature is accompanied by the generation of GP-zones having an approximately spherical shape. With increasing aging time, the GP-zones increase in size and, simultaneously, the strength of the alloy increases. GP-zones nucleate homogenously. With extended aging time, the next transition precipitates, known as η', the precursor of the equilibrium η ($MgZn_2$) phase, precipitate. This semicoherent phase is the main hardening phase in the Al-Zn-Mg(-Cu) alloys but reaches highest strengthening potential only at elevated temperatures. The semicoherent η' nucleate and grow on dislocations and subgrain boundaries.

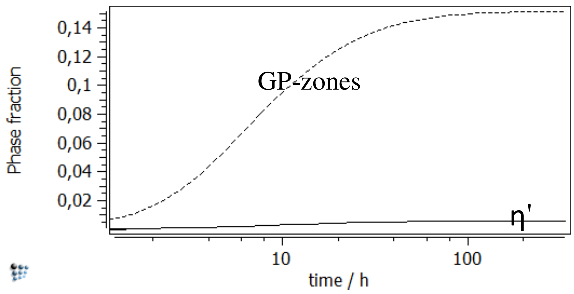

Figure 1: Calculated phase fraction for a 5.8Zn-2.5Mg -1.5 Mg Al alloy during natural aging at room temperature (~25°C)

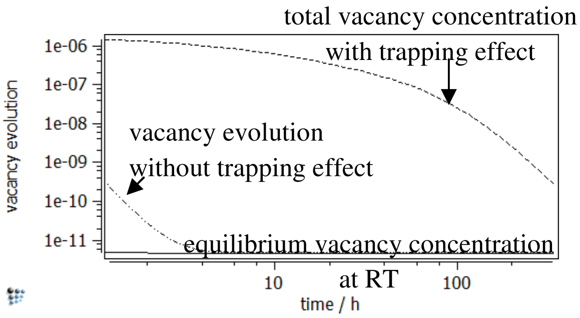

Figure 2: Vacancy evolution during natural aging showing the high amount of excess vacancies after rapid quench

Fig. 1 shows the evolution of the phase fraction of the metastable phases of the system Al-Zn-Mg(-Cu). During natural ageing, the hardness is mainly determined by the amount of very small precipitates, GP-zones and, later, the η' precipitates, formed after quenching. High quenching rates are necessary to allow precipitates to nucleate homogeneously. Decreasing the quenching rate decreases the number of quenched-in vacancies and, therefore, diffusion is decelerated at low temperatures. Under the latter conditions, the precipitate distribution coarsens and the ultimate strength is particularly low. Solid solution strengthening also contribute to the increase of strength of the naturally aged aluminium alloys, but to a much less extent as precipitation strengthening.

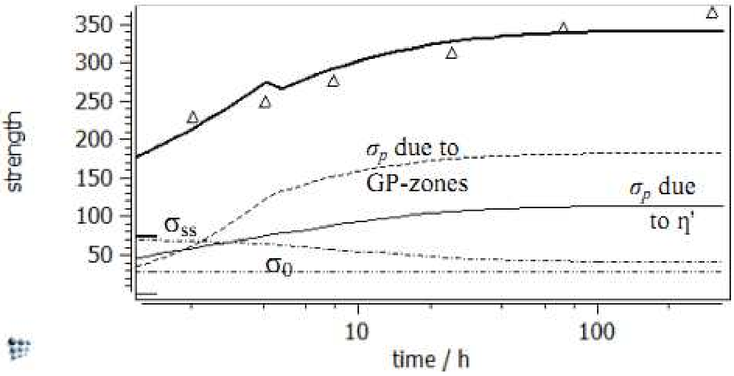

Figure 3: Evolution of $R_{p0.2}$ for 5.8Zn-2.5Mg-1.5Mg Al alloy during natural aging

Fig.3 shows the calculated $R_{p0.2}$ together with the individual strengthening contributions. According to experiment, the strength reaches nearly a plateau after 300hrs during natural aging. At this time, an $R_{p0.2}$ of about 340 MPa is calculated, which corresponds well with the experimental data. This increase of strength after long time natural aging can only be explained by the continuous presence of excess quenched-in vacancies (Fig.2) due to vacancy trapping. The high vacancy keeps the diffusivity of alloying elements in the system at a high level.

## Acknowledgement

Financial support by the Austrian Federal Government (in particular from Bundesministerium für Verkehr, Innovation und Technologie and Bundesministerium für Wirtschaft, Familie und Jugend) represented by Österreichische Forschungsförderungsgesellschaft mbH and the Styrian and the Tyrolean Provincial Government, represented by Steirische Wirtschaftsförderungsgesellschaft mbH and Standortagentur Tirol, within the framework of the COMET Funding Programme is gratefully acknowledged.

## References

[1] Peng X., Fan J., Yang Y., Chen Y., Yin Y. *International Journal of Solids and Structures* (2003), 40, 7385-7397.
[2] Deschamps A., Niewcz as M., Bley F., Brechet Y., Embury J.D., LeSinq L., Livet F., Simon J.P. *Philosphical Magazine A.* (1999), 79, 10, 2485-2504.
[3] Nowill C.,. *PhD thesis*. 2007.
[4] Fischer F.D., Svoboda J, Appel F. , Kozeschnik E., *Acta Mater.* (2011), 59, 3463-3472.
[5] Lang P., Povoden-Karadeniz E., Mayer W., Falahati A., Kozeschnik E., *proceedings PRICM8* (2013) 3181-3188
[6] Fischer F.D., Svoboda J., Appel F., Kozeschnik E. *Modelling Simul. Mater. Sci. Eng.* (2013) in print.
[7] Fuller C.B., Mahonex M.W., Calabrese M., Micona L., *Materials Science and Engineering* (2010), A 527, 2233-2240
[8] Ardell A.J., *Metall. Trans.* (1984), 16A, 2131-2165
[9] Myhr OR., Grong Ø., Andersen SJ., *Acta Mater.* (2001), 49, 65-75

**THERMEC 2013 Supplement**

10.4028/www.scientific.net/AMR.922

**Thermo-Kinetic Simulation of the Yield Strength Evolution of AA7075 during Natural Aging**

10.4028/www.scientific.net/AMR.922.406

# Simulation of the plastic deformation response of AA 6082 in W condition

Peter Lang[1,2], Markus Rath[1], Pavel Sherstnev[3], Ernst Kozeschnik[1,4]

[1]Institute of Materials Science and Technology, Vienna University of Technology,
Favoritenstraße 9-11, Vienna, 1040, Austria
[2]Department of Materials Science and Metallurgy, University of Cambridge,
Charles Babbage Road 27, Cambridge, CB3 0FS, UK
[3]LKR Leichtmetallkompetenzzentrum Ranshofen GmbH, AIT Austrian Institute of Technology, P.O. Box 26, 5282 Ranshofen, Austria
[4]Christian Doppler Laboratory "Early Stages of Precipitation", Institute of Materials Science and Technology, Vienna University of Technology, Favoritenstraße 9-11, 1040, Austria

Corresponding author:

P. Lang
University of Cambridge
Charles Babbage Road 27
CB3 0FS, UK

Email: pl404@cam.ac.uk

Keywords: deformation, aluminium alloy 6082, simulation, stress-strain, W condition

Abstract

In the present study, the parameterization of a simple model is assessed for describing the deformation behaviour of an AA6082 aluminium alloy in W condition (solution treated and quenched). To obtain a better physical understanding of the flow stress and the dislocation density evolution as well as the strain rate sensitivity of this kind of Al alloy, modelling and simulation of the work-hardening behaviour is applied in the framework of a simple but efficient one-parameter model based on the total dislocation density evolution. Experimental stress-strain curves, measured for several temperatures and strain rates, are taken from literature to compare and validate our computational approach. The study finally delivers a parameterization for the evolution equations that is capable of describing the deformation characteristics of the alloy in terms of the temperature and strain-rate sensitive yield stress. In addition to the effect of the dislocation-dislocation interactions, the intrinsic yield stress of aluminium and solid solution strengthening is taken into account.

## Introduction

The influence of ageing on the mechanical properties of Al-Mg-Si alloys and their work-hardening behaviour is important from both, scientific and industrial viewpoints. Especially, the AA6082 is a popular representative of the Al-Mg-Si series and the mechanical response of this alloy during plastic deformation is essential in optimizing the production process (e.g. rolling and forming). In order to predict the deformation behaviour for an Al-Mg-Si system, a one-parameter dislocation evolution-based model [1] is utilized, which correlates stress and strain in the form of rate equations that account for the impact of strain rate and temperature in a Kocks-Mecking based formulation [2].

Al-Mg-Si alloys are well known for being heat treatable to form metastable and stable precipitates. Since precipitation hardening, as well as the nature of the precipitates and the related solute distribution, alters the work-hardening behaviour of the alloy, in a first step towards a complete description of mechanical response of hardenable alloys, the present study is focused only on conditions where precipitation reactions can be neglected.

Several approaches and applications have been proposed to model work hardening of Al alloys [3-11]. Some of these approaches can be characterized as constitutive, such as the Sellars and McTegart [7], Hollomon [8] or Ludwigson [4] equations, while others rely on a one- [2] or multi-parameter [10-12] microstructural description based on appropriate state parameters. In the present work, we use an extended one-parameter model in the sense of the Kocks, Mecking [2,13] (KM model) and Estrin, Mecking [14] (modified KM model) theory, which has been developed and formulated in ref. [1]. The KM strain hardening theory is based on the evolution of the dislocation density, $\rho$, during plastic deformation and their contribution to strength, σ. The model is briefly reviewed and, finally, a parameter set is proposed by which the temperature and strain rate dependence of the present alloy in the W condition is reproduced well. Experimental data sets for AA6082 in W condition, taken from literature, are compared to our modelling results.

## One-parameter model for the stress-strain response

A popular and efficient Ansatz to describe and characterise the evolution of a metallic microstructure during work hardening is the one-parameter microstructural approach. The term "one-parameter" emphasizes that the stress-strain response is controlled by the evolution of a single state parameter, only. In the present model, this parameter is the total dislocation density, evolving as a consequence of the interplay of generation and annihilation terms during deformation in the material. The KM strain hardening one-parameter theory [2] consists of a hardening part, accounting for the strain-induced increase in dislocation density, and a softening contribution due to annihilation or rearrangement of dislocations (dynamic recovery).

The general relation between the Yield stress increase due to dislocation hardening, $\sigma_d$, and the total dislocation density, $\rho$, is given as [1,15]

$$\Delta\sigma_d = \alpha M G b\sqrt{\rho} \ , \qquad (1)$$

with $M$ being the Taylor factor, $G$ the shear modulus and $b$ the Burger's vector. In the present analysis, $\alpha$ is a proportionality factor with the value of 0.5. This relation between stress and dislocation density holds for the cases where the flow stress is solely controlled by dislocation-dislocation interaction. Although this applies in a strict sense to pure fcc materials [15], only, it can also be used for dilute solid solutions, where the particle and lattice resistance to dislocation motion is negligibly small.

The evolution of the total dislocation density, $\rho$, during deformation is dependent on the dislocation storage and dislocation annihilation rates as [1]

$$\frac{d\rho}{dt} = \left.\frac{d\rho}{dt}\right|_{\mathrm{a}} - \left.\frac{d\rho}{dt}\right|_{\mathrm{r1}} - \left.\frac{d\rho}{dt}\right|_{\mathrm{r2}} . \tag{2}$$

The initial hardening is due to generation and storage of dislocations. The first term (indexed *a*) in eq. (2) describes the dislocation generation and accumulation process in dependence of temperature and strain rate, with $\rho$ representing the total dislocation density. As deformation proceeds, the softening mechanisms based on annihilation of dislocations finally balance the generation term. The second term (indexed r1) in eq. (2) accounts for spontaneous annihilation dependent on the applied strain rate (dynamic recovery) and the third term (indexed *r2*) is related to static recovery controlled by dislocation climb.

The rate of dislocation accumulation (generation) in the present model is expressed as

$$\left.\frac{d\rho}{dt}\right|_{\mathrm{a}} = \frac{\dot{\phi}}{bL} , \tag{3}$$

where $\dot{\varphi}$ is the plastic strain rate and *L* is the mean free path length for dislocation migration, which is given as

$$L = \frac{A}{\sqrt{\rho}} . \tag{4}$$

*A* is a materials constant and details to its dependence on strain rate and temperature are given in the results section.

The second term in eq. (2) represents the reduction of the dislocation density and the classical softening stage due to spontaneous dislocation annihilation. This mechanism is often denoted as dynamic recovery. As soon as two dislocations with antiparallel Burger's vectors approach each other closer than a critical distance $d_{\mathrm{crit}}$, they will spontaneously annihilate at a rate [17]

$$\left.\frac{d\rho}{dt}\right|_{r1} = -B \cdot 2 \frac{d_{\mathrm{crit}}}{b} \rho \dot{\phi} . \tag{5}$$

The critical distance, $d_{\mathrm{crit}}$, is given as [16]

$$d_{\mathrm{crit}} = \frac{Gb^4}{2\pi(1-\upsilon) \cdot Q^{\mathrm{fv}}} , \tag{6}$$

where $v$ is Poisson's ratio (0.33) and $Q^{\mathrm{fv}}$ is the vacancy formation energy (0.67 eV for Al). *B* is a parameter associated with the dependency of dynamic recovery on the strain rate and experimentally evaluated correlations are given in the results section.

In the formulation of the static recovery term, we assume that the recovery rate [17] is controlled by substitutional self-diffusion along the dislocation cores. The corresponding diffusion coefficient is often denoted as the pipe diffusion coefficient, $D_c$, which, in our simulations, is related to the bulk diffusivity by a temperature dependent factor. Representative mean values for short-circuit diffusion along dislocation cores have been assessed recently by Stechauner and Kozeschnik [18]. These values are adopted in the present work and not treated as adjustable parameters. The thermally-induced recovery rate can then be written as

$$\left.\frac{d\rho}{dt}\right|_{r2} = -C \cdot 2D_{\mathrm{c}} \frac{Gb^3}{k_B T} (\rho^2 - \rho_{\mathrm{equ}}^2)\,. \tag{7}$$

$\rho_{\mathrm{equ}}$ is the equilibrium dislocation density, $k_{\mathrm{B}}$ is the Bolzmann constant. $C$ is a calibration parameter. The values for the term $C$ as used in the present studies, are given in the results section.

Since the model consists of only three independent fitting parameters ($A$, $B$ and $C$), the term "*ABC* model" is used further on for convenience. The dislocation density evolution equations for generation and annihilation are implemented in the software package MatCalc [19,20] and utilized in the simulations of work hardening behaviour of the three different 6082 Al alloys.

To calculate the total yield strength evolution, $\sigma_{\mathrm{total}}$, the intrinsic strength of pure aluminium, $\sigma_0$, the Hall-Petch strengthening, $\sigma_{\mathrm{gb}}$, for fine grain hardening and solid solution hardening, $\sigma_{\mathrm{ss}}$, are added to the strain hardening, $\sigma_{\mathrm{d}}$, by a generalized form of superposition law distinguishing between the athermal, $\sigma_{\mathrm{ath}}$, and thermal, $\sigma_{\mathrm{th}}$, components of the total stress as

$$\sigma_{\mathrm{total}} = \left(\sigma_{\mathrm{th}}^p + \sigma_{\mathrm{ath}}^p\right)^{\frac{1}{p}} \tag{8}$$

with

$$\sigma_{th} = \sigma_0 + \sigma_{\mathrm{ss}} + \sigma_{\mathrm{gb}} + \sigma_{ppt} \qquad \text{and} \qquad \sigma_{\mathrm{ath}} = \sigma_{\mathrm{d}}\,. \tag{8a}$$

The intrinsic yield strength of pure aluminium, $\sigma_0$, is taken as 10 MPa [21]. The coupling exponent, $p$, is taken with a value of 1.8.

The solid solution strengthening contribution is described by the following equation

$$\sigma_{\mathrm{ss}} = \left(\sum_i \left(k_i c_i^{2/3}\right)^q\right)^{\frac{1}{q}}, \tag{9}$$

where $c_i$ is the concentration (weight %) of element $i$ in solid solution and $k_i$ is the corresponding scaling factor. Here, we use 29 MPa/wt.%$^{2/3}$ for Mg and 66 MPa/wt.%$^{2/3}$ for Si [22]. The solid solution strength coupling exponent, $q$, is also taken as 1.8.

The Hall-Petch equation, used to describe the strength increment due to the grain size, is reads as

$$\sigma_{gb} = kM \cdot d^{-1/2}, \tag{10}$$

with the parameter $k$ taken as $0.04 \cdot 10^6$ Pa·m$^{1/2}$ for the given materials and $d$ representing the grain size (grain diameter).

The precipitation strengthening contribution, $\sigma_{ppt}$, is neglected in the present work since we assume that the material is in the W condition, i.e. in the solution heat-treated and quenched condition, and contains only negligible effects from natural ageing.

## Experimental data and simulation setup

The experimental data for the deformation behaviour of three AA6082 alloys in W condition are taken from literature [23,24,25] and compared to our simulation results. The alloys are designated as alloy AA6082-1, AA6082-2 and AA6082-3. They differ slightly in chemical composition, as summarized in Table 1. All experiments used in the present study have been conducted in such a way that the materials were first solution annealed for sufficiently long time to ensure dissolution of the hardening phases, then rapidly quenched and stored such that no noticeable precipitation reactions occurred. To maintain the W condition, storage in liquid nitrogen after solution annealing and quenching was applied in the cases of alloys AA6082-2 and AA6082-3. For alloy AA6082-1, the tests were conducted at the solution annealing temperature and no intermediate storage was necessary. All applied strain rates, except the tests carried out at the solution annealing temperature of 525 °C, are sufficiently high to complete the tests within one minute. The equilibrium dislocation density, $\rho_{equ}$, is assumed to be $10^{11}$ m$^{-2}$, the grain size, $d_{gr}$, for all alloys is taken as 50 µm.

Table 1: Nominal chemical composition (wt.%) of investigated materials

| alloy | Mg | Si | Cu |
|---|---|---|---|
| AA6082-1 | 0.6 | 0.7 | n.a. |
| AA6082-2 | 0.6 | 0.9 | n.a. |
| AA6082-3 | 0.7 | 1.0 | 0.003 |

Table 2: Input parameters used in the strain hardening model

| Parameter | Value |
|---|---|
| $M$ | 3.06 |
| $b$ | $2.84 \cdot 10^{-10}$ m |
| $G$ | $3.14 \cdot 10^{10} - 1.63 \cdot 10^{7} \cdot T$ Pa |
| $\rho_{equ}$ | $10^{11}$ m$^{-2}$ (const.) |
| $d_{gr}$ | $5 \cdot 10^{-5}$ m (const.) |
| $k_{Mg}$ | 29 MPa/wt.%$^{2/3}$ |
| $k_{Si}$ | 66 MPa/wt.%$^{2/3}$ |

## Results

First, the thermal components of the yield strength, $\sigma_{th}$, of the annealed materials are calculated, taking the intrinsic yield strength for pure Al, $\sigma_0$, the Hall-Petch strengthening, $\sigma_{gb}$, and the solid solution strengthening contributions, $\sigma_{ss}$, into account. The thermal yield strength, $\sigma_{th}$, which represents the strength without strain hardening, $\sigma_d$, for the three alloys is depicted on Fig. 1. The effect of Cu on the strengthening behaviour is marginal and, therefore, neglected since only one reference (AA6082-3) reports a Cu content of approximately 0.003 wt.%. We assume that the Cu content is negligible also in the other materials and ignore its contribution to solid solution strengthening.

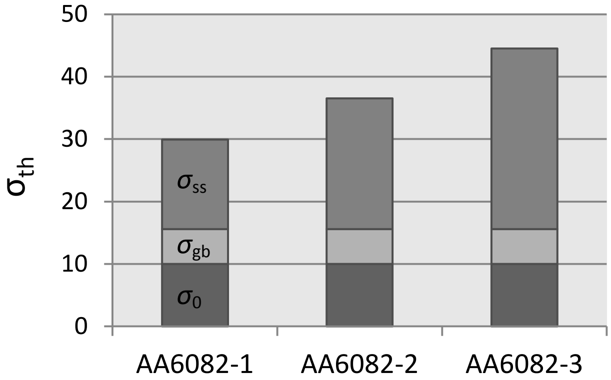

Figure 1: Calculated thermal yield strength contributions, $\sigma_{th}$, for AA6082-1, AA6082-2 and AA6082-3 in the annealed condition (before plastic deformation).

Alloy AA6082-1 has the lowest total amount of alloying elements and exhibits the lowest total yield strength in the annealed condition (29.9 MPa). Alloy AA6082-3, higher alloyed, having 0.3 wt.% Si and 0.1 wt.% Mg more in solid solution, shows an increase of the initial yield strength of approximately 50 %. The initial yield strength of AA6082-3 is evaluated with 44.5 MPa. The one of AA6082-2, in the annealed condition, is calculated to be 36.5 MPa.

In a next step, we discuss the evaluation of the *A*, *B* and *C* coefficients using the experimental information. One of the key parameters in the calculation is the characteristic of the temperature-dependent hardening parameter *A*. In our work, the value of *A* is assessed by fitting to experiments at different testing temperatures but constant strain rate such that the strength matches over the entire temperature range. Figure 2 shows the observed variation of *A* between 300 and 800 K, eq. 11 summarizes the according parameterization. The dislocation generation-related parameter *A* increases linearly with temperature (*T* in K) for the investigated AA 6082 series as

$$A = 0.23 \cdot T - 0.97\,. \tag{11}$$

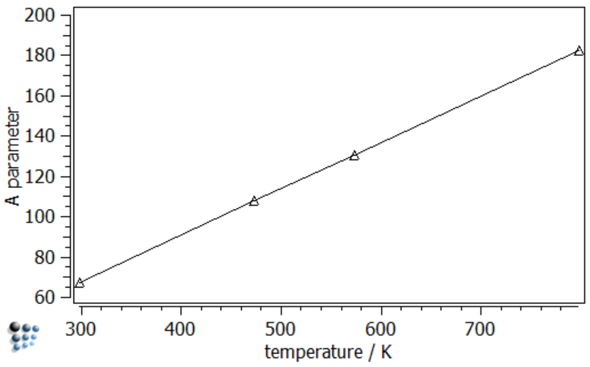

Figure 2: Variation of parameter A as a function of temperature.

The softening parameter *B*, associated with the dynamic recovery effect, is assumed to depend mainly on strain rate. The correlation between *B* and $\dot{\varphi}$ is shown in Figure 2 for data from the present investigation of AA6082 alloys. *B* is assessed by fitting for different strain rates at constant temperature, such that the steady-state part of the stress-strain curve is reproduced for the investigated strain rates. The observed logarithmic strain-rate dependency of *B* for alloy AA6082 in W condition can be written as

$$B = 2 - 0.434 \cdot \ln(\dot{\varphi})\,. \qquad (12)$$

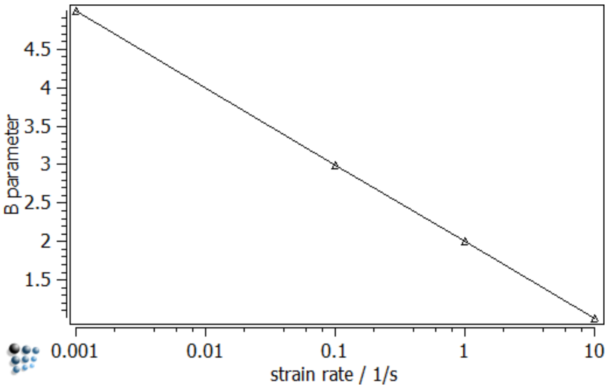

Figure 3: Variation of parameter *B* as a function of strain rate.

The Parameter *C* is assumed to be constant in the present work ($C$=5·$10^{-4}$). Commonly, this parameter can be used to account for effects, such as, solute drag. It is adjusted such that the steady-state conditions in the stress-strain curves are reproduced for the entire testing conditions.

Table 3: Summary of evaluated input parameters *A*, *B* and *C* used in the strain-hardening model

| parameter | value | valid for |
|---|---|---|
| *A* term | 0.23·*T*-0.97 | 298 K ≤ *T* ≤ 800 K |
| *B* term | 2-0.434·lnφ̇ | 0.008 ≤ φ̇ ≤ 10 |
| *C* term | $5 \cdot 10^{-4}$ | 298 K ≤ *T* ≤ 800 K |

To illustrate its applicability, the model is next used to simulate the stress-strain curves for aluminium alloys 6082 in W condition with the nominal compositions given in table 1. Although the industrial alloys have more complex chemical composition, the ternary system Al-Mg-Si is supposed to define the governing chemistry at all instances and we perform our simulations for this case.

### Alloy AA6082-1

The tensile tests in ref. [23] were carried out at different strain rates (0.01 to 10 $s^{-1}$) at the solution annealing temperature of 525 °C. Unfortunately, no exact chemical composition was reported by these authors, which is why we estimate the chemical composition to be in the range of a typical AA6082 with 0.6 wt.% Mg and 0.7 wt.% Si. Figure 4 shows the comparison of the model results with experiments for the three strain rates. Figure 5 shows the calculated evolution of the dislocation density for AA6082-1 as a function of the three strain rates at 525 °C.

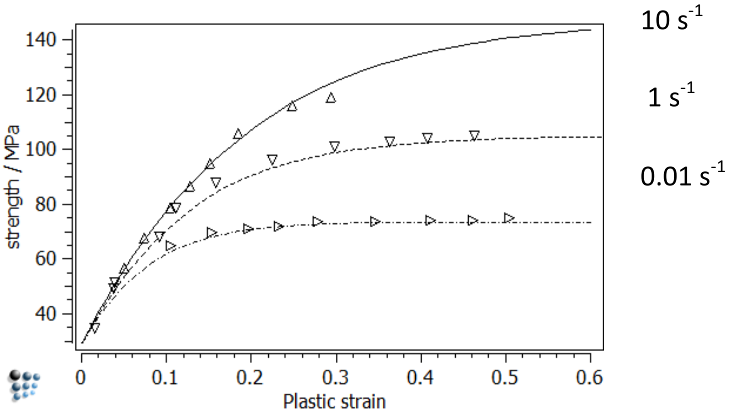

Figure 4: Comparison of experimental (symbols) and computed (lines) stress strain relations for strain rates of 0.01, 1.0 and 10 $s^{-1}$ for alloy AA6082-1 at 525 °C.

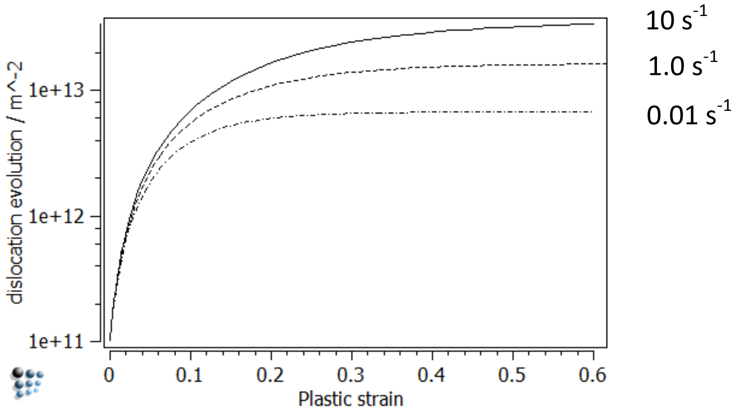

Figure 5: Computed dislocation density evolution for strain rates of 0.01, 1.0 and 10 $s^{-1}$ for alloy AA6082-1 at 525 °C.

**Alloy AA6082-2**

Deformation tests in alloy AA6082-2, ref. [24], carried out in an Al-matrix with 0.59 wt.% Mg and 0.89 wt.% Si, are compared to the model results in Figure 6 for a strain rate of 0.067 $s^{-1}$. The testing temperatures varied from 25 °C to 300 °C. Figure 7 shows the calculated evolution of the dislocation density for AA6082-2 ) for a strain rate of 0.067 $s^{-1}$ as a function of the three test temperatures (25, 200 and 300 °C).

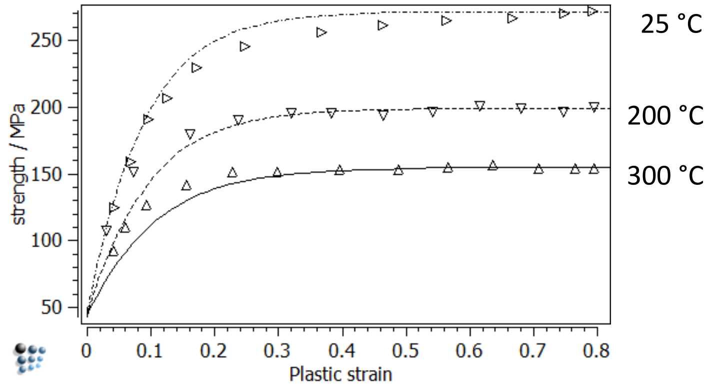

Figure 6: Comparison of experimental (symbols) and computed (lines) stress strain relations for a strain rate of 0.067 $s^{-1}$ at 25 °C, 200 °C and 300 °C for alloy AA6082-2.

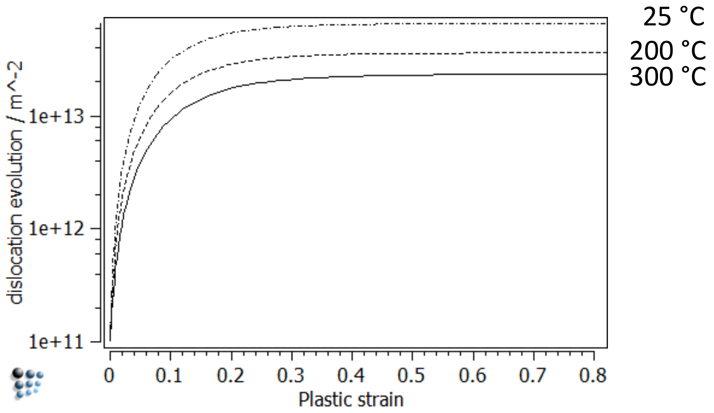

Figure 7: Computed dislocation density evolution for strain rates of 0.067 $s^{-1}$ at 25 °C, 200 °C and 300 °C for alloy AA6082-2.

The model results give a good representation of the experimental observations. At 25 °C, a maximum strength of 250 MPa is reached, whereas the strength at 300 °C reaches a plateau at about 150 MPa. This behaviour is attributed mainly to the temperature-dependent hardening parameter *A* and the thermally activated kinetics of recovery by dislocation climb, parameter *C*.

**Alloy AA6082-3**

The tensile tests in ref. [25] were performed on a 0.67 wt.% Mg, 1.04 wt.% Si industrial alloy AA6082 using a servo-hydraulic testing machine using a strain rate of 0.008 $s^{-1}$ at a temperature of 25 °C. The simulation of the evolution of strength is performed at the same conditions. In figure 8, the calculated results are compared to the experiment. Figure 9 shows the computationally evaluated dislocation density evolution of AA6082-3 for a strain rate of 0.008 $s^{-1}$ at a temperature of 25 °C.

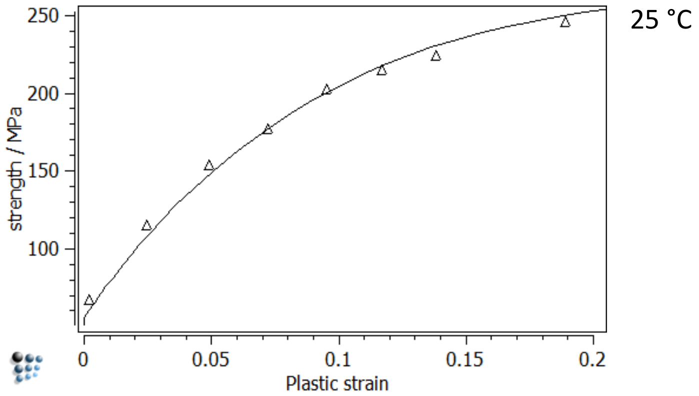

Figure 8: Comparison of experimental (symbols) and computed (curve) stress strain relation for a strain rate of 0.008 $s^{-1}$ for alloy AA6082-3 at 25 °C.

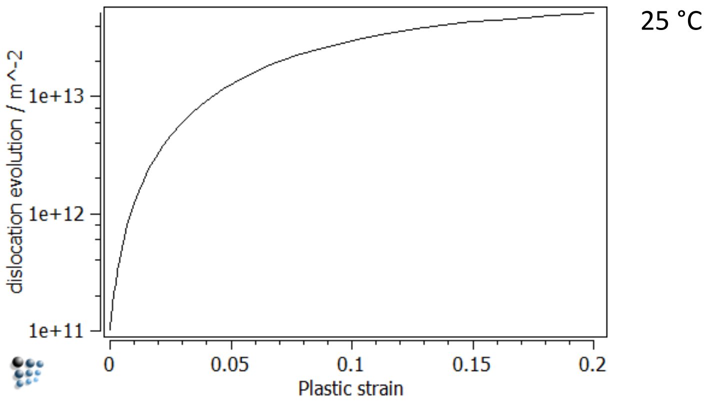

Figure 9: Computed dislocation density evolution for a strain rate of 0.008 $s^{-1}$ for alloy AA6082-3 at 25 °C.

## Conclusion

The effects of temperature and strain rate on the work-hardening behaviour of Al-Mg-Si alloys in solution treated temper (W) are studied with the goal of developing the parameterization of a one-parameter model to reproduce the work-hardening and dynamic recovery behaviour of AA6082 alloys. The *ABC* model, as an extension of the well-established approaches of Kocks, Mecking and Estrin, Mecking, for the prediction of strain hardening is used for this purpose. The stress strain relations are derived from the experiments as a function of the testing conditions (temperature and strain rate). With the dislocation density as the only internal variable, the *ABC* model successfully reproduces the experimentally observed stress strain relations, accounting also for the solid solution strengthening and grain size effect.

## References

[1] P. Sherstnev, P. Lang, E. Kozeschnik, Proc. ECCOMAS 2012 - European Congress on Computational Methods in Applied Sciences and Engineering (2012) 5331.
[2] U.F. Kocks, H. Mecking, Prog. Mater. Sci. 48 (2003) 171.
[3] L.M Cheng, W.J. Poole, J.D. Embury, D.J. Lloyd, Metal. Mater. Trans. A 34 (2003) 2473.
[4] D.C. Ludwigson, Metall. Trans. 2 (1971) 2825.
[5] W.J. Poole, D.J. Lloyd, Proc. 9th Int. Conf. on Al Alloys ICAA9 (2004) 939.
[6] A. Simar, Y. Brechet, B. de Meester, A. Denquin, T. Pardoen, Mater. Sci. Eng. A 486 1-2 (2008) 85.
[7] C.M. Sellars, W.H. McTegart, Acta. Metall 14 (1966) 1136.
[8] J.H. Hollomon, Trans. AIME 162 (1945) 2131.
[9] D.C. Ludwigson, Metall. Trans. 2 (1971) 2825.
[10] E. Nes, K. Marthinsen, Mat. Sci. Eng. A 322 (2002) 176.
[11] E. Nes, K. Marthinsen, Y. Brechet, Scripta Mat. 47 (2002) 607.
[12] F. Roters, D. Raabe, G. Gottstein, Acta Mater. 48 (2000) 4181.
[13] H. Mecking and U.F. Kocks, Acta Metall. 29 (1981) 1865.
[14] Y. Estrin, H. Mecking, Acta Metall 32 1 (1984) 57.
[15] G.I. Taylor, Proc. Roy. Soc. A 145 (1934) 362.
[16] S. Brinkmann, R. Sivanesapillai, A. Hartmaier, Inter. Journal of Fatique 33 (2011) 1369.
[17] L.E. Lindgren, K. Domkin, S. Hansson, Mechanics of Materials 40 (2008) 907.
[18] G. Stechauner, E. Kozeschnik, CALPHAD 47 (2014) 92.
[19] J. Svoboda, F.D. Fischer, P. Fratzl, E. Kozeschnik, Mater. Sci. Eng. A 385 (1-2) (2004) 166.
[20] E. Kozeschnik, J. Svoboda, P. Fratzl, F.D. Fischer, Mater. Sci. Eng. A 385 (1-2) (2004) 157.
[21] S.C. Wang, Z. Zhu, M.J. Starink, Journal of Microscopy 217 (2005) 174-178.
[22] O.R. Myhr, Ø. Grong, S.J. Andersen, Acta. Mater. 49 (2001) 65.
[23] R.P. Garrett, J. Lin, T.A. Dean, International Journal of Plasticity 21 (2005) 1640.
[24] K.I. Aastorp, Norwegian University of Science and Technology (NTNU), thesis (2002)
[25] Ø. Ryen, Norwegian University of Science and Technology (NTNU), thesis (2003)

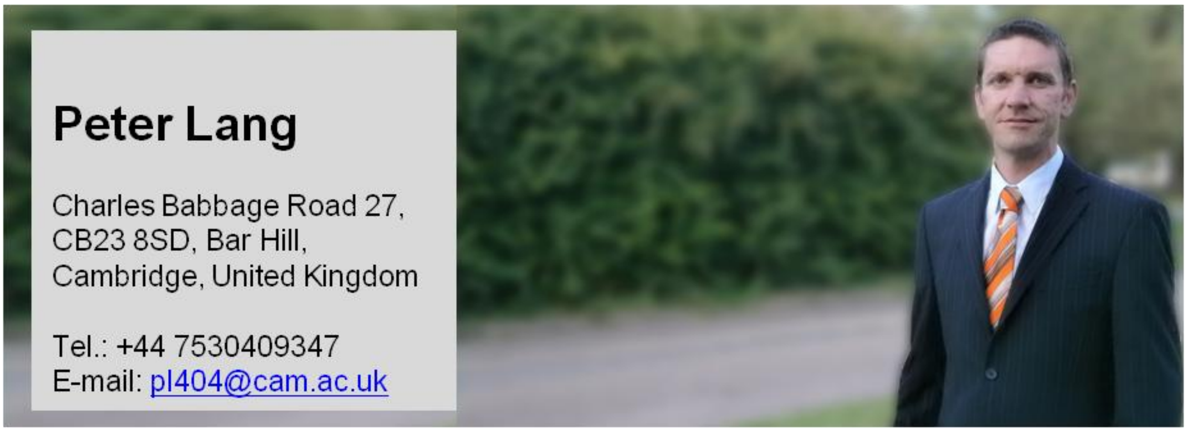

**Peter Lang**

Charles Babbage Road 27,
CB23 8SD, Bar Hill,
Cambridge, United Kingdom

Tel.: +44 7530409347
E-mail: pl404@cam.ac.uk

# Curriculum Vitae

## Professional Experience:

| | |
|---|---|
| 03/2014 - | Research Assistant - Hydrogen Embrittlement Characterisation<br>University of Cambridge, Cambridge, United Kingdom |
| 04/2011 – 01/2014: | Project Assistant - Optimization Development Aluminium<br>Material Center Leoben, Styria, Austria |
| 04/2009 – 03/2011: | Project Assistant - Modelling and Simulation Materials Science<br>Vienna University of Technology, Vienna, Austria |
| 03/2006 – 01/2009: | Project Manager - Solid-Liquid Separation in Mining Operations<br>Andritz AG, Separation, Styria, Graz, Austria |

## Education:

| | |
|---|---|
| 04/2009 – | Doctoral Studies in Mechanical and Industrial Engineering, Institute of Materials Science and -Technology, Vienna University of Technology, Austria |
| 09/2009 – 06/2010: | FH Burgenland, University of Applied Sciences, International Economic Relations; Burgenland, Austria |
| 09/1998 – 11/2005: | Master of Science, Mineral Resources Engineering, Mining Engineering, Montanuniversität Leoben, Styria, Austria<br>Diploma Thesis: „Detail Investigation of the Slurry Ponds located at the "Styrian Iron Mountain" Erzberg", Department of Mineral Resources, cooperation with industry (VA Erzberg GmbH) |
| 09/1988 – 06/1996: | Federal grammar school Mattersburg, Burgenland, Austria |
| 09/1984 – 06/1988: | Primary school Wulkaprodersdorf, Burgenland, Austria |

## Practical work placement

| | |
|---|---|
| 09/2003: | Kärntner Montanindustrie, Waldenstein |
| 07/2003 – 08/2003: | Veitsch – Radex GmbH & Co Breitenau |
| 07/2002 – 08/2002: | Lafarge Perlmooser AG, Werk Mannersdorf |
| 09/2001: | ARGE S6 Tunnel Semmering<br>GKB – Bergbau GmbH, Bereich Umwelt |
| 07/2001 – 08/2001: | Wolfram Bergbau und Hütten – GmbH Nfg. KG |
| 07/2000 - 08/2000: | Karl Lehner + Co Baugesellschaft m.b.H. |
| 02/1999 - 08/1999: | Papst – Lehner Bau |
| 11/1996 - 01/1998: | Military band Burgenland |
| 08/1995: | Gebrüder Haider Bauunternehmung GmbH |
| 07/1993 und 07/1994: | Österreichische Kuvertindustrie Ges.m.b.H |

## Academic lectures / Conferences:

| | |
|---|---|
| 2014: | MMM2014, Berkeley California, USA |
| 2013: | THERMEC, Las Vegas, USA<br>PRICM8, Waikoloa Hawaii, USA |
| 2012: | EATP, Grenoble, France<br>ICAA13, Pittsburgh, USA |
| 2011: | MS&T'11, Columbus, USA |
| 2010: | ICAA12, Yokohama, Japan<br>Junior Science Conference, Vienna, Austria |

## Additional qualification / Awards:

| | |
|---|---|
| 2014: | Gibbs triangle award – annual best paper award CALPHAD journal |
| 2014: | MMM2014 award – 7th Conference, Berkeley California, USA |
| 2004: | Radiation Protection, Seibersdorf Research, Austria |
| 1994: | English course, International Language Academy Oxford |

## Skills:

| | |
|---|---|
| Language: | German (Native)<br>English (Fluent)<br>Russian, Croatian (Basic) |
| IT: | MS-Office, MatCalc, VASP, Linux |

## Interests:

Sport (hiking, climbing, swimming), Music (trombone), Coffee roasting

## References:

on demand